

**Molecular Adsorption and Diffusion Properties of
Polymeric and Microporous Materials via Quartz
Crystal Microbalance Techniques**

A Dissertation

Presented to

The Academic Faculty

by

Anandram Venkatasubramanian

In Partial Fulfillment

of the Requirements for the Degree

Doctor of Philosophy in the

G.W. Woodruff School of Mechanical Engineering

Georgia Institute of Technology

August 2013

Copyright 2013 by Anandram Venkatasubramanian

Molecular Adsorption and Diffusion Properties of Polymeric and Microporous Materials via Quartz Crystal Microbalance Techniques

Approved by

Dr. Peter J. Hesketh, Advisor

G.W. Woodruff School of Mechanical
Engineering
Georgia Institute of Technology

Dr. Todd Sulchek, Committee member

G.W. Woodruff School of Mechanical
Engineering
Georgia Institute of Technology

Dr. Sankar Nair, Co-Advisor

School of Chemical & Biomolecular
Engineering
Georgia Institute of Technology

Dr. David Sholl, Committee member

School of Chemical & Biomolecular
Engineering
Georgia Institute of Technology

**Dr. Samuel Graham, Committee
member**

G.W. Woodruff School of Mechanical
Engineering
Georgia Institute of Technology

Date approved: May 7, 2013

TO MY PARENTS AND UNCLE

ACKNOWLEDGEMENTS

I would like to thank my advisors, Dr. Peter. J Hesketh and Dr. Sankar Nair for guiding me through my doctoral research. Their mentorship was invaluable in developing my knowledge and skills that I was seeking to obtain through my doctoral study at Georgia Institute of Technology. I would also like to thank my dissertation committee members, Dr. David Sholl, Dr. Todd Sulchek and Dr. Samuel Graham for agreeing to critique my thesis and provide valuable insights. I would also like to thank Conoco Phillips/Phillips 66 company for funding my doctoral research generously.

I would like to thank my lab colleagues Milad Navaei, Ilya Ellern, Drew Owen and Ali MahdaviFar with whom I had numerous helpful interactions not only regarding my research work, but also during my coursework at Georgia Tech. I would like to acknowledge the cooperation provided by my colleagues in the School of Chemical and Biomolecular Engineering department at Georgia Tech, namely Dr. Emmanuel Haldoupis, Dr. Dun Yen Kang and Andrew Brown for identifying, synthesizing candidate materials and helping me understand the nuances of material chemistry. It was truly an enriching experience.

I would like to thank the Microelectronic Research Center for letting me use the SEM microscopy and Dr. Sankar Nair's group for letting me use the X-ray diffractometer facility which helped me gain valuable insights in material properties. I would like to thank the faculty members who supervised my coursework and helped me gain a strong background in nanoscale science.

Finally I would like to thank the staff at the Office of Student Services at G.W.Woodruff school of Mechanical Engineering and the facilities and maintenance staff at Georgia Tech for making my doctoral research memorable and comfortable.

Table of Contents

ACKNOWLEDGEMENTS	IV
LIST OF TABLES	XII
LIST OF FIGURES	XIV
NOMENCLATURE	XXII
SUMMARY	XXIII
CHAPTER 1: INTRODUCTION	1
1.1 Nanoporous Materials	1
1.1.1 Metal Organic Frameworks (MOFs)	1
1.1.2 Single Wall Nanotubes (SWNTs)	3
1.2 Polymers	5
1.3 Motivations for this Work	7
1.4 Objectives of this Thesis	8
1.5 Significance of Quartz Crystal Microbalance (QCM) - Based Adsorption and Diffusion Measurements	9
1.6 Topics Covered in this Thesis	9
CHAPTER 2: DESIGN, CONSTRUCTION AND THEORY OF QCM BASED APPARATUS	15
2.1 Design Considerations	15
2.2 Construction of the Experimental Setup	15

2.2.1 Design of the Stainless Steel Pressure Cell _____	15
2.2.2 Thermal Control System _____	17
2.2.3 Analyte Gases _____	18
2.2.4 Pressure Gauge _____	19
2.2.5 Phase Lock Oscillator _____	19
2.2.6 Quartz Crystal Microbalance _____	20
2.3 Description of the QCM based Sorption Apparatus _____	21
2.4 Theory of Measurement _____	25
2.4.1 Theory of Operation of the QCM _____	25
2.4.2 Sauerbrey's Equation _____	29
2.4.3 Factors Affecting the Measurement of Resonant Frequency of QCM _____	30
2.5 Conclusions _____	33
CHAPTER 3: APPLICATIONS TO GAS ADSORPTION IN POLYMERIC MATERIALS _____	34
3.1 Theory of Adsorption in Polymers _____	34
3.2 Materials of Interest _____	36
3.2.1 Matrimid 5218 _____	36
3.2.2 6FDA-DAM _____	37
3.3 Sample Preparation and Characterization of Matrimid 5218 _____	38
3.3.1 Powder Type Deposition _____	38
3.3.2 Thin Film Deposition _____	39
3.4 Gas Adsorption Measurement using Matrimid 5218 _____	40

3.4.1 Powder Deposition _____	40
3.4.2 Thin Film Deposition _____	43
3.5 Sample Preparation of 6FDA-DAM _____	49
3.5.1 Thin Film Deposition _____	49
3.6 Gas Adsorption Measurement using 6FDA-DAM _____	49
3.6.1 Thin Film Deposition _____	49
3.6 Conclusions _____	53
CHAPTER 4: APPLICATIONS TO GAS ADSORPTION IN NANOPOROUS MATERIALS _____	55
4.1 Theory of Adsorption in Nanoporous Materials _____	55
4.1.1 Langmuir Adsorption Model _____	55
4.1.2 Henry's Law _____	57
4.2 Materials of Interest _____	58
4.2.1 Copper-Based MOF (Cu-hfipbb) _____	58
4.2.2 Zeolitic Imidazolate Framework – 90 (ZIF-90) _____	59
4.2.3 Aluminosilicate Nanotubes and its Modifications (AlSiNTs) _____	60
4.3 Sample Preparation and Characterization of Metal Organic Frameworks (MOF) _____	62
4.3.1 Synthesis, Deposition and Characterization of Cu-hfipbb MOF (small crystals) _____	62
4.3.1.1 Synthesis of Cu-hfipbb MOF Crystal (small crystals) _____	62
4.3.1.2 Deposition of Cu-hfipbb MOF Crystals on QCM Substrates (small crystals) _____	63

4.3.1.3 Characterization of Cu-hfipbb MOF Material _____	63
4.3.2 Synthesis, Deposition and Characterization of ZIF-90 MOF _____	65
4.3.2.1 Synthesis of ZIF-90 Crystals _____	65
4.3.2.2 Deposition of ZIF-90 Crystals on QCM Substrates _____	66
4.3.2.3 Characterization of ZIF-90 MOF Material _____	66
4.3.3 Synthesis, Deposition and Characterization of Cu-hfipbb MOF (large crystals) _____	68
4.3.1.1 Synthesis of Cu-hfipbb MOF Crystal (large crystals) _____	68
4.3.1.2 Deposition of Cu-hfipbb MOF Crystals on QCM Substrates (large crystals) _____	68
4.3.1.3 Characterization of Cu-hfipbb MOF Material (large crystals) _____	69
4.4 Gas Adsorption Measurements using Metal Organic Frameworks _____	70
4.4.1 Gas Adsorption Measurements from Cu-hfipbb MOF (small crystals) _____	70
4.4.2 Gas Adsorption Measurements from ZIF- 90 _____	75
4.4.3 Gas Adsorption Measurements from Cu-hfipbb MOF (large crystals) _____	79
4.5 Sample Preparation and Characterization of AluminoSilicate Nanotubes _____	84
4.5.1 Synthesis of Bare Single Wall AluminoSilicate Nanotubes (BNTs) _____	84
4.5.2 Synthesis of Aminomethyltriethoxysilane (AMTES) _____	84
4.5.3 Synthesis of Aminefunctionalized Single Wall AluminoSilicate Nanotubes (ANTs) _____	85
4.5.4 Deposition of BNTs and ANTs on QCM Substrates _____	86
4.5.5 Characterization of the BNTs and ANTs Deposited on the QCM _____	86
4.6 Gas Adsorption Measurements using Nanotubes _____	88

4.6.1 Gas Adsorption Measurements from BNTs and its Modifications	88
4.7 Conclusions	101
CHAPTER 5: APPLICATIONS TO DIFFUSION MEASUREMENTS	103
5.1 Theory of Gas Diffusion in Thin Films	103
5.2 Gas Diffusion Measurements in Matrimid 5218	104
5.2.1 Sample Preparation of Matrimid 5218 film Deposited on the QCM	104
5.2.2 Gas Diffusion Analysis in Matrimid 5218	105
5.3 Gas Diffusion Measurements in 6FDA-DAM	109
5.3.1 Sample Preparation, Deposition and Characterization of 6FDA-DAM film Deposited on the QCM	109
5.3.2 Gas Diffusion Analysis in 6FDA-DAM	109
5.4 Theory of Diffusion in a Porous Solid Particles	112
5.5 Gas Diffusion Measurements in MOFs	113
5.5.1 Sample Preparation, Deposition and Characterization of Cu-hfipbb Crystals (small and large crystals) Deposited on the QCM	113
5.5.2 Gas Diffusion Analysis in Cu-hfipbb Crystals (small and large crystals)	113
5.6 Conclusions	118
CHAPTER 6: CONCLUSIONS AND RECOMMENDATIONS FOR FUTURE WORK	120
6.1 Conclusions	120
6.2 Future work	123

6.2.1 Improvements to the Electrical Instrumentation and Data Acquisition System	124
6.2.3 Synchronized Approach with Piezoresistive Microcantilever	129
APPENDIX A	131
A.1 Snapshot the Experimental Setup	131
APPENDIX B	133
B.1 Improvement in QCM Cell Design	133
REFERENCES	138

List of Tables

Table 3.1 Comparison of thermodynamic adsorption parameters obtained from CO ₂ adsorption in Matrimid 5218 using the QCM-based sorption apparatus with the corresponding parameters obtained from gravimetric measurements [53]	42
Table 3.2 Average relative error (%) between the experimental data and the dual mode adsorption model for CO ₂ gas adsorption in Matrimid 5218[71].	43
Table 3.3 CO ₂ adsorption parameters for Matrimid 5218 obtained from the QCM-based measurement, and compared to parameters obtained from literature [53, 71].	47
Table 3.4 CH ₄ adsorption parameters for Matrimid 5218 obtained from the QCM-based measurement, and compared to parameters obtained from literature.[53]	47
Table 3.5 Average relative error (%) between the experimental data and the dual mode adsorption model for CO ₂ gas adsorption in Matrimid 5218.	48
Table 3.6 Average relative error (%) between the experimental data and the dual mode adsorption model for CH ₄ gas adsorption in Matrimid 5218.	48
Table 3.7 Gas adsorption parameters for 6FDA-DAM obtained from the QCM-based measurement	52
Table 3.8 Average relative error (%) between the experimental data and the adsorption model for gas adsorption in 6FDA-DAM	53
Table 4.1 Adsorption parameters for Cu-hfipbb based on the Langmuir model.	75

Table 4.2 Average relative error (%) between the experimental data and the Langmuir adsorption model for Cu-hfipbb.	75
Table 4.3 Henry's constants for gas adsorption in ZIF-90.	77
Table 4.4 Average relative error (%) between the experimental data and the Henry's adsorption model for ZIF-90.	77
Table 4.5 Adsorption parameters for Cu-hfipbb based on the Langmuir model (CH ₄ , N ₂ and n-Butane) and dual mode adsorption model (CO ₂ and Ethylene)	83
Table 4.6 Average relative error (%) between the experimental data and the Langmuir model (CH ₄ , N ₂ and n-Butane) and dual mode adsorption model (CO ₂ and ethylene)	83
Table 4.7 Adsorption parameters for BNTs based on the Langmuir model.	91
Table 4.8 Average relative error (%) between the experimental data and the Langmuir adsorption model for BNTs.	91
Table 4.9 Comparison of Langmuir adsorption model parameters between BNT's and ANT's for the sub-atmospheric pressure range	97
Table 4.10 Average relative error (ARE in %) between the Langmuir adsorption model and the experimental data	97
Table 4.11 Henry's constant ratio between ANT and BNT (K_{ANT}/K_{BNT}) for three adsorbates.	99
Table 4.12 Fitted Langmuir parameters of the gas adsorption isotherms. The product of C_l and α is the Henry's constant K	99

List of Figures

- Figure 1.1** (A) Structure of $\text{Cu}(\text{hfipbb})(\text{H}_2\text{hfipbb})_{0.5}$ in the longitudinal direction, (B) Topology of the ZIF-90 structure in the diagonal direction, (C) Structure of nonfunctionalized AlSiNTs (BNTs), (D) Structure of amine functionalized AlSiNTs (ANTs) 13
- Figure 1.2** (A) Chemical structure of Matrimid 5218 [53], (B) Chemical structure of 6FDA-DAM [69] 14
- Figure 2.1.** 3D rendering of the high pressure/ high temperature cell showing the $\frac{1}{4}$ " gas outlet connecting to the gas inlet/outlet system, Bayonet-Neill-Concelman (BNC) type connection to the phase lock oscillator (PLO) to measure the resonant frequency of the quartz crystal microbalance (QCM), thermocouples to measure the temperature inside the chamber and the high temperature O-ring to seal the chamber 16
- Figure 2.2.** Cut-section view of the high pressure/ high temperature cell showing the dimensions of the chamber 17
- Figure 2.3** Illustrations of Quartz Crystal Microbalance (QCM) used in our experiments. 21
- Figure 2.4** Schematic of the experimental setup [71] 23
- Figure 2.5** Labview© program recording the raw data for CO_2 gas adsorption in Cu-hfipbb MOF. 24
- Figure 2.6** (A) Inficon 1" Crystal – electrode configuration, (B) Inficon 1" Crystal as seen from the front side [72] 26
- Figure 2.7** Schematic of the principle of operation of QCM 26

Figure 2.8 Simple molecular model for explaining piezoelectric effect: (A) unperturbed molecule; (B) molecule subjected to an external force; and (C) polarizing effect on material surface [73]; (D) electrical circuit model of the QCM	28
Figure 2.9 Frequency change versus temperature for the 5 MHz, 25°C AT- cut QCM	29
Figure 3.1 Structure of Matrimid 5218 polyimide [59]	37
Figure 3.2 Structure of 6FDA-DAM polyimide [83]	38
Figure 3.3 SEM images of Matrimid 5218 deposited on the QCM show island deposition	39
Figure 3.4 (A) SEM images of continuous thin films of Matrimid 5218 film deposited on the QCM; (B) edge of the film as evidenced by the sliver of gold	40
Figure 3.5 Solubility of CO ₂ at STP per unit volume of Matrimid® 5218 at different temperatures as measured by the in-house developed Quartz Crystal Microbalance (QCM) sorption apparatus. The solid lines represent the dual mode isotherm model fit	42
Figure 3.6 Solubility of gases at STP per unit volume of Matrimid® 5218 at different temperatures as measured by the QCM technique (A) Solubility of CO ₂ at STP per unit volume of Matrimid® 5218 (B) Solubility of CH ₄ at STP per unit volume of Matrimid® 5218. Solid lines represent the dual mode isotherm fit.	46
Figure 3.7 Solubility of gases at STP per unit volume of 6FDA-DAM at different temperatures as measured by the QCM technique. (A) Solubility of CO ₂ at STP, (B) Solubility of CH ₄ at STP, (C) Solubility of CH ₄ at STP	

represented up to 1 atm and (D) Solubility of n-C ₄ H ₁₀ at STP. Solid lines represent the Dual Mode isotherm fit for (A) CO ₂ and (D) n-C ₄ H ₁₀ and Henry's Fit for (C) CH ₄ .	51
Figure 4.1 Structure of the Cu-hfipbb MOF [71]	59
Figure 4.2 Structure of ZIF-90[71]	60
Figure 4.3 Structure of the (A) Bare aluminosilicate nanotubes (BNTs), (B) 15 % methylamine functionalized aluminosilicate nanotubes (ANTs)	62
Figure 4.4 Cu-hfipbb crystals deposited on the gold surface of the QCM.	64
Figure 4.5 XRD patterns of Cu-hfipbb crystals taken before (marked as 2) and after (marked as 3) adsorption measurements, and comparison with the simulated XRD patterns of the crystal structures (marked as 1).	65
Figure 4.6 ZIF-90 crystals deposited on the gold surface of the QCM.	67
Figure 4.7 XRD patterns of ZIF-90 crystals, taken before (marked as 2) and after (marked as 3) adsorption measurements, and comparison with the simulated XRD patterns of the crystal structures (marked as 1).	67
Figure 4.8 Cu-hfipbb crystals deposited on the gold surface of the QCM. (A) crystals obtained after 6 hrs of synthesis, (B) crystals obtained after 24 hr synthesis	69
Figure 4.9 XRD patterns of Cu-hfipbb crystals taken before (Pre exp) and after (Post exp) adsorption measurements, and compared with the simulated and synthesized crystals (6 hr synthesis and 24 hr synthesis time) XRD patterns of the crystal structures.	70

Figure 4.10 Solubility of gases (in cc STP/g) at 25°C (only CO₂), 30°C, 50°C and 70°C in the MOF Cu-hfipbb. (A) CO₂ adsorption isotherms at different temperatures, with a gravimetrically-measured CO₂ adsorption isotherm at 25°C; (B) CH₄ and (C) N₂ adsorption isotherms at different temperatures. Langmuir model fits are represented by the solid lines. 74

Figure 4.11 Solubility of gases (in cc STP/g) at 30°C, 50°C and 70°C in the MOF ZIF-90. CO₂ (A & B), CH₄ (C & D), and N₂ (E & F) adsorption isotherms for the entire pressure range studied, and the sub-atmospheric pressure range, respectively. Henry's constant is fitted in the sub-atmospheric pressure range as represented by the solid lines. 78

Figure 4.12 Solubility of gases (in cc STP/g) at different temperatures in the MOF Cu-hfipbb. (A) CO₂ adsorption isotherms at different temperatures, (B) CH₄ and (C) N₂, (D) Ethylene and (E) n-Butane. The fits with simple analytical models like Langmuir (for CH₄, N₂ and n-Butane) and dual mode adsorption model (CO₂ and Ethylene) are represented by the solid lines. 81

Figure 4.13 Comparison of gas adsorption isotherm obtained from large and small sized Cu-hfipbb crystals at different temperatures. (A) CO₂, (B) CH₄ and (C) N₂. Isotherms obtained from large sized Cu-hfipbb crystals are represented by markers and that obtained from small sized Cu-hfipbb crystals are represented by solid lines, 82

Figure 4.14 XRD pattern obtained from BNTs deposited on the QCM 87

Figure 4.15 XRD pattern obtained from ANTs deposited on the QCM 87

Figure 4.16 Solubility of gases (in cc STP/g) at 25°C, 48°C and 67°C in the BNTs.

(A) CO₂ adsorption isotherms at different temperatures. (B) CH₄ and (C) N₂ adsorption isotherms at different temperatures. Langmuir model fits are represented by the solid lines. 90

Figure 4.17 Solubility of CO₂ (in cc STP/g) at 25°C, 48°C and 67°C in the ANTs (A & C) and Bare AlSi NTs (B & D). Adsorption isotherms for the entire pressure range (0-120 psi) presented in (A & B) and the sub-atmospheric pressure range (C & D), respectively. Langmuir adsorption model is fitted in the sub-atmospheric pressure range as represented by the solid lines (C & D). 94

Figure 4.18 Solubility of CH₄ (in cc STP/g) at 25°C, 48°C and 67°C in the ANTs (A & C) and Bare AlSi NTs (B & D). Adsorption isotherms for the entire pressure range (0-120 psi) presented in (A & B) and the sub-atmospheric pressure range (C & D), respectively. Langmuir adsorption model is fitted in the sub-atmospheric pressure range as represented by the solid lines (C & D). 95

Figure 4.19 Solubility of N₂ (in cc STP/g) at 25°C, 48°C and 67°C in the ANTs (A & C) and Bare AlSi NTs (B & D). Adsorption isotherms for the entire pressure range (0-120 psi) presented in (A & B) and the sub-atmospheric pressure range (C & D), respectively. Langmuir adsorption model is fitted in the sub-atmospheric pressure range as represented by the solid lines (C & D). 96

- Figure 4.20** Comparison of adsorption selectivity between BNTs and ANTs at different temperatures. (A) CO₂/CH₄ adsorption selectivity for ANTs, (B) CO₂/CH₄ adsorption selectivity for BNTs, (C) CO₂/N₂ adsorption selectivity for ANTs, (D) CO₂/N₂ adsorption selectivity for BNTs 98
- Figure 4.21** The adsorption isotherms of (A) CO₂ at 25 °C, (B) CO₂ at 67 °C, (C) CH₄ at 25 °C, (D) CH₄ at 67 °C, (E) N₂ at 25 °C, and (F) N₂ at 67 °C for BNTs (blue diamonds) and ANTs (red squares); and the fitted curves (solid lines) of the Langmuir model. 100
- Figure 5.1** Typical fit of the experimental transient data with fitted equation (equation 5.4) for Matrimid 5218. 106
- Figure 5.2** Gas diffusion coefficients vs pressure at different temperatures in Matrimid 5218 for (A) CO₂ and (B) CH₄, (C) Average gas diffusion coefficients (based on all pressures) at different temperatures. 107
- Figure 5.3** Permeability of gases in Matrimid 5218 at different temperatures compared with literature data [59] (A) CO₂ permeability (B) CH₄ permeability 108
- Figure 5.4** Typical fit of the experimental transient data with the fitted equation (equation 5.4) for 6FDA-DAM 110
- Figure 5.5** (A) Gas diffusion coefficients vs pressure at different temperatures for n-Butane in 6FDA-DAM, (B) Permeability of n-Butane in 6FDA-DAM at different temperatures compared with literature data. 111
- Figure 5.6** (A) Typical fit of the experimental transient data with the fitted equation (equation 5.11) for CO₂ in Cu-hfipbb MOF, (B) Typical fit of the

experimental transient data with the fitted equation (equation 5.11) for other gases in Cu-hfipbb MOF	115
Figure 5.7 Gas diffusion time scale vs pressure at different temperatures in Cu-hfipbb for (A) CH ₄ , (B) N ₂ , (C) Ethylene and (D) n-Butane	116
Figure 5.8 Diffusion selectivity of ethylene over n-Butane in Cu-hfipbb MOF. The lines connecting the points are only a guide to the eye.	117
Figure 5.9 Comparison of diffusion time scale obtained from large and small sized Cu-hfipbb crystals for (A) CO ₂ and (B) CH ₄	118
Figure 6.1 Schematic of the suggested multicomponent gas sorption apparatus.	125
Figure 6.2 Schematic diagram of the chamber head to be developed	127
Figure 6.3 Schematic view of the chamber bottom	128
Figure 6.4 Schematic diagram of the cut section view of the chamber bottom	128
Figure A.1 Labeled photograph of the QCM-based adsorption measurement apparatus. Inset 1 shows the frequency counter, voltmeter, PID temperature controller and pressure reader. Inset 1a shows the phase lock oscillator used to measure the resonant frequency. Inset 2 and 2a shows the detailed view of the high temperature, high pressure stainless steel chamber with the heating jacket. 3 represent the gas cylinder used for dosing gas to the chamber.	131
Figure A.2 Comparison of gas adsorption measurements between sample 1 and sample 2 of the small sized Cu-hfipbb MOF crystals at 30°C (Refer section 4.4.1)	132

Figure B.1 Schematic diagram of the gas feed system for the multi component QCM based adsorption setup	133
Figure B.2 Schematic diagram of the temperature measurement module	134
Figure B.3 Schematic view of the pressure measurement module	135
Figure B.4 Schematic representation of the exit gas analyzer module connecting the sample chamber to the GC/MS set up	135
Figure B.5 Detailed schematic view of the gas feed valve fittings to connect the sample chamber to the dosing gas cylinder	136
Figure B.6 Detailed schematic view of the pressure gauge fittings between the sample chamber and pressure transducer	136
Figure B.7 Detailed schematic view of the exit gas analyzer fitting to connecting the sample chamber to first shut off valve downstream.	137

Nomenclature

6FDA-DAM	(2,2-bis(3,4-carboxyphenyl) hexafluoropropane dianhydride–diaminomesitylene)
AlSiNTs	aluminosilicate nanotubes
AMTES	aminomethyltriethoxysilane
ANTs	amine-functionalized aluminosilicate nanotubes
APTES	aminopropyltriethoxysilane
ARE	Average relative error (%)
BNC	Bayonet-Neill-Concelman
BNTs	bare/non-functionalized aluminosilicate Nanotubes
Cu-hfipbb	Cu(hfipbb)(4,4'-hexafluoro-isopropylidene-bis-benzoate) _{0.5}
ImCA	Imidazole Carboxyaldehyde
Matrimid 5218	diamine, 5(6)-amino-1-(4' aminophenyl)-1,3,-trimethylindane
MOF	Metal Organic Framework
MTES	methyltriethoxysilane
PID	Proportional Integral Derivative
PLO	Phase Lock Oscillator
QCM	Quartz Crystal Microbalance
SEM	Scanning Electron Microscopy
SWNTs	single-walled nanotubes
TEOS	tetraethylorthosilicate
XRD	X-ray Diffraction
ZIF-90	Zeolitic Imidazolate Framework - 90

Summary

Nanoporous molecular sieve materials have found a wide range of technological applications in catalysis, separations, and ion exchange. Recently, novel nanoporous materials like Metal Organic Frameworks (MOFs) and Metal Oxide Nanotubes have gained impetus due to their ultra high internal surface areas, modifiable pore structure and chemistry, and good chemical and thermal stability. As a result, there is great interest in their use as permselective membrane materials, adsorbents, and catalysts. In addition, polymeric materials continue to attract significant interest as membranes and adsorbents. Due to the large number of nanoporous and polymeric materials available, hierarchical screening and selection strategies based upon combined computational and experimental methods are emerging. For experimental characterization of candidate materials for adsorption and membrane applications, it is desirable to obtain measurements from small amounts of synthesized sample before a larger synthesis and characterization effort is made for promising materials. In the case of membrane materials (such as polymers and some MOFs), it is also desirable to obtain direct measurements on thin films. However, the characterization of gas adsorption and diffusion in porous materials is performed predominantly by commercial gravimetric equipment, whose capital and operating costs are high and require relatively large amounts of powder sample (typically > 200 mg) to obtain accurate data.

The overall objective of this thesis is to investigate the adsorption and diffusion characteristics of nanoporous and polymer materials of high interest in adsorption and membrane applications, *via* the development and use of a high-pressure/high-temperature quartz crystal microbalance (QCM) device which is capable of measurements on powders

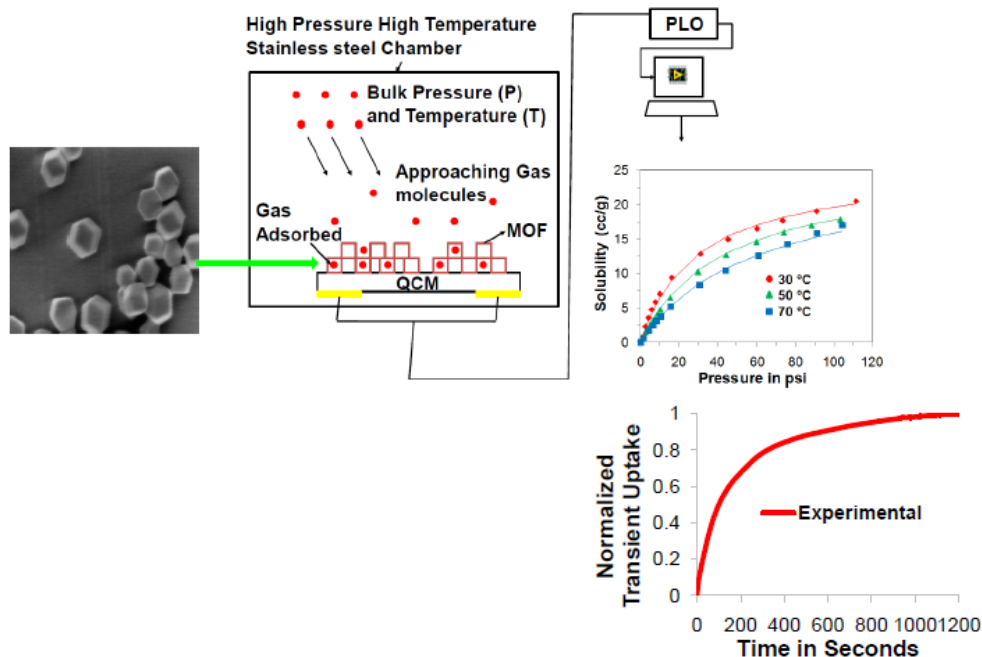
and thin films with small (< 1 mg) amounts of sample. In this regard, the thesis is divided into four parts, *viz*

- (1) Design and development of high temperature/ high pressure QCM device.
- (2) Measurement and analysis of adsorption characteristics in nanoporous materials.
- (3) Diffusion measurement and analysis in polymer thin films.
- (4) Diffusion measurement and analysis in MOF crystals.

Unlike gravimetric methods, the QCM resonant frequency measurements can be made to a high precision, thereby allowing operation with very small amounts of sample. In the first part of this thesis, the measurement theory, design, and construction of the instrument along with validation data from a polyimide material, Matrimid 5218 is described. In the second part, the use of the instrument to examine gas adsorption characteristics of two interesting MOF materials - namely $\text{Cu}(\text{hfipbb})(4,4'$ -hexafluoroisopropylidene-bis-benzoate) $)_{0.5}$ (referred to as Cu-hfipbb) and Zeolitic Imidazolate Framework-90 (ZIF-90) – and an inorganic nanoporous material (single-walled aluminosilicate nanotubes) is described. The adsorption properties of gases such as CO_2 , CH_4 , N_2 , ethylene and n-Butane were obtained and analyzed with adsorption models to obtain and understand the fundamental adsorption parameters. In the case of the nanotube material, our main result is the comparison of their adsorption properties in their non-functionalized form and in their amine-functionalized form, which revealed interesting performance enhancements upon functionalization.

In the third part of this thesis, the applications of the QCM-based setup to obtain information on molecular diffusion over a range of temperature and pressure conditions from polymeric thin films directly deposited on QCM substrates is examined. Detailed measurements and analysis of gas diffusion properties from two polyimide materials of interest, namely Matrimid 5218 and 6FDA-DAM is presented. In the final part of the thesis, the application of the QCM-based setup to obtain diffusion information from powder samples of MOF materials such as Cu-hfipbb is examined.

Overall, this work has demonstrated a sound basis for wider application of microanalytical techniques, specifically QCM-based measurements, in fundamental research on adsorption and diffusion in porous materials. A schematic representation of this research is presented below and its detailed meaning will be elucidated in the thesis.



CHAPTER 1: INTRODUCTION

1.1 Nanoporous Materials

Nanoporous molecular sieve materials have found a wide range of technological applications in catalysis, separations, sensing and ion exchange [1]. Recent improvements in our abilities to manipulate on the nanoscale are transforming our use of these materials from the merely opportunistic to directed design. This is most strikingly the case in the creation of a wide variety of membranes where control over pore size is increasing dramatically, often to atomic levels of perfection, as is the ability to modify physical and chemical characteristics of the materials that make up the pores.

The whole spectrum of available nanoporous materials can be broadly classified based on the size of pores. According to IUPAC classification on the pore size of nanoporous materials, pores between 0-2 nm are classified as micropore, pores between 2-50 nm as mesopore and pores >50 nm as macropore. There may be other criteria such as type of network material and shape of pores which are not discussed explicitly here [2]. In this thesis, microporous materials are predominantly studied for their gas separation properties. In particular, attention is given to Metal Organic Frameworks (MOFs) and Metal Oxide Nanotubes.

1.1.1 Metal Organic Frameworks (MOFs)

Recently, a new class of nanoporous materials known as Metal Organic Frameworks (MOFs) [3] have gained impetus due to their salient features which include ultra-high surface areas ($> 6000 \text{ m}^2 \text{ g}^{-1}$ has been reported), pore structure and chemistry that can be modified using rational synthetic design and a high degree of chemical and

thermal stability. MOFs have monolithic pore dimensions comparable in size to zeolites, achieved by coupling inorganic clusters with organic “linker” groups [4]. A typical MOF consists of metal cations such as Zn (II) linked by anionic organic linker groups such as carboxylates, yielding a relatively rigid, but open framework that can accommodate guest molecules. As a result, MOFs can function as a chemical recognition layer in chemical sensors that rely on analyte adsorption. Several reports of their use in the fabrication of membranes for gas separations have appeared [5-8]. Their use in adsorption-based applications is also an area of great interest, and they have been shown to selectively adsorb specific gas molecules from mixtures [9-17].

Due to the importance of MOFs as membrane materials and adsorbents, and considering the large number of MOF materials available, there is a need to develop efficient strategies for screening and measuring the adsorption characteristics of key MOF materials for a given potential application. Research groups at Georgia Tech have recently proposed such a strategy to enable the use of MOFs in gas separation membrane and adsorption applications. The first step of this strategy involves the use of computational approaches to screen large numbers of MOF materials and predict their effectiveness for a particular separation via a hierarchical series of molecular simulations [18, 19]. Through this method, large numbers of MOFs can be eliminated as being unsuitable for a particular application, and a reasonable number of potentially suitable MOF materials are predicted, which then become the target of more focused and efficient experimentation to determine the adsorption and diffusion characteristics.

Thus through this computational screening, two important MOF materials identified for gas separation applications by computational screening were selected [19].

The two MOF materials of interest are $\text{Cu}(\text{hfipbb})(4,4'\text{-hexafluoroisopropylidene-bis-benzoate})_{0.5}$ (referred to as Cu-hfipbb) and Zeolitic Imidazolate Framework-90 (ZIF-90). Cu-hfipbb and ZIF-90 has been the subject of several recent works that investigate their CO_2 , CH_4 , and N_2 gas adsorption/transport properties computationally and through the fabrication of membranes [5, 18-20]. Cu-hfipbb is a crystalline interpenetrating framework containing 1D channels, and is based on a $\text{Cu}_2(\text{hfipbb})_4(\text{H}_2\text{hfipbb})_2$ paddle-wheel building unit (Figure 1.1A). This MOF has cages of effective pore dimensions $5.1 \text{ \AA} \times 5.1 \text{ \AA}$ connected by small windows of dimensions $3.5 \text{ \AA} \times 3.2 \text{ \AA}$ [19]. The topology of the ZIF-90 structure is identical to the sodalite silicate topology. The crystal structure comprises of Zn(II) centers linked by imidazolate-2-carboxyaldehyde (ICA) molecules (Figure 1.1B). This leads to a ZIF structure containing cages of size 11.2 \AA connected by windows of size 3.5 \AA [21]. Although previous authors have fabricated and tested membranes containing ZIF-90 and Cu-hfipbb, very little was known about the intrinsic adsorption and transport properties of this material. Hence these materials were studied in this research.

1.1.2 Single Wall Nanotubes (SWNTs)

In addition to the MOFs, another microporous material that has been studied in this thesis is the Single Walled Nanotubes (SWNTs). Nanotubular materials are important “building blocks” of nanotechnology, based upon their incorporation into nanoscale devices. In particular, the synthesis and applications of carbon nanotubes have been extensively studied for over two decades [22-27]. One of the application areas has been the use of carbon nanotubes for molecular separations, owing to some of their unique

properties. One such important property, extremely fast mass transport of molecules within carbon nanotubes associated with their low friction inner nanotube surfaces, has been demonstrated via computational and experimental studies [28-32]. Furthermore, the behavior of adsorbate molecules in nano-confinement is fundamentally different than in the bulk phase, which could lead to the design of new sorbents [33]. Finally, their one-dimensional geometry could allow for alignment in desirable orientations [34-36] for given separation devices to optimize the mass transport. Despite possessing such attractive properties, several intrinsic limitations of carbon nanotubes inhibit their application in large scale separation processes: the high cost of carbon nanotube synthesis and membrane formation (by microfabrication processes), as well as their lack of surface functionality, which significantly limits their molecular selectivity. Although outer-surface modification of carbon nanotubes has been developed for nearly two decades [37-39], interior modification via covalent chemistry is still challenging due to the low reactivity of the inner-surface [40]. Hence, the interior functionalization of carbon nanotubes remains a challenge.

These high barriers facing the use of carbon nanotubes in membranes can be compared with certain favorable properties of metal oxide nanotubes. In particular, metal oxide nanotubes have a much lower cost due to moderate synthesis conditions (usually hydrothermal or solvothermal), higher surface reactivity (similar to a metal oxide or hydroxide) that is advantageous to surface modification, and controllable dimensions (such as length in the ~20-500 nm range), which can allow fabrication of thin membranes [41, 42]. The present work will focus on a specific single-walled metal oxide nanotube (SWNT) with an aluminosilicate composition [27]. This SWNT is the synthetic analog of

the nanotubular mineral imogolite, and has created substantial interest in recent years [43-46]. It possesses several unique and attractive properties for molecular transport and adsorption and membrane formation, such as controllable and monodisperse dimensions [45, 47], extraordinary hydrophilicity and surface silanol density [48], and fast mass transport (e.g. for water and alcohols) [27, 29, 32, 49]. The inner surface of the aluminosilicate SWNT can be expected to resemble those of metal oxide/hydroxide and silicate materials, and thus are more amenable to surface modification than carbon nanotubes. The aluminosilicate SWNTs contain silanol (Si-OH) groups on the inner surface and hence can potentially be functionalized in a manner analogous to the well-known techniques for functionalization of mesoporous and microporous silicas [50, 51]. On the other hand, the hydroxyl groups at the external surfaces of aluminosilicate SWNTs may possess good affinity to hydrophilic polymers [52]. This could open the route for fabricating high-quality nanotube/polymer membranes [27].

1.2 Polymers

Over the last decade, polymeric membranes have been proven to operate successfully in certain industrial gas separations. To obtain membranes that combine high permeability and high selectivity together with thermal stability, new polymers called high-performance polymers, were developed like polyimide (PI), poly(phenyl oxide) (PPO), poly(trimethylsilylpropyne) (PTMSP), and polytriazole [53]. Among these, Polyimides are an important class of polymer for membrane gas separation, used, for example, in carbondioxide and hydrogen sulfide separation during the sweetening of natural gas. The commercially produced polyimide, 3,3'-4,4'-benzophenone

tetracarboxylic-dianhydride diaminophenylindane (BTDA-DAPI), commonly known as Matrimid 5218, is a polyimide widely used in industry because of its promising properties when separating gas mixtures [53]. There have been few quantitative studies on the sorption behavior of gases within Matrimid films. Punsalan and Koros reported on CO₂ sorption in Matrimid as part of an aging study [54] as well as a membrane thickness study [55], while Burns and Koros have examined Matrimid sorption for propane/propylene separation [56]. Moore and Koros [57] reported on CH₄ sorption as part of a mixed matrix membrane study, and similarly Chung et al. [58] has reported on CO₂ and CH₄ sorption in Matrimid as a result of a mixed matrix membrane with C₆₀. Scholes et al. [53] presented a quantitative study in the sorption behavior of CO₂, N₂, CH₄ as well as water vapor in Matrimid 5218 over a range of temperature. Availability of such extensive data on adsorption behavior in Matrimid 5218 piqued our interest in studying this material as a membrane material for gas separation. With regard to the permeation property also there have been few studies. Recent report by Zhao et al. [59] studied the permeability of pure gas CO₂, CH₄, N₂ and H₂ at different temperatures in Matrimid 5218 and its modifications at a constant pressure. Song et al. [60] studied the permeability of pure gas H₂, CO₂, CH₄, N₂ and O₂ at different temperatures in Matrimid 5218 and its modifications as a mixed matrix membrane with ZIF-8 at a constant pressure. However there is no known study on the behavior of its permeation properties with respect to pressure at different temperatures.

In addition to Matrimid, another polymer material studied was 6FDA-DAM. 6FDA-DAM also known as (2,2-bis(3,4-carboxyphenyl) hexafluoro propanedianhydride–diaminomesitylene), is a polyimide widely used in industry for its ultra high permeability

and selectivity [5, 61]. However, there have been few quantitative studies on the sorption and permeation behavior of gases in 6FDA-DAM films. Liu et al. reported butane isomers permeation properties at a single temperature and different pressures for 6FDA-DAM and its modifications as a mixed matrix membrane with MFI [62]. Esekile et al. [61] reported the permeation and adsorption properties at a single temperature and different pressures for 6FDA-DAM. Cui et al. [63, 64] reported the permeation properties of 6FDA based polyimide films for O₂, N₂ and CO₂ at different pressures and a constant temperature. However, the above mentioned studies do not consider the effect of temperature or provide thermodynamic parameters of adsorption or permeation to understand its behavior as a membrane. Hence study of adsorption and permeation properties of these polyimides with respect to different temperatures and pressures may yield information on its thermodynamic properties and hence could open the route for fabricating high-quality nanoporous materials (MOFs, Nanotubes)/polymer membranes.

1.3 Motivations for this Work

The characterization of gas adsorption in these porous materials is performed predominantly by commercial equipment (Gravimetric, Volumetric or Permeation Cell). Their capital and operating costs are generally high. Furthermore, they require relatively large amounts of sample (typically > 200 mg) to obtain accurate data, and also cannot measure gas adsorption in thin films or coatings. It is desirable to broaden the range of techniques that can be used to reliably measure the adsorption properties of MOF materials over a substantial range of pressure and temperature by non-gravimetric

methods, ideally with only a small sample size requirement (< 1 mg), and with the sample being potentially in powder deposition or thin film form.

1.4 Objectives of this Thesis

The overall objective of this thesis research is to investigate the adsorption and diffusion characteristics of nanoporous materials through the development and use of a high-pressure/high-temperature quartz crystal microbalance (QCM) device. In this regard, the proposed research is divided into four main objectives,

1. Design and development of high temperature/ high pressure QCM device
2. Measurement and analysis of adsorption characteristics in nanoporous materials
3. Diffusion measurement and analysis in polymer thin films
4. Diffusion measurement and analysis in MOF crystals.

The results obtained in Objectives 2-4 will allow us to make important recommendations regarding the use of specific nanoporous materials in molecular separation applications, and will also lead to significant fundamental knowledge of adsorption thermodynamics in these nanoporous materials via the application of analytical adsorption models to the experimental data. Further, the use of QCM based technique in our current setup yields both the adsorption and diffusion characteristics from the same sample at different temperatures and pressures. The permeation parameters can then be calculated from the adsorption and diffusion data thus enhancing the flexibility in measurements.

1.5 Significance of Quartz Crystal Microbalance (QCM) - Based Adsorption and Diffusion Measurements

The QCM measures changes in the mass of material deposited on a piezoelectric quartz substrate by measuring the change in its resonant frequency resulting from mass addition. QCM devices have been shown to be effective in vacuum, gas phase, and (more recently) in liquid environments [65, 66]. Unlike gravimetric measurements, the resonant frequency measurements can be easily made to a high precision, thereby allowing operation with very small amounts of sample and buoyancy corrections are not required. In addition to the resonant frequency, the method also yields data on the dissipation (damping) in the system, and thereby allows quantification of the sample's elastic properties that may be useful in thin film/membrane applications. A QCM system can be constructed for a fraction (~20%) of the cost of a gravimetric apparatus. Recent reports have investigated the use of flow cell based QCM techniques for measuring the adsorption and diffusion of Volatile Organic Compounds (VOCs) in MOF materials [67, 68]. However, the capability to perform accurate QCM-based adsorption measurements over a comprehensive range of temperature and pressure remains a desirable goal. Detailed description of the experimental setup and the theory of measurement is given in subsequent chapters.

1.6 Topics Covered in this Thesis

In this thesis, we present in detail the design considerations, description and the theory of measurement of the QCM based gas sensing apparatus developed (**Chapter 2**). Upon completion of the construction of the setup, the instrument was validated with

Matrimid 5218 (powder type deposition) which produced excellent degree of conformance with reported values (**Chapter 3**). In addition to the adsorption data from Matrimid 5218 (powder type deposition), we also present the gas adsorption measurement and analysis from Matrimid 5218 and 6FDA-DAM films deposited on the QCM (**Chapter 3**). We then characterized the gas adsorption characteristics of important MOF materials, identified for gas separation applications by computational screening [19] (**Chapter 4**). The two MOF materials of interest are Cu(hfipbb)(4,4'-hexafluoroisopropylidene-bis-benzoate)_{0.5} (referred to as Cu-hfipbb) and Zeolitic Imidazolate Framework-90 (ZIF-90). Cu-hfipbb and ZIF-90 has been the subject of several recent works that investigate their CO₂, CH₄, and N₂ gas adsorption/transport properties computationally and through the fabrication of membranes [5, 18-20]. Cu-hfipbb is a crystalline interpenetrating framework containing 1D channels, and is based on a Cu₂(hfipbb)₄(H₂hfipbb)₂ paddle-wheel building unit (Figure 1.1A). This MOF has cages of effective pore dimensions 5.1 Å x 5.1 Å connected by small windows of dimensions 3.5 Å x 3.2 Å [19]. The topology of the ZIF-90 structure is identical to the sodalite silicate topology. The crystal structure comprises of Zn(II) centers linked by imidazolate-2-carboxyaldehyde (ICA) molecules (Figure 1.1B). This leads to a ZIF structure containing cages of size 11.2 Å connected by windows of size 3.5 Å [21]. From our analysis we found that adsorption in the 1-D channels of Cu-hfipbb can be well described by a single-site Langmuir model. On the other hand, adsorption in ZIF-90 follows a more complex behavior, commensurate with its pore structure consisting of large porous cages connected in three dimensions by small windows. In both materials, the order of adsorption strength is CO₂ > CH₄ > N₂. Although previous authors have

fabricated and tested membranes containing ZIF-90 and Cu-hfipbb, very little was known about the intrinsic adsorption and transport properties of this material.

Following the gas adsorption results from MOFs, gas uptake measurements in AlSiNTs are presented (**Chapter 4**). This type of nanotube consists of an octahedral aluminum(III) hydroxide outer wall and a tetrahedral silanol inner wall, with doubly-coordinated hydroxyl groups on the outer wall and pendant hydroxyls on the inner wall. Here we present the gas adsorption results from single-walled amine-functionalized Aluminosilicate Nanotubes (ANTs) with up to 15% of the interior $\equiv\text{Si-OH}$ groups substituted by $\equiv\text{Si-CH}_2\text{NH}_2$ groups, *via* the use of an in-house-synthesized precursor (aminomethyltriethoxysilane, AMTES) and compare them against nonfunctionalized Aluminosilicate Nanotubes (BNTs) (Figure 1.1C & D). The pore diameters of these nanotubes are ~ 1 nm and vary in length between 20-500 nm. Similar to the Cu-hfipbb and ZIF-90 MOFs, gas adsorption for CO_2 , CH_4 , and N_2 gases for these nanotubes were measured and quantitative insights on the adsorption thermodynamics of these gases in these materials are obtained. From our results, the amine-functionalized nanotubes (ANTs) show a dramatic improvement in CO_2/CH_4 and CO_2/N_2 adsorptive selectivity over the bare nanotubes (BNTs). Thus the versatility of the QCM based setup to obtain adsorption measurements is demonstrated and can be used to provide recommendations on the use of interesting gas sensing materials.

As a part of our third objective, polymer films of Matrimid 5218 and 6FDA-DAM were spun on to the QCM substrate and were subjected to gas uptake experiments from which adsorption and permeation parameters were measured (**Chapter 5**). The reason for this experiment is twofold. Our initial goal was to validate the capability of the sorption

apparatus to measure diffusion coefficients and hence the permeation parameters. Further, from our literature search it was observed that, even though previous work with Matrimid 5218 and 6FDA – DAM were performed with regard to its adsorption and permeation parameters, it was incomplete in its analysis with respect to the effect of temperature and pressure. Hence the second goal of this experiment was to study the adsorption and permeation properties in these polyimides with respect to different temperatures and pressures which could yield information on the thermodynamic properties of adsorption and diffusion and could open the route for fabricating high-quality nanoporous materials/polymer membranes. Based on the experiments with Matrimid 5218 and 6FDA-DAM (Figure 1.2 A & B respectively), strong agreement with the literature was observed. Further experiments with 6FDA-DAM thin film revealed the limitations of the setup in measuring the diffusion coefficients of fast diffusing species. From the overall analysis it was observed that in the case of Matrimid 5218 thin film, the adsorption favorability for $\text{CO}_2 > \text{CH}_4$, whereas the diffusion time scale of $\text{CH}_4 > \text{CO}_2$. In the case of 6FDA-DAM thin film, it was observed that that the adsorption favorability followed $n\text{-C}_4\text{H}_{10} > \text{CO}_2 > \text{CH}_4$. Regarding the diffusion measurements for 6FDA-DAM thin film, since reliable parameters with CO_2 and CH_4 could not be obtained, only diffusion and permeation parameters with $n\text{-C}_4\text{H}_{10}$ were obtained.

Subsequently, we study the adsorption and diffusion properties in the microporous Cu-hfipbb MOF with respect to CO_2 , CH_4 , N_2 , n-Butane and Ethylene (**Chapter 5**). Based on the experimental measurements, we found that the adsorption favorability followed the order $n\text{-Butane} > \text{CO}_2 > \text{Ethylene} > \text{CH}_4 > \text{N}_2$. From our analysis we found that the diffusion time scale for CO_2 was too short to be reliably measured in

the current setup, while reliable estimates were obtained for CH₄, N₂, Ethylene and n-Butane. Based on the diffusion time scale analysis it was observed that the diffusion time scale broadly followed the order n-Butane > CH₄ > N₂ > Ethylene. Finally we conclude the thesis, highlighting the major achievement of this research and present directions for future research.

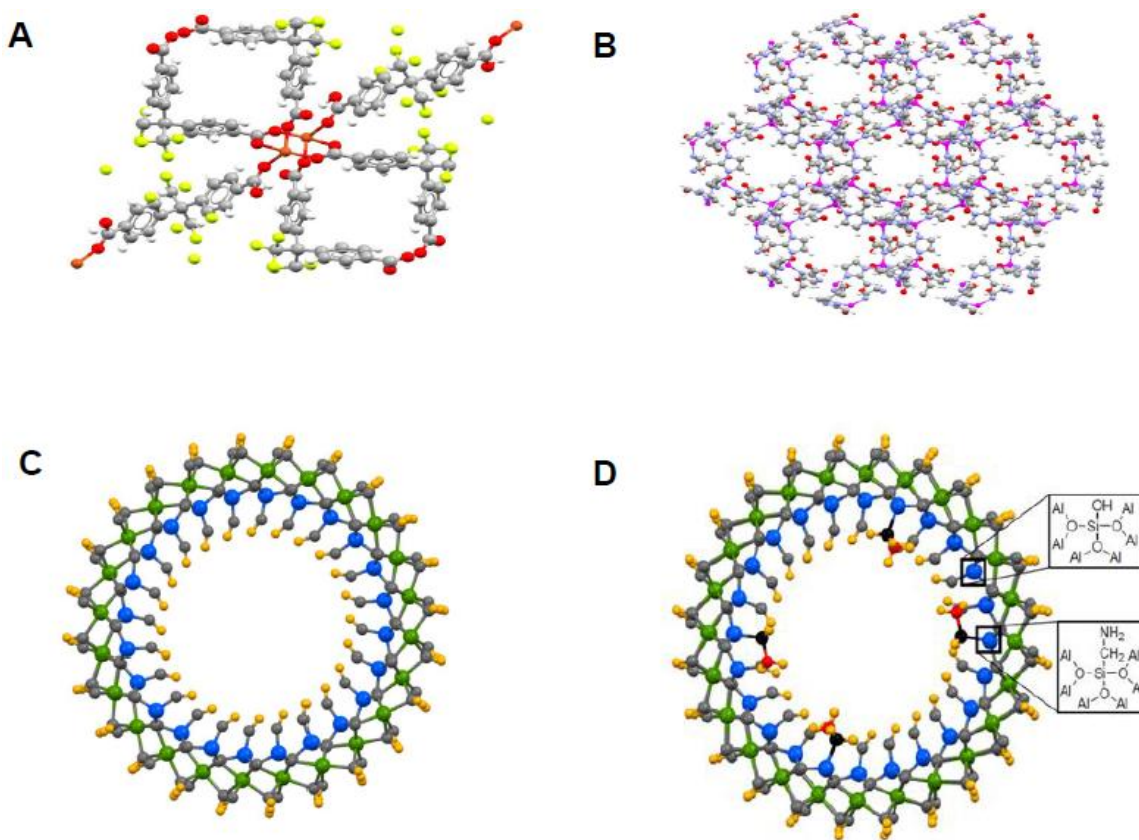


Figure 1.1 (A) Structure of Cu(hfipbb)(H₂hfipbb)_{0.5} in the longitudinal direction, (B) Topology of the ZIF-90 structure in the diagonal direction, (C) Structure of nonfunctionalized AlSiNTs (BNTs), (D) Structure of amine functionalized AlSiNTs (ANTs)

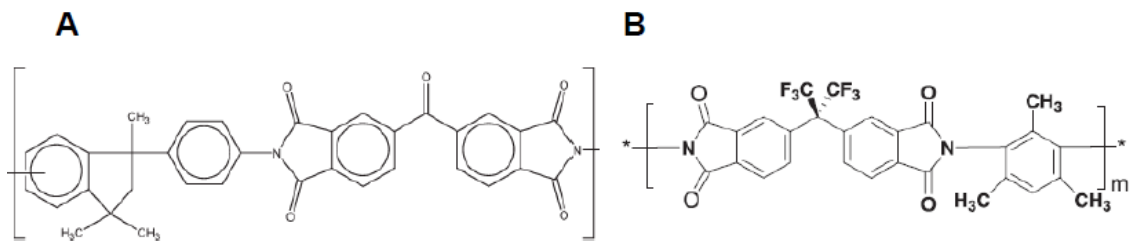


Figure 1.2 (A) Chemical structure of Matrimid 5218 [53], (B) Chemical structure of

6FDA-DAM [69]

CHAPTER 2: DESIGN, CONSTRUCTION AND THEORY OF QCM BASED APPARATUS

2.1 Design Considerations

The experimental setup was intended to measure the adsorption of single component gas in nanoporous samples at different pressures and temperatures. To achieve this goal, it was necessary to maintain the sample inside an isothermal chamber, and also to have a technique to measure the resonant frequency of the QCM. Further, the experimental setup needed to be designed to withstand pressures up to 10 bar and temperatures up to 250 °C.

2.2 Construction of the Experimental Setup

2.2.1 Design of the Stainless Steel Pressure Cell

A high pressure/high temperature stainless steel chamber with a removable chamber head was constructed. The chamber, with an inner diameter of 3", outer diameter of 4.5" and total height of 2" was constructed. The wall thickness was 0.75". The chamber head was 4.5" in diameter and 0.5" in thickness. The total internal volume of the cell was calculated to be 175 ml. The cell's overall design and cross sectional views are presented in Figure 2.1 and Figure 2.2 respectively. One of the constraints in designing the cell was that the total volume of the cell needed to be as small as possible in order to eliminate temperature variation inside the cell. Following the construction of the stainless steel chamber, the two QCMs inside the cell were mounted between the electrical connection using homemade copper clips. The clips were connected to the four

BNCs connections screwed onto the chamber head. Detailed illustrations of the experimental setup are shown in Figure A.1 in Appendix A.

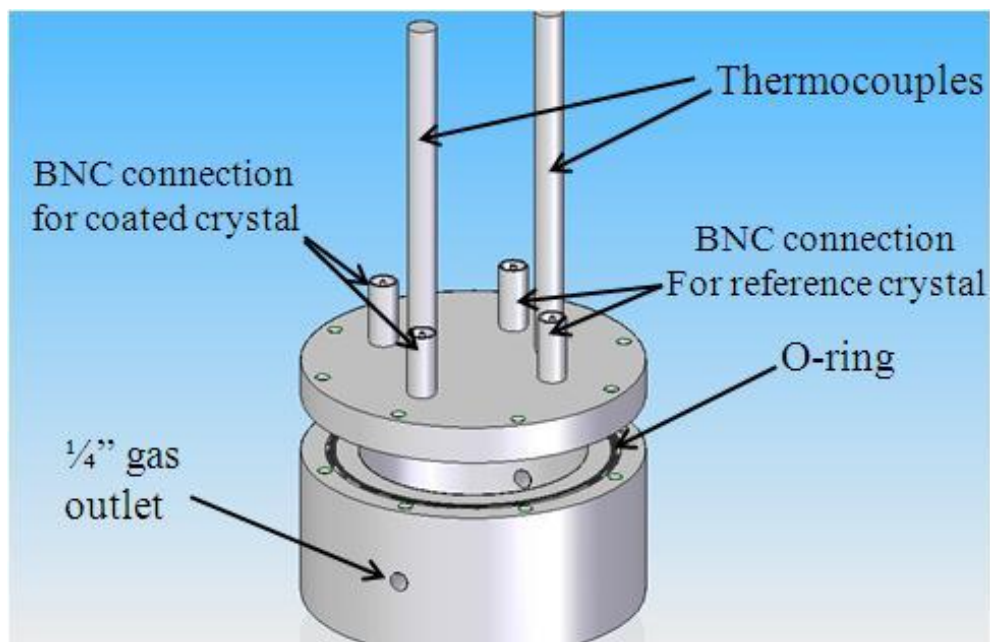


Figure 2.1. 3D rendering of the high pressure/ high temperature cell showing the 1/4" gas outlet connecting to the gas inlet/outlet system, Bayonet-Neill-Concelman (BNC) type connection to the phase lock oscillator (PLO) to measure the resonant frequency of the quartz crystal microbalance (QCM), thermocouples to measure the temperature inside the chamber and the high temperature O-ring to seal the chamber

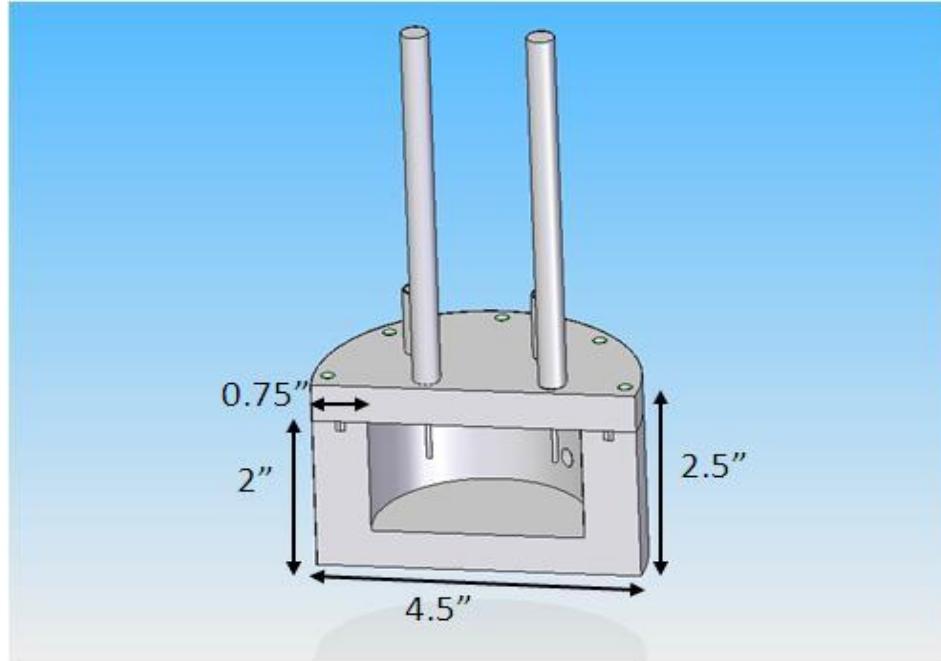


Figure 2.2. Cut-section view of the high pressure/ high temperature cell showing the dimensions of the chamber

2.2.2 Thermal Control System

Two K type thermocouples manufactured by Omega were screwed onto the cap of the cell in two different locations in order to monitor temperature gradients inside the cell. The measuring tips of the thermocouples are inside the cell as shown in Figure 2.1. The two thermocouples are connected to a cold junction compensator (OMEGA-CJ) through a metal shield wire. The voltage of the output was measured using two multimeters (Agilent 5313X Series), and the voltages were converted to temperatures using appropriate conversion expression in Labview©. Using two multimeters reduced the Lab View© program's cycle time and consequently improved the accuracy of the measurement. These multimeters were used as voltmeters and were accurate up to five

decimal digits in the voltage range 0 mV to 8 mV ensuring a temperature precision of 0.1°C. Detailed illustrations of the experimental setup are shown in Figure A.1 in Appendix A.

2.2.3 Analyte Gases

The sorption apparatus is currently capable of measuring gas uptake from CO₂, N₂, CH₄, Ethylene and n-Butane gases. However, the design could easily be modified for water vapor and volatile organic compounds (VOCs), if necessary. The gases used in all the experiments were ultra high purity gases supplied by Airgas (GA). A special protocol was maintained for gases like CH₄, n-Butane and Ethylene due to its inflammability. The inflammable gases need to be diluted with N₂ by a minimum ratio of 4:1 before venting the gas through the vacuum pump, to avoid ignition. The venting protocol for the inflammable gas is as follows: Following experiments at high pressure with inflammable gases, the high pressure cell is depressurized by venting into the fume hood up to 20 psi. The chamber is then pressurized with N₂ up to 80 psi. The chamber is then again depressurized by venting into the fume hood up to 20 psi. These steps are repeated several times (4-5) to ensure that the inflammable gas is diluted enough with N₂. Finally, the high pressure cell is pressurized with N₂ up to 50 psi, and the chamber is subjected to vacuum pump down. Detailed illustrations of the gas tanks in the experimental setup are shown in Figure A.1 in Appendix A.

2.2.4 Pressure Gauge

The pressure gauge used in our setup was MKS 121A Baratron® Capacitance Manometer which can operate at up to 150°C. The sensor and electronics are separated by an eight foot cable that allows the electronics to be mounted away from heat sources. The pressure gauge has a range of up to 10000 Torr and is an all metal sensor. The voltage output from the sensor is connected to a standard MKS pressure reader (PDR200) for measurement of pressure output. The pressure gauge is capable of handling corrosive gases compatible with inconel and stainless steel. Detailed illustration of the pressure gauge in the experimental setup is shown in Figure A.1 in Appendix A.

2.2.5 Phase Lock Oscillator

The resonant frequencies of the QCMs used in this setup were measured using Phase Lock Oscillators (PLO), purchased from Inficon, (NY, USA). The Phase Lock Oscillator was used to track the frequency of the QCM and the dc voltage that is proportional to the crystal's conductance which provides additional information in the study of lossy films and viscous solutions. The PLO utilizes an internal oscillator referred to as a Voltage Controlled Oscillator (VCO) to drive the crystal. The crystal current is monitored and the frequency of the oscillator is adjusted until there is zero phase error between the crystal voltage and current. Assuming the crystal's electrode capacitance has been effectively cancelled, this point of zero phase error between the crystal current and the voltage is the exact series resonant point of the crystal. The magnitude of current at this point is proportional to the crystal's conductance. This current is converted to a voltage, demodulated and amplified to create a dc voltage proportional to crystal

conductance. The PLO has a phase detector which continuously monitors the phase difference between the crystal's current and voltage; hence, the resonant frequency is automatically adjusted. This PLO, which supports 5 MHz crystals, was chosen for its electrode capacitance cancellation and auto lock features. Due to the high resolution required by the experiments; the phase lock oscillator is required to have a very small frequency error. From our experiments we have observed the phase lock oscillator to have a frequency error of 0.4 Hz for crystals with a quality factor of $\sim 120,000$, which is suitable for gas adsorption measurement. Detailed illustrations of the PLO in the experimental setup are shown in Figure A.1 in Appendix A.

2.2.6 Quartz Crystal Microbalance

The QCMs employed in this study were purchased from Inficon, NY. They had a resonant frequency of 5 MHz and were AT - cut at room temperature (25°C). The construction of the QCMs involved deposition of a thin layer of gold electrodes on either side of the quartz disc. The quartz disc was 1" in diameter and about 333 μm thick. The QCM is a thickness shear mode resonator in which acoustic waves propagate normal to the crystal surface [70]. The use of QCMs as chemical sensors has its origins in the work of Sauerbrey and King [70]. The shift in the resonant frequency of an oscillating AT - cut crystal is correlated quantitatively with addition or removal of mass from the surface of the device. AT - cut crystals are singularly rotated Y-axis cuts having thickness shear vibration mode (top and bottom half of the crystal move in opposite direction) during oscillation. The AT-cut quartz is chosen for its superior mechanical and piezoelectric properties, and the angle of cut can be adjusted to obtain a zero temperature coefficient at

a desired operating temperature. The Inficon AT cut for 25°C 1 inch diameter crystal was chosen because this crystal has very good temperature stability (minimal effect of temperature variation) for the range of temperatures (25°C – 65°C) we intend to operate in a gas environment. The advantages of QCMs over conventional gravimetric devices are: compactness, absence of buoyancy effects, and much higher sensitivity per unit sample mass [70]. The QCMs used in our experiments is shown in Figure 2.3. Detailed description of the theory of operation of the QCM is available in subsequent sections.

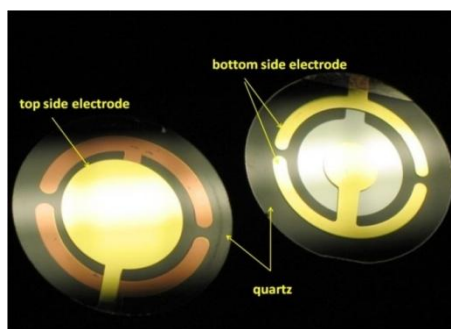


Figure 2.3 Illustrations of Quartz Crystal Microbalance (QCM) used in our experiments.

2.3 Description of the QCM based Sorption Apparatus

The schematic of the experimental setup is shown in Figure 2.4. Two identical crystals were placed inside the 175 cc high pressure stainless steel cylindrical chamber with a custom-designed QCM holder. One crystal was uncoated and acts as a reference sample, while the other was coated with the sample to be studied. The sample environment chamber was constructed from stainless steel SS 316 and can be operated up to a pressure of 10 bar and a temperature of up to 250 °C. The pressure limit is determined by the range of the pressure sensor, whereas the temperature limit is due to

the maximum operating temperature recommended for the O-ring (Markez® Z1213 perfluoroelastomer, size 236) used to seal the chamber at high pressure. The chamber was placed in a temperature control mantle and connected to an oil-free, dry scroll vacuum pump (Edwards XDS 10) by a 3' long, 1" outer diameter stainless steel tube. The O-rings and the chamber were cleaned periodically with a dry clean cloth and were blown with a jet of dry air to prevent any contaminants from settling in the chamber.

The two crystals were connected through four Bayonet-Neill-Concelman (BNC) connections *via* high-temperature-resistant cables to the two phase-lock oscillators (PLO-10, Inficon, NY). The output frequencies and dc voltages of both QCMs from the PLO-10 were measured by a frequency counter (Agilent 5313X Series) and an Acquisition/Switch unit (HP 34970A). Two K-type thermocouples were used to monitor the temperature at two different locations inside the chamber to ensure that any temperature gradients are negligible. In order to monitor the absolute pressure inside the cell, a pressure transducer (MKS 10000 Torr) was connected in the sample chamber, and the pressure was recorded by a pressure reader (PDR200). The pressure was controlled by dosing small amounts of gas into the cell to reach each new equilibrium pressure condition. The pressure sensors were periodically calibrated by MKS and were used as provided with an error of 0.01%. The temperatures, frequency changes due to the mass adsorbed and damping voltages were recorded with the LabView software. The sample chamber was placed inside two hemispherical heating mantles and further insulated using glass wool. A digital temperature controller (CG-15001, Chemglass, NJ) was used to control the temperature with a precision of $\pm 1^\circ\text{C}$. The gases used were research-grade and contain less than 5 ppm of water vapor. The current apparatus is equipped with a

heating mantle and but does not reach sub-ambient temperatures. It is, in principle, possible to conduct sub-ambient measurements with an appropriate cooling arrangement. Figure 2.5 presents a typical plot of the temperatures, resonant frequency of the QCM and the DC voltage of the QCM recorded with Lab View© software. It illustrates CO₂ gas adsorption in Cu-hfipbb MOF at 29 °C. Figure 2.5 A & B on the left are the frequency and the Voltage of the reference QCM. Similarly Figure 2.5 D & E on the right are the frequency and the voltage of the sample deposited QCM. Figure 2.5 C & F are the temperatures of the two thermocouples that were positioned inside the pressure vessel near the QCMs.

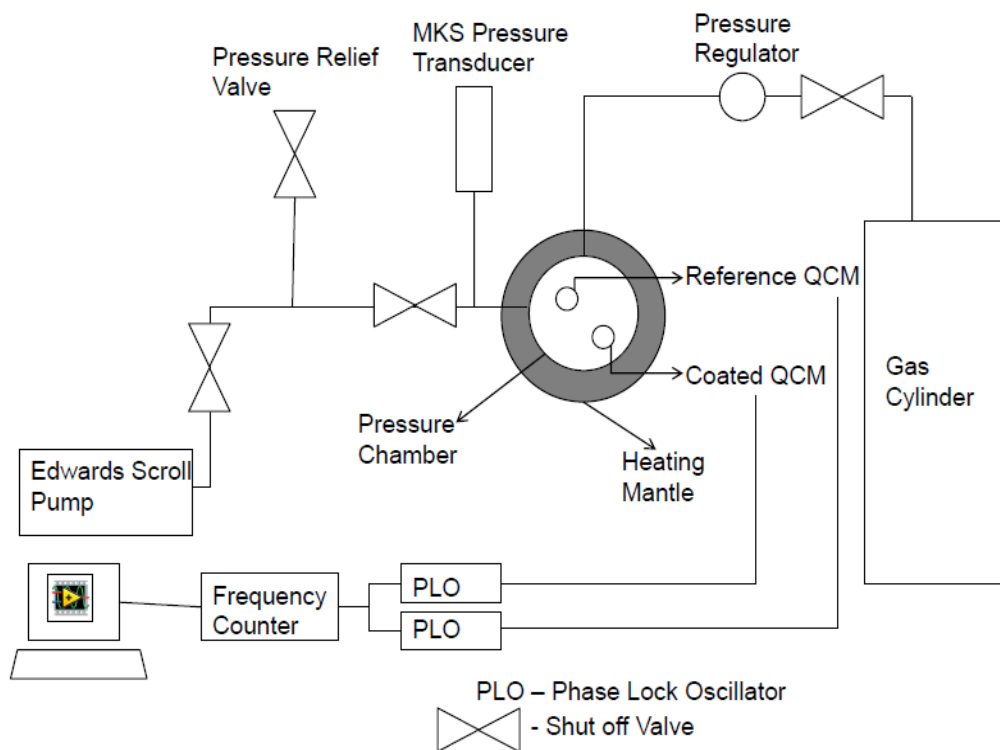


Figure 2.4 Schematic of the experimental setup [71]

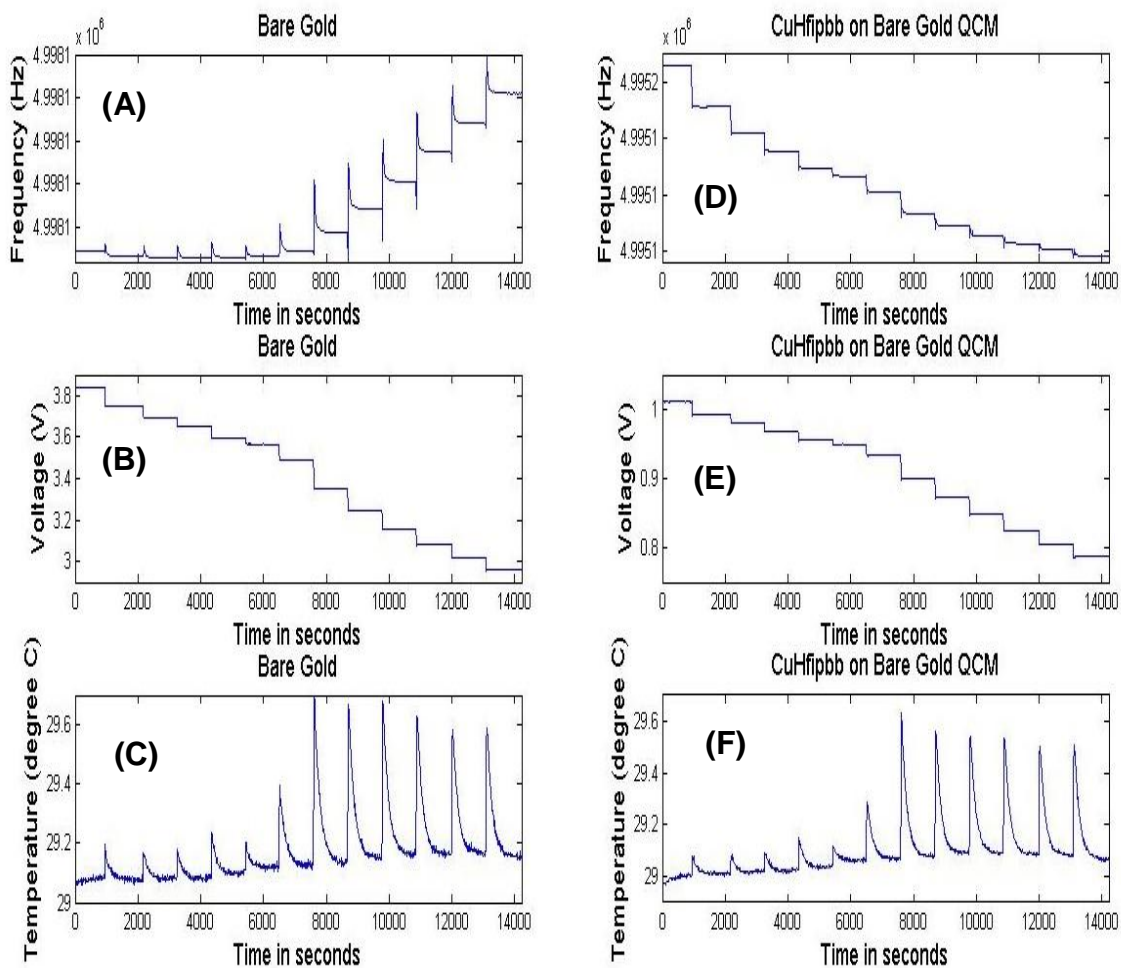


Figure 2.5 Labview© program recording the raw data for CO₂ gas adsorption in CuHfipbb MOF.

As shown in the Figure, the frequency of sample deposited QCM decreases as the pressure inside the cell increases, as a consequence of gas adsorbed into the adsorbent. On the other hand, the frequency of the reference QCM increases as the pressure inside the cell increases above 1 atm. However at pressures ≤ 1 atm, the frequency of bare QCM does not change appreciably. The dc voltages of both QCM were used to monitor the crystal resistance. As shown in Figure 2.5 C & F, the temperature gradient inside the cell

is relatively small ~ 0.2 °C and the equilibrium temperature changes are stable over a long period of time.

2.4 Theory of Measurement

2.4.1 Theory of Operation of the QCM

QCM is a shear acoustic-wave sensor in which the acoustic wave propagates in the direction perpendicular to the crystal surface. The principle behind this acoustic-wave sensor is that adding mass on the surface of the sensor causes the resonant frequency to decrease. Schematic of a 5 MHz Inficon 1” quartz crystal along with the crystal – electrode configuration and schematic of Inficon 1” quartz crystal as seen from the front side is shown in Figure 2.6 A & B. As shown in the Figure, QCM consists of three components: front side (sensing electrode), rear side (contact electrode) and the quartz dielectric. The front and rear side electrodes, whose planar dimensions are much larger than their thickness, are assumed to be thin films with infinite extensions. These two electrodes are connected to the electrical circuit for two main reasons: to obtain resonant frequency measurement and to stimulate shear deformation oscillation motion. The quartz plane which is an essential part of the QCM is bound between the two electrodes and is piezoelectric in nature. It is excited by applying AC voltage which induces a shear deformation oscillating at the frequency of excitation. This process is illustrated in Figure 2.7. Detailed explanation of the piezoelectric effect is given below.

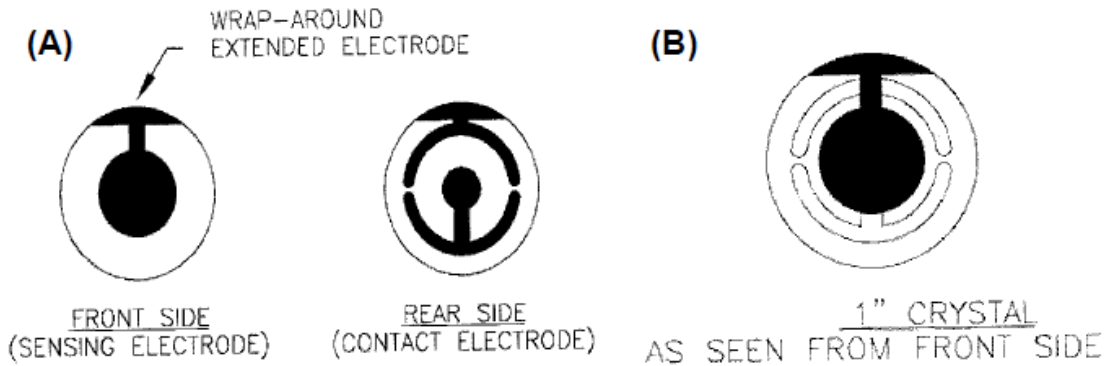


Figure 2.6 (A) Inficon 1'' Crystal – electrode configuration, (B) Inficon 1'' Crystal as seen from the front side [72]

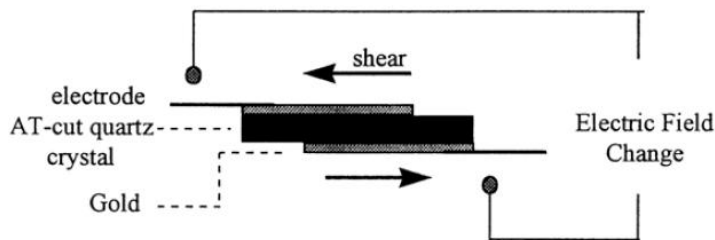


Figure 2.7 Schematic of the principle of operation of QCM

The piezoelectric effect is classified into two types: *direct piezoelectric effect* and *reverse piezoelectric effect*. In direct piezoelectric effect, the application of mechanical force induces the generation of an electric field, while the converse is true in the case of reverse piezoelectric effect. A detailed account of direct piezoelectric effect is presented here. In direct piezoelectric effect, electrical polarization of molecules occurs by subjecting the material to compressive stress (compressive mechanical force). Application of this compressive force on the material alters the location of negative and positive charges of the atoms in the crystal, hence causing the polarization of the

material. However there is no net charge inside the material, so the surface of the material becomes polarized. This polarized surface generates an electric field, resulting in the flow of electric charges in an external circuit in the direction of electric field. Upon the removal of mechanical force from the material, the polarization disappears, and the material comes back to its initial stage. By applying tensile stress on the material, the surface of the material becomes polarized again, however, the flow of electric charges is in the opposite direction of the flow of electric charges in the compressive force. This phenomenon as shown in Figure 2.8 A-C is called the direct piezoelectric effect in which an electric charge is generated by applying stress on the materials. Figure 2.8 shows that when pressure is applied to a material, the dipoles change / the polarization changes, and the electric field changes. When pressure is removed, the system reverts to its previous state of charge / polarization. The reverse piezoelectric effect occurs when a mechanical deformation is produced in a piezoelectric material when a voltage is applied between the electrodes of the piezoelectric material [73]. The reverse piezoelectric effect is the primary mechanism of operation for the QCMs.

The circuit model of QCM is shown in Figure 2.8 D. The electrical circuit consists of two branches: The motional branch and the static or shunt branch. The motional branch contains L.R.C circuitry that models the motion occurrence and is modified by mass and viscous loading of crystal. The static or shunt branch contains only the capacitance and it is associated with the dielectric materials between the two electrodes.

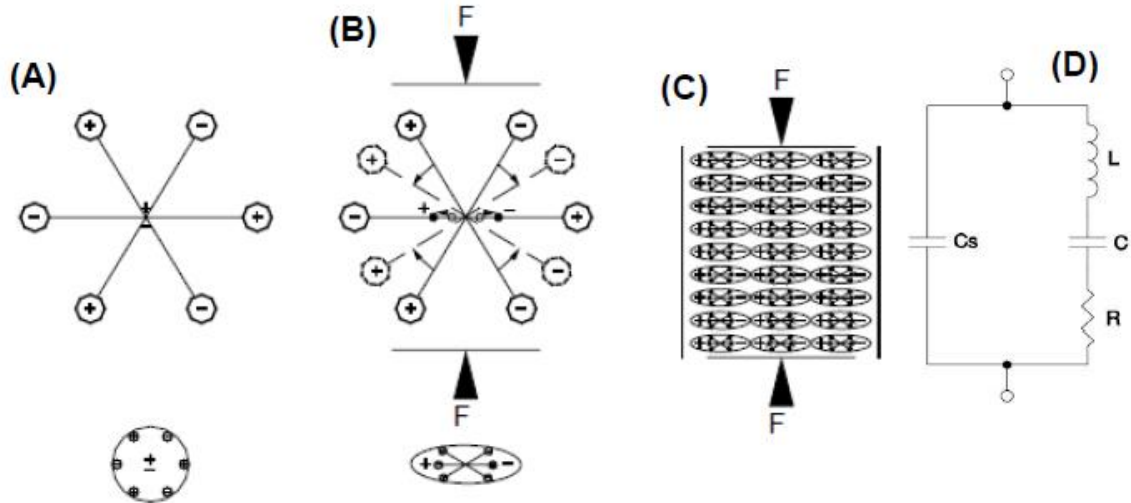


Figure 2.8 Simple molecular model for explaining piezoelectric effect: **(A)** unperturbed molecule; **(B)** molecule subjected to an external force; and **(C)** polarizing effect on material surface [73]; **(D)** electrical circuit model of the QCM

The resonant frequency of thick shear mode quartz is a transverse acoustic wave bouncing between the top and bottom electrodes. The resonant frequency of QCM is inversely proportional to the thickness of the crystal as shown in equation 2.1

$$f = n \frac{v_0}{2 \times L} \quad n=1,2,3,.. \quad (2.1)$$

where f is the resonant frequency, L is the thickness of the quartz plate; v_0 is the speed of sound within the crystal. One of the advantages of using quartz crystal resonators in sensing applications is associated with a specific crystal cut, at which the temperature coefficient of the crystal frequency is zero. At this point, the frequency change due to the temperature variation is minimized. Figure 2.9 shows the frequency change as a function of temperature for 25°C AT-cut crystal. For the room temperature AT-cut crystal, the effect of temperature in the range of 15°C to 45°C is negligible;

however, in a higher temperature environment, the effect of temperature can have a significant influence on attempts to detect small mass changes. The 25°C AT-cut QCM was chosen for our experiments because in most of our experiments the temperatures were in the range of 25°C to 70°C where the temperature coefficient was minimal.

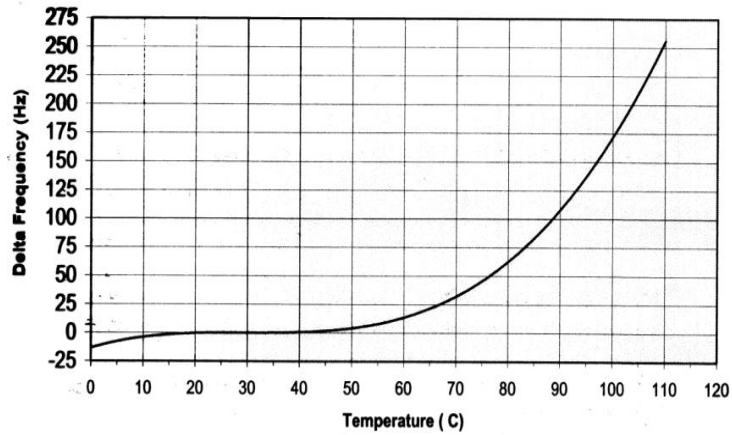


Figure 2.9 Frequency change versus temperature for the 5 MHz, 25°C AT- cut QCM

2.4.2 Sauerbrey's Equation

The use of QCMs as chemical sensors has its origins in the work of Sauerbrey and King [70]. The shift in the resonant frequency of an oscillating AT - cut crystal is correlated quantitatively with addition or removal of mass from the surface of the device. AT - cut crystals are singularly rotated Y-axis cuts having thickness shear vibration mode (top and bottom half of the crystal move in opposite direction) during oscillation. Mass changes are obtained from the Sauerbrey equation (equation 2.2)

$$\Delta m = \frac{(f_q - f) \sqrt{\rho_q \times \mu_q}}{2n \times f^2} \quad (2.2)$$

wherein Δm is the change in mass per unit area as a function of shift in resonant frequency (g/cm^2), f_q is the resonant frequency (Hz) of the reference state, f is the

resonant frequency of loaded crystal, ρ_q is the density of quartz (2.648 g cm^{-3}), μ_q is the effective piezoelectrically stiffened shear modulus of quartz ($2.947 \times 10^{11} \text{ g cm}^{-1} \text{ s}^{-2}$), and n is the resonant frequency mode (in this case, $n = 1$). It is assumed that the material deposited has the same acoustic-elastic properties as the substrate. This assumption holds for thin films and small amounts of powder/particulate samples, and is validated by comparing the resonant frequency of the unloaded crystal with the resonant frequency of the sample-loaded crystal. A common rule of thumb is that the shift in resonant frequency due to mass addition should be less than 1% for the Sauerbrey equation to be valid [74]. This was strictly maintained in all of our measurements.

2.4.3 Factors Affecting the Measurement of Resonant Frequency of QCM

The frequency change of a QCM is not only due to the mass adsorbed or deposited on the surface, but also due to various other factors as listed in equation 2.3 [70].

$$f = f_0 + \Delta f_m + \Delta f_T + \Delta f_P + \Delta f_v + \Delta f_R \quad (2.3)$$

Here f_0 is the fundamental resonant frequency, Δf_m is the shift in frequency due to mass change, Δf_T is the shift in frequency due to temperature changes, Δf_P is the shift in frequency due to pressure changes, Δf_v is the shift in frequency due to viscosity, and Δf_R is the shift in frequency due to “roughness loading” (i.e., shear caused by the ambient medium) [75].

The effect of temperature on frequency change is given by equation 2.4

$$\Delta f_T = f_0 \beta(T) \quad (2.4)$$

where $\beta(T)$ is the temperature coefficient and is negligible in the temperature range between 15°C to 45°C for 25°C AT- cut QCMs. The frequency change due to the hydrostatic pressure is given by equation 2.5.

$$\Delta f_p = f_0 \alpha P \quad (2.5)$$

where P is the hydrostatic pressure and α is the pressure constant. The pressure constant reported by Stockbridge is $1.045 \times 10^{-5} \text{ MPa}^{-1}$ at 25°C.

The effect of viscosity loading on QCM is discussed by Kanazawa using a physics model in the fluid [76] (equation 2.6)

$$\Delta f_v = -f_0^{\frac{3}{2}} \sqrt{\frac{\rho_L n_L}{\pi \rho \mu_L}} \quad (2.6)$$

where ρ_L is the density of the liquid, n_L is the viscosity of the liquid, ρ is the density of quartz. The frequency change due to the effect of viscosity loading is not significant for the gases and pressures used in our work. There are some variations in the value of the viscosity coefficient reported for liquid and gas surrounding [70, 77, 78].

In the end, effect of surface roughness loading is driven by equation 2.7 [79]

$$\Delta f_R = -H \times \rho_L \quad (2.7)$$

where H is a constant which depends on the surface roughness and fundamental frequency of the QCM. Since all our experiments were conducted under isothermal conditions and the bulk medium is a low-viscosity gas. Hence, the viscosity and roughness loading factors are negligible. Previous research has shown that gas adsorption in sorbent powders deposited on the QCM is negligibly affected by elasticity effects, and can be described with Sauerbrey's equation [80].

In order to eliminate the effects of frequency change due pressure and temperature, an identical reference QCM was placed in the experimental cell next to the coated QCM. The corrections were then applied to the frequency of the sample coated QCM by subtracting the response of the reference QCM from that of the sample-coated QCM. Using this technique, the frequency change due to the hydrostatic pressure and temperature were eliminated. The effect of roughness loading was assumed to be negligible, since the crystals used in the experiment have been polished on both sides.

Furthermore, the DC voltage of a QCM is another important factor which needs to be studied. The DC voltage is a proportional measure of the conductance (1/resistance) of the QCM crystal. The resistance of the crystal is important because it is directly proportional to the error due to imperfect capacitance cancellation. It is to be noted that in an earlier section (*Section 2.24, Phase Lock Oscillator*) it was mentioned that the assumption of the crystal's electrode capacitance to be effectively cancelled was pivotal in the measurement of resonant frequency by the Phase lock Oscillator (PLO-10). To ensure that the frequency error due to the crystal resistance is negligible for each measurement, equation 2.8 was used to convert the DC voltage of a QCM to a frequency error.

$$\Delta f = -\frac{\arctan(2\pi f_o C_{crystal} R_{crystal})}{2} \frac{f_o}{Q} \quad (2.8)$$

where f_o is the fundamental frequency ($f_o \sim 5MHz$), Q is the quality factor, $C_{crystal}$ is the capacitance of the crystal ($C_{crystal} = 6-7 pF$), and $R_{crystal}$ is the resistance of the crystal.

The quality factor is the sharpness of the resonant frequency peak and short term stability of an oscillation. It is defined as the ratio between the mechanical energy and the

energy dissipated per cycle due to the QCM oscillation. Hence, the quality factor is expressed by equation 2.9

$$Q = 2\pi \frac{\text{Mechanical energy}}{\text{Energy dissipated per cycle}} \quad (2.9)$$

The quality factor of typical Inficon 1” quartz crystal oscillator is around 120000. The resistance of the crystal was calculated using equation 2.10 and the DC voltage as shown below.

$$R_{crystal} = \frac{100}{V_{DC}} - 20 \quad (2.10)$$

Using these parameters in equation 2.8, the frequency error for the experiment is measured to be less than 1 Hz while dc voltage ranges between 3-3.6 V.

2.5 Conclusions

In this chapter the design considerations and the construction of the experimental setup was discussed. Detailed description of the theory of operation of the QCM along with the factors affecting the measurement of resonant frequency of QCM was presented. From the discussion, the assumptions held for thin films and small amounts of powder/particulate samples deposited on the QCM with respect to shift in resonant frequency due to mass addition were clearly illuminated. Further precautionary measures for the setup maintenance and experimental procedures with inflammable gases were also offered.

CHAPTER 3: APPLICATIONS TO GAS ADSORPTION IN POLYMERIC MATERIALS

3.1 Theory of Adsorption in Polymers

Most polyimides, like Matrimid 5218 and 6FDA-DAM, are glassy polymers at room temperature because they are below the glass transition temperature (T_g of Matrimid is 313°C [53] and that of 6FDA-DAM is 325°C [62]). As a consequence, polyimide films never reach thermodynamic equilibrium and the polymer chains are imperfectly packed. This generates excess free volume in the form of microscopic voids between polymer chains. Within these voids gases adsorb, increasing the solubility of gas within the polymer films. Therefore, the total concentration of absorbed gas within a glassy polymer film (C) can be described by (equation 3.1)

$$C = C_D + C_H \quad (3.1)$$

where C_H is sorption of gas within the microvoids, and can be approximated by the standard Langmuir adsorption relationship dependent on the gas pressure, p (equation 3.2):

$$C_H = \frac{C'_H \alpha p}{1 + \alpha p} \quad (3.2)$$

C'_H is the maximum adsorption capacity, while α is the ratio of rate coefficients of adsorption and desorption, or Langmuir affinity constant, defined as (equation 3.3)

$$\alpha = \frac{C_H}{(C'_H - C_H)p} \quad (3.3)$$

C_D is the concentration of gas dissociated within the polymer matrix and is proportional to the gas pressure through the Henry's Law constant (K_D) (equation 3.4):

$$C_D = K_D * P \quad (3.4)$$

Hence, the dual-mode sorption of gases with glassy polymer films is written as [53, 57, 58, 62] (equation 3.5):

$$C = K_D P + \frac{C'_H \alpha p}{1 + \alpha p} \quad (3.5)$$

The Henry's Law coefficient within this expression can be correlated with the Lennard-Jones potential well depth parameter (ε/κ) for the penetrating gas

$$K_D = K_{D0} e^{\frac{m\varepsilon}{\kappa T}} \quad (3.6)$$

The parameter, m , is a dimensionless constant signifying heat of adsorption due to Henry's mode. The parameter K_{D0} is a function of the medium through which the species penetrates. To further reduce the number of adjustable parameters, the maximum adsorption capacity C'_H and the Langmuir adsorption constant α can be assumed to follow an exponential relationship with temperature (equation 3.7 & 3.8 respectively)

$$C'_H = C'_{H0} e^{\frac{-\Delta H_s}{RT}} \quad (3.7)$$

$$\alpha = \alpha_0 e^{\frac{-\Delta H_s}{RT}} \quad (3.8)$$

where C'_H is the adsorbed gas concentration at STP (cc/cc), C_{H0} is the temperature-independent Langmuir adsorption capacity (cc/cc), ΔH_s is the Heat of adsorption (kJ/mol), α is the temperature dependent Langmuir adsorption constant (psi^{-1}), α_0 is the temperature-independent Langmuir adsorption constant (psi^{-1}) and P is pressure (in psi).

In order to fit the adsorption data from glassy polymers, this model includes a temperature-dependency relation to the Henry's part for both Matrimid and 6FDA-DAM. However for Langmuir part of the isotherm, for Matrimid, C_H has a temperature relation (equation 3.7) while α is maintained constant and for 6FDA-DAM, α has a temperature relation (equation 3.8) while C_H is maintained constant. The reasons for this fit will be explained later.

3.2 Materials of Interest

3.2.1 Matrimid 5218

Matrimid 5218 is a thermoplastic polyimide based on a diamine, 5(6)-amino-1-(4' aminophenyl)-1,3,-trimethylindane. It is fully imidized during manufacturing, eliminating the need for high temperature processing. For example, when solutions of Matrimid 5218 are used for coating applications, the substrate need only be heated to a temperature and for sufficient time to thoroughly remove the solvent thus forming pinhole-free coatings or void-free parts from those materials. Also, Matrimid 5218 is soluble in many organic solvents. The high solubility of these polymers is good from a processing standpoint. Further Matrimid 5218, is a polyimide widely used in industry because of its promising properties when separating gas mixtures and there have been few quantitative studies on the adsorption and permeation behavior of gases within these Matrimid films [53, 57-59]. From these studies it has been observed that Matrimid 5218 has high permeability and selectivity. Availability of data on adsorption and permeation behavior in Matrimid 5218 attracted our interest in studying this material as a membrane material. The chemical structure of Matrimid 5218 is shown in Figure 3.1.

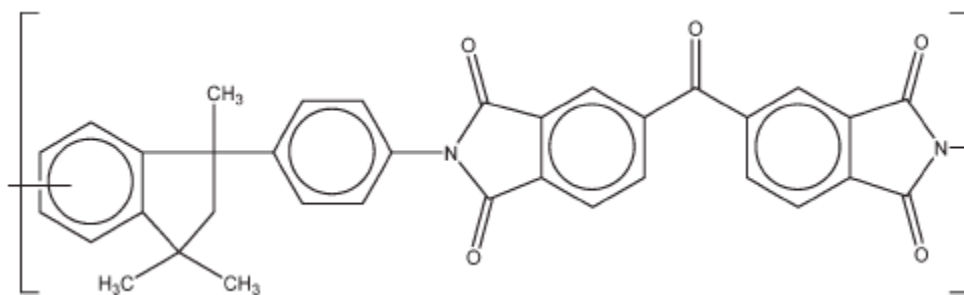


Figure 3.1 Structure of Matrimid 5218 polyimide [59]

3.2.2 6FDA-DAM

The 6FDA–DAM polyimide, is synthesized by polymerizing two monomers; 6FDA(2,2-bis (3,4-carboxyphenyl) hexafluoropropane dianhydride) and DAM (diaminomesitylene) [62]. Much research has been reported on polyimides derived from 4,4'- hexafluoroisopropylidene) dipthalic anhydride (6FDA), because they have excellent gas separation properties and are soluble in common solvents [81]. The high solubility of these polymers is good from a processing standpoint. Previous quantitative studies on sorption and permeation behavior of gases have shown that 6FDA-DAM films have high permeability and selectivity [5, 61-64, 69, 82]. However, none of these studies consider the effect of temperature or provide thermodynamic parameters of adsorption or permeation to understand its behavior as a membrane. Hence, the study of adsorption and permeation properties in this polyimide with respect to different temperatures and pressures may yield information on its thermodynamic properties and hence could open the route for fabricating high-quality nanoporous materials/polymer membranes. The chemical structure of 6FDA-DAM is shown in Figure 3.2

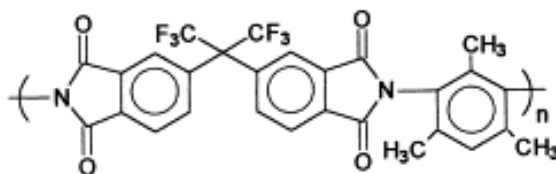


Figure 3.2 Structure of 6FDA-DAM polyimide [83]

3.3 Sample Preparation and Characterization of Matrimid 5218

3.3.1 Powder Type Deposition

To prepare the polymer sample, a 10% by wt suspension of Matrimid® 5218 (Hutzman, USA) was dissolved in N-methylpyrrolidone (99.5%, anhydrous, VWR scientific) and spin-coated on the QCM substrate at 2000 rpm. The sample was then pre-baked in a conventional oven at 120°C and atmospheric pressure for 30 min to remove bulk solvent. The sample was then mounted in the QCM sorption apparatus and degassed *in situ* at a temperature of 120°C under vacuum before adsorption measurements. Following the Matrimid deposition on the QCM, the samples were examined by Scanning Electron Microscopy (SEM). From the SEM images in Figure 3.3, we see that the Matrimid deposited on the QCM is distributed in islands and it does not form a continuous film. The mass of sample deposited was calculated to be 364 µg and was measured under vacuum after annealing and degassing.

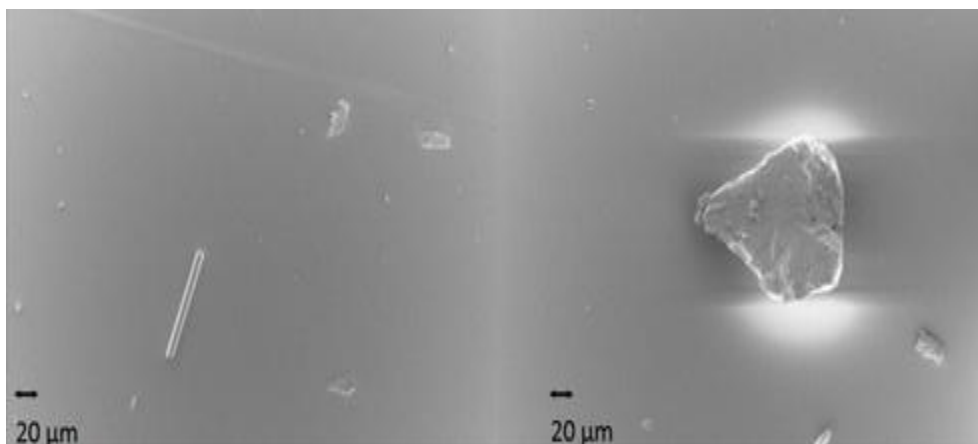


Figure 3.3 SEM images of Matrimid 5218 deposited on the QCM show island deposition

3.3.2 Thin Film Deposition

To prepare the polymer sample, a 20% by weight sample of Matrimid® 5218 (Hutzman, USA) was dissolved in N-methylpyrrolidone (99.5%, anhydrous, VWR scientific) and spin-coated on the QCM substrate at 3500 rpm. The sample was then pre-baked in a conventional oven at 100°C and atmospheric pressure for 30 min to remove bulk solvent. The sample was then mounted in the measurement apparatus and degassed *in situ* at a temperature of 100°C under vacuum before adsorption measurements for about 24 hours. The thickness of the film deposited was measured to be ~ 15-20 μm. The mass of sample deposited were calculated to be 3.16 mg and were measured under vacuum after annealing and degassing. Following the Matrimid deposition on the QCM, the samples was examined by Scanning Electron Microscopy (SEM). From the SEM images in Figure 3.4 A & B, we see that the Matrimid deposited on the QCM is a continuous film as evidenced by the sliver of gold at the edge of the Matrimid layer in Figure 3.4B.

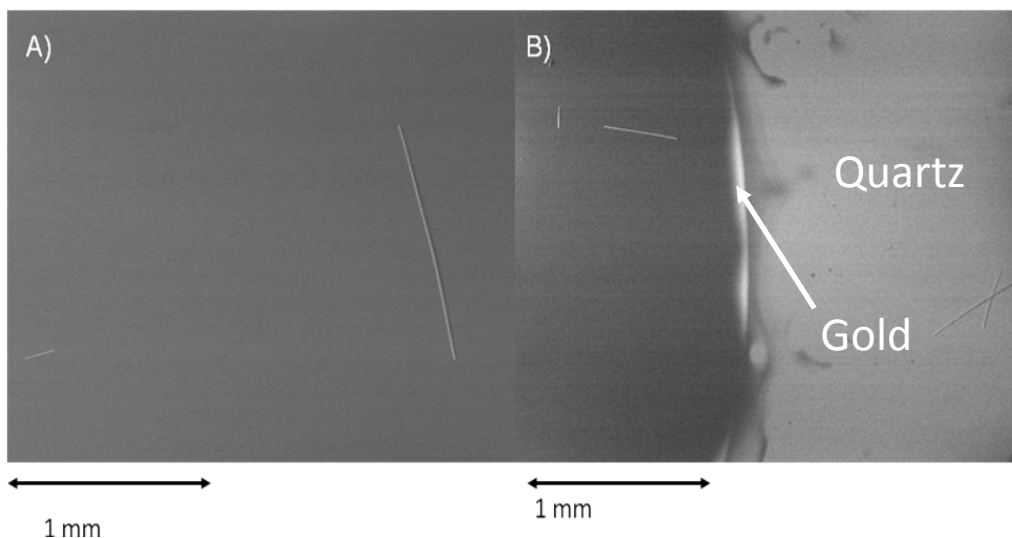


Figure 3.4 (A) SEM images of continuous thin films of Matrimid 5218 film deposited on the QCM; (B) edge of the film as evidenced by the sliver of gold

3.4 Gas Adsorption Measurement using Matrimid 5218

3.4.1 Powder Deposition

The ability of the QCM apparatus to measure adsorption was validated using a well-known polymer as a standard material. Hence we measured adsorption isotherms for CO₂ in the Matrimid® 5218 up to 60 psi of pressure and at temperatures between 25-53°C. Adsorption in Matrimid® 5218 was analyzed using the well-known dual mode adsorption isotherm for glassy polymers [53, 57, 58]. From Scholes et al. [53], $m = 6.67 \pm 0.5$. The Lennard-Jones potential well depth parameter (ϵ/κ) is obtained from Poling et al. [84] as 195.2 K for CO₂. In order to fit the adsorption data from glassy polymers, this model includes a temperature-dependent Henry's coefficient (K_D) and Langmuir adsorption capacity (C'_H), whereas the Langmuir parameter α is assumed to be temperature-independent as the variation across temperature was small.

Following the initial preheating at 120°C under vacuum, the chamber was cooled down to room temperature and the mass of Matrimid deposited was found by measuring the shift in resonant frequency. The deposited mass was measured to be 364 µg. Subsequently, single component CO₂ adsorption isotherms were collected at temperatures of 25°C, 42°C, and 52°C and pressures up to 60 psi. Figure 3.5 shows the experimental and fitted dual-mode adsorption isotherms for CO₂ in Matrimid (equations 3.5-3.7). The adsorption parameters obtained from our QCM-based measurement are compared against the adsorption parameters obtained gravimetrically by Scholes et al. [53] in Table 3.1. In Table 3.1, we observe a very good agreement between the thermodynamic parameters obtained from our experimental results and those obtained by Scholes et al. [53]. There are some minor quantitative differences, which are possibly due to differences in polymer film casting techniques, effects of physical aging of the polymer, and differences in penetrant gas purity [53, 57, 58]. The presence of such effects is not entirely avoidable. The average relative % error (ARE) between the model and the experimental data is shown in Table 3.2, corroborating the generally high quality of the fit results. Hence it is clear that our QCM-based apparatus gives reliable results and can be used reliably for microanalytical adsorption measurements.

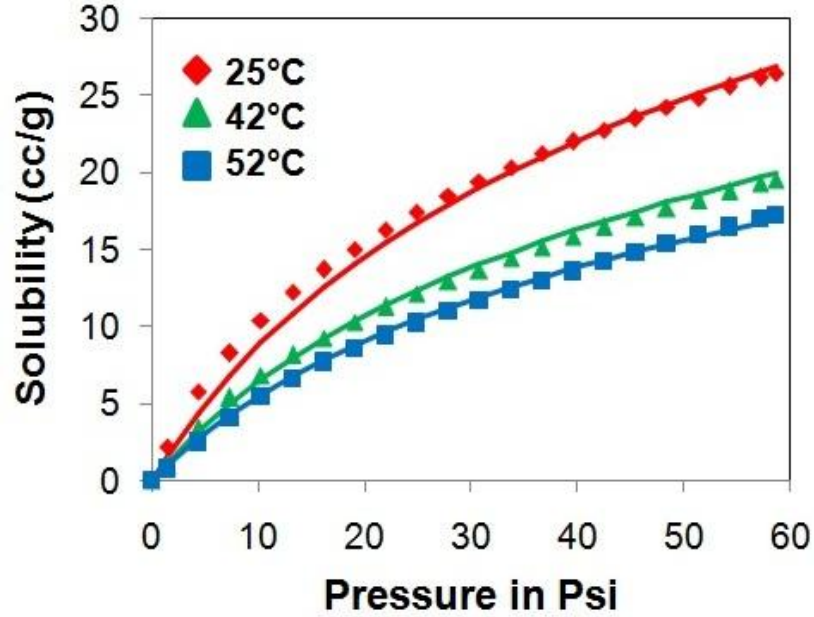


Figure 3.5 Solubility of CO₂ at STP per unit volume of Matrimid® 5218 at different temperatures as measured by the in-house developed Quartz Crystal Microbalance (QCM) sorption apparatus. The solid lines represent the dual mode isotherm model fit

Table 3.1 Comparison of thermodynamic adsorption parameters obtained from CO₂ adsorption in Matrimid 5218 using the QCM-based sorption apparatus with the corresponding parameters obtained from gravimetric measurements [53]

Parameter	QCM	Gravimetric [53]
C_{H0} (cc/cc)	0.09 ± 0.006	0.08 ± 0.031
ΔH_a (kJ/mol)	-14.6 ± 0.93	-14.9 ± 0.97
α (psi ⁻¹)	0.031 ± 0.002	0.034 ± 0.0023
K_{D0} (cc/cc.psi)×10 ⁻³	1.36 ± 0.09	1.23 ± 0.682
m	6.53 ± 0.4	6.67 ± 0.5

Table 3.2 Average relative error (%) between the experimental data and the dual mode adsorption model for CO₂ gas adsorption in Matrimid 5218[71].

CO ₂ Adsorption data @	Average Relative Error (ARE) (%)
25°C	6.4
42°C	3.2
52°C	3.3

$$*ARE(\%) = \frac{100}{N-1} \sum_{i=2}^N \left| \frac{Adsorption_{Experiment,i} - Adsorption_{Model,i}}{Adsorption_{Experiment,i}} \right|$$

3.4.2 Thin Film Deposition

The experimental procedure for gas adsorption in Matrimid 5218 thin film was similar to the procedure explained in section 3.4.1 for powder type deposition. The gas uptake isotherms were collected at temperatures between 30-45°C and up to pressures of 60 psi for both CO₂ and CH₄. The adsorption isotherms were then fit with Dual mode adsorption model (equations 3.5 - 3.7).

Using the Lennard-Jones potential well depth parameter (ϵ/κ) as obtained from Poling et al. [84] as 195.2 for CO₂ and 148.6 for CH₄, the corresponding thermodynamic adsorption parameters were obtained for CO₂ and CH₄. This experiment with Matrimid 5218 is also used to obtain diffusion coefficients and hence the permeation parameters.

In the paper by Zhao et al. [59], the permeation results for CO₂, CH₄, N₂ and H₂ at 2 atm and different temperatures were presented. From those results we observed, negligible difference between the permeation properties and selectivity with respect to CO₂ for both CH₄ and N₂, at all the temperatures presented. Hence in our experiments with the Matrimid thin films, we measured the adsorption and permeation properties for CO₂ and CH₄.

Following the initial preheating at 100°C under vacuum, the chamber was cooled down to room temperature and the mass of Matrimid deposited was found by measuring the shift in resonant frequency. Subsequently, single component CO₂ and CH₄ adsorption isotherms were collected at temperatures of 30°C, 35°C, and 45°C for pressures up to 60 psi. Figure 3.6 shows the experimental and fitted dual-mode adsorption isotherms for CO₂ and CH₄ in Matrimid 5218 (equations 3.5-3.7). The adsorption parameters obtained from the Matrimid film for CO₂ on our QCM-based setup are compared against the adsorption parameters obtained gravimetrically by Scholes et al. [53] and the separate powder deposition sample from our previous work [71] in Table 3.3. In Table 3.4, the adsorption parameters obtained from the Matrimid film for CH₄ on our QCM-based measurement are compared against the adsorption parameters obtained gravimetrically by Scholes et al. [53]. From Tables 3.3 and 3.4, we observe a reasonably satisfactory agreement between the thermodynamic parameters obtained from our experimental results and those obtained from the literature [53, 71]. However, there are some quantitative differences, particularly in the case of CO₂ adsorption in Matrimid 5218 thin film. While the exact reasons for these deviations are not known, possible reasons may be

due to differences in polymer material deposition techniques, initial annealing temperature, effects of physical aging of the polymer, and differences in penetrant gas purity [53, 71]. The presence of such effects is not entirely avoidable.

On comparing the experimental adsorption curves for CO₂ and CH₄, we observe that CO₂ adsorbs higher in quantity than CH₄ at comparable pressures. This is because the chemical associations between CO₂ and Matrimid are thermodynamically favorable and hence the adsorbed CO₂ concentration is higher than that for CH₄ at similar pressures. This is further corroborated by the higher heat of adsorption for CO₂ over CH₄. The standard dual-sorption behavior is that of a rapid increase in gas concentration at low pressures (dominated by Langmuir type Adsorption), which tapers off at higher pressures to an almost linear relationship (dominated by Henry's type adsorption). At low pressures, the microvoid space within the polymeric matrix is rapidly filled. As the pressure of the gas increases, free microvoid space becomes limited and the concentration increase is reduced to the sorption of gas in the polymeric matrix only. This follows Henry's law, hence the almost linear relationship at high pressures [53].

From Figure 3.6, it can be observed that the CO₂ adsorption shows the typical dual mode adsorption, while CH₄ shows weaker Langmuir type adsorption. This is evident in the decrease in Langmuir affinity constant (α) for CH₄ compared to CO₂. Further, the average relative % error (ARE) between the model and the experimental data is shown in Tables 3.5 and 3.6, corroborates the generally high quality of the fit results. Hence it is clear that our QCM-based apparatus gives consistent results and can be used reliably for microanalytical adsorption measurements from powder or film depositions.

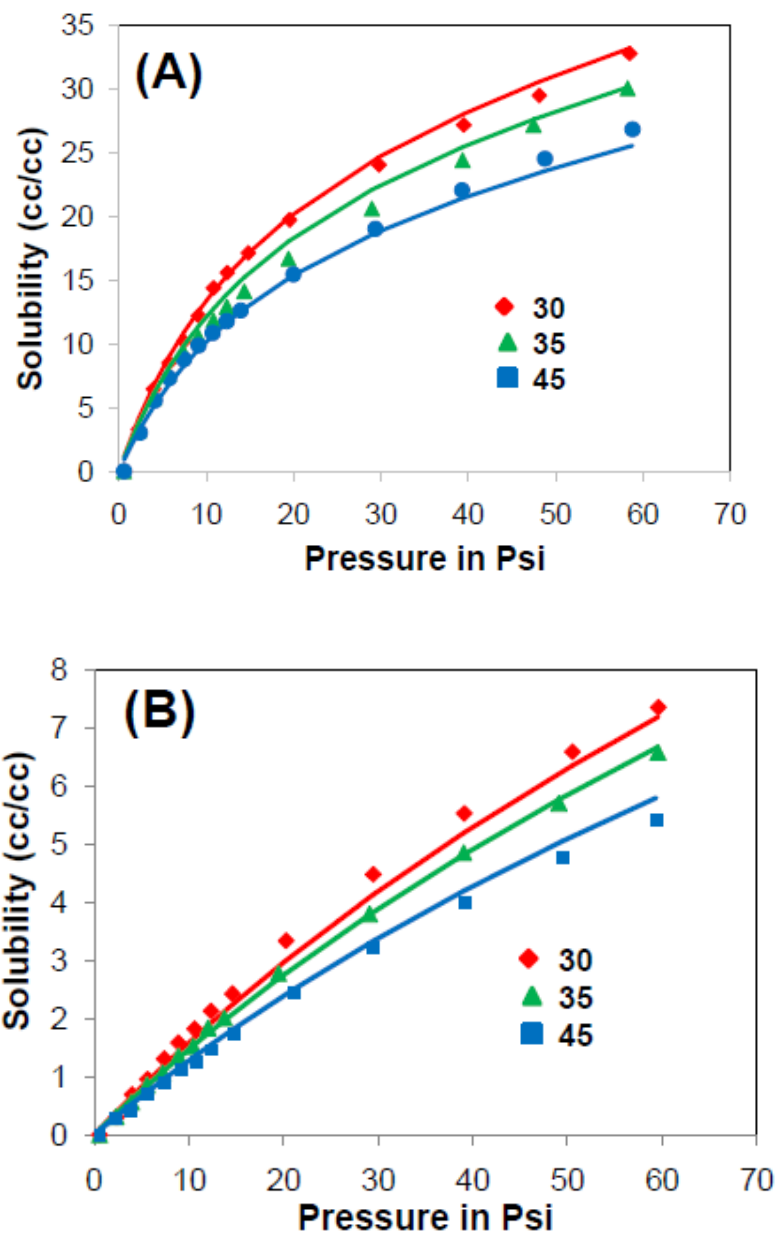


Figure 3.6 Solubility of gases at STP per unit volume of Matrimid® 5218 at different temperatures as measured by the QCM technique (A) Solubility of CO₂ at STP per unit volume of Matrimid® 5218 (B) Solubility of CH₄ at STP per unit volume of Matrimid® 5218. Solid lines represent the dual mode isotherm fit.

Table 3.3 CO₂ adsorption parameters for Matrimid 5218 obtained from the QCM-based measurement, and compared to parameters obtained from literature [53, 71].

Parameters	This work	Venkatasubramanian et al. 2012 [71]	Scholes et al. [53]
C _{H0} (cc/cc)	0.12 ± 0.008	0.09 ± 0.006	0.08± 0.031
ΔH _a (kJmol ⁻¹)	-14 ± 0.98	-14.6 ± 0.93	-14.9± 0.97
α (psi ⁻¹)	0.061 ± 0.0043	0.031 ± 0.002	0.034± 0.0023
K _{do} (cc/cc.psi) x10 ⁻³	2.2 ± 0.15	1.36 ± 0.09	1.23± 0.682
m	6.53 ± 0.46	6.53 ± 0.4	6.67± 0.5

Table 3.4 CH₄ adsorption parameters for Matrimid 5218 obtained from the QCM-based measurement, and compared to parameters obtained from literature.[53]

Parameters	This work	Scholes et al. [53]
C _{H0} (cc/cc)	0.196 ± 0.013	0.264 ± 0.081
ΔH _a (kJmol ⁻¹)	-10.8 ± 0.72	-11 ± 0.8
α (psi ⁻¹)x10 ⁻³	9.475 ± 0.632	7.77 ± 0.48
K _{do} (cc/cc.psi) x10 ⁻³	1.127 ± 0.0752	1.23± 0.682
m	6.9 ± 0.46	6.67± 0.5

Table 3.5 Average relative error (%) between the experimental data and the dual mode adsorption model for CO₂ gas adsorption in Matrimid 5218.

CO₂ Adsorption data @	Average Relative Error (ARE) (%)
30°C	4.6
35°C	6.9
45°C	3.7

Table 3.6 Average relative error (%) between the experimental data and the dual mode adsorption model for CH₄ gas adsorption in Matrimid 5218.

CH₄ Adsorption data @	Average Relative Error (ARE) (%)
30°C	8.7
35°C	3.4
45°C	8

3.5 Sample Preparation of 6FDA-DAM

3.5.1 Thin Film Deposition

To prepare the polymer sample, a 10% by weight sample of 6FDA-DAM (synthesized in-house as per the procedure in [62]) was dissolved in TetraHydrofuran (99.5%, anhydrous, VWR scientific) and spin-coated on the QCM substrate at 500 rpm. The sample was then air dried at room temperature and atmospheric pressure for 24 hours to evaporate bulk solvent. The sample was then mounted in the measurement apparatus and degassed *in situ* at a temperature of 210°C under vacuum before adsorption measurements for about 24 hours. The thickness of the film deposited was ~ 12 µm. The mass of sample deposited was calculated to be 2.05 mg and was measured under vacuum after annealing and degassing.

3.6 Gas Adsorption Measurement using 6FDA-DAM

3.6.1 Thin Film Deposition

Following the initial annealing and degassing at 210°C under vacuum, the chamber was cooled down to room temperature and the mass of 6FDA-DAM deposited was found by measuring the shift in resonant frequency. Subsequently, single component CO₂ and CH₄ adsorption isotherms were collected at temperatures of 30°C, 35°C, 45°C and 100°C for pressures up to 60 psi and are presented in Figures 3.7 A, B and C. Single component n-C₄H₁₀ adsorption isotherms were collected at temperatures of 45°C, 65°C and 100°C for pressures up to 20 psi and are presented in Figure 3.7 D. Figure 3.7A and D shows the experimental and fitted dual-mode adsorption isotherms for CO₂ and n-C₄H₁₀ in 6FDA-DAM (equations 3.5, 3.6 and 3.8, Table 3.7) while Figure 3.7B and C

show the experimental and fitted Henry's Isotherm for CH₄ (equation 3.6, Table 3.7). The Lennard-Jones potential well depth parameter (ϵ/κ) is obtained from Poling et al. [84] as 195.2 K for CO₂, 148.6 for CH₄ and 531.4 for n-C₄H₁₀. From the Figure, we observe that the quality of fit is satisfactory and the adsorption parameters obtained from the fits are reliable. The measure of the quality of the fit is given by average relative error (ARE %) and is presented in Table 3.8. Following dual mode fit at each temperature, it was observed that C_H did not vary much with temperature compared to α . Hence C_H was maintained constant.

From Figure 3.7A & D, we observe that CO₂ and n-C₄H₁₀ shows typical dual mode fit with low pressures (≤ 1 atm) dominated by pore filling mode (evident from larger change in slope) and higher pressures (> 1 atm) dominated by Henry's mode (evident from near linear relation to pressure). It is interesting to note that even though n-C₄H₁₀ is a larger sized molecule compared to CO₂, it fills the pores more effectively than CO₂, as evidenced by higher α_0 and K_{D0} compared to that of CO₂. However n-C₄H₁₀ has lower Langmuir adsorption capacity compared to CO₂ due to its larger molecular size. While the thermodynamic adsorption parameters like the heat of adsorption (ΔH_a and m) from both the modes (Henry's and Langmuir) is lower for n-C₄H₁₀ compared to CO₂, the overall equilibrium adsorption is higher for n-C₄H₁₀ compared to CO₂ at relevant pressures and temperature. This is primarily due to the relatively high α_0 and K_{D0} of n-C₄H₁₀ compared to that of CO₂.

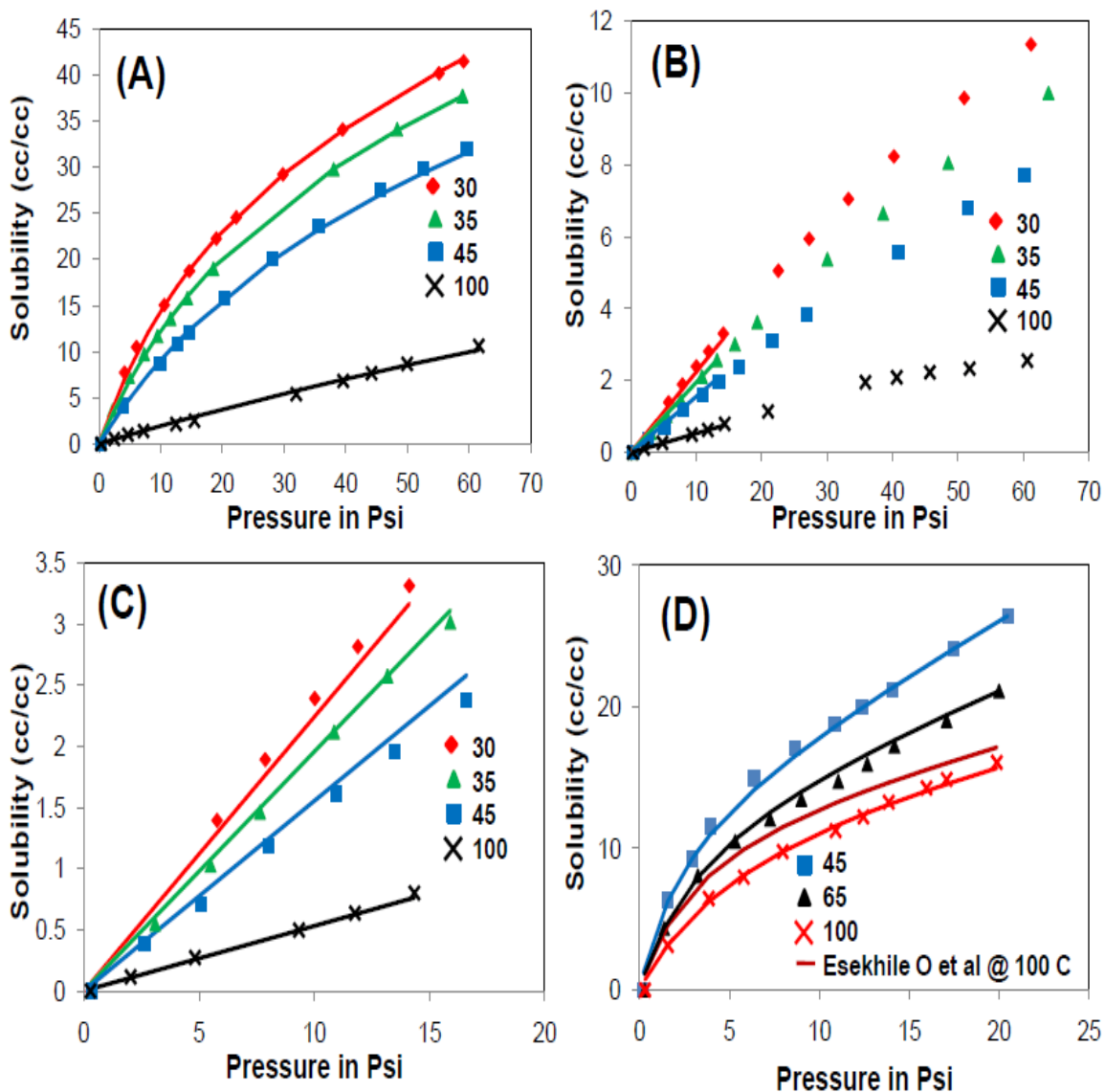


Figure 3.7 Solubility of gases at STP per unit volume of 6FDA-DAM at different temperatures as measured by the QCM technique. **(A)** Solubility of CO₂ at STP, **(B)** Solubility of CH₄ at STP, **(C)** Solubility of CH₄ at STP represented up to 1 atm and **(D)** Solubility of n-C₄H₁₀ at STP. Solid lines represent the Dual Mode isotherm fit for **(A)** CO₂ and **(D)** n-C₄H₁₀ and Henry's Fit for **(C)** CH₄.

From Figure 3.7B & C, we observe that, compared to CO₂ and n-C₄H₁₀, the adsorption isotherm for CH₄ is dominated by Henry's mode (evidenced by near linear relation to pressure). However at higher pressures (> 1 atm), there is a possibility of adsorbate-adsorbate interactions. Hence the isotherms were fit with Henry's model at sub atmospheric pressure range where linearity is perfectly maintained. From the parameters obtained we can understand that adsorption of CH₄ was clearly dominated by Henry's mode as evident from the Henry's constant and the quality of fit (Refer to Table 3.8).

Table 3.7 Gas adsorption parameters for 6FDA-DAM obtained from the QCM-based measurement

Parameters	CO ₂	CH ₄	n-C ₄ H ₁₀
C _H (cc/cc)	40 ± 2.17	-	13.6 ± 0.3
ΔH _a (kJmol ⁻¹)	-30.7 ± 1.7	-	-16.1 ± 0.35
α ₀ (psi ⁻¹)	(2.2 ± 0.12) x 10 ⁻⁷	-	(9 ± 0.2) x 10 ⁻⁴
K _{do} (cc/cc.psi) x10 ⁻⁴	0.12 ± 0.00651	1.323 ± 0.06	9 ± 0.2
m	15.2 ± 0.8	15.1 ± 0.7	4 ± 0.09

Table 3.8 Average relative error (%) between the experimental data and the adsorption model for gas adsorption in 6FDA-DAM

Average Relative Error (ARE %) @	CO ₂	CH ₄	n- C ₄ H ₁₀
30	6	5	-
35	2.5	3.4	-
45	7.5	7.4	2
65	-	-	2.9
102	5.7	3.5	1.7

3.6 Conclusions

In this chapter the gas adsorption characteristics in polymer materials, particularly, the gas adsorption measurements from Matrimid 5218 and 6FDA DAM are presented. Following the construction of the setup, which has been described in chapter 2, the adsorption measurement capability was validated using Matrimid 5218 deposited in powder form. From the measurements, the thermodynamic adsorption parameters for CO₂ were obtained and were found to compare well with the literature. Further experiments with polymer materials (Matrimid 5218 and 6FDA-DAM) deposited as thin films were conducted to obtain the adsorption parameters for specific analytes. From these polymeric thin films, the gas adsorption isotherms (CO₂ & CH₄ for Matrimid 5218 and CO₂, CH₄ & n-Butane for 6FDA-DAM) were collected and studied using the dual mode adsorption model. From our analysis on the gas adsorption data from Matrimid

5218 we found that it agreed well with the literature and that the adsorption favorability for $\text{CO}_2 > \text{CH}_4$. For 6FDA-DAM, there is no known literature for comparison. Based on our analysis, we found that the CO_2 and $\text{n-C}_4\text{H}_{10}$ adsorption followed the dual mode adsorption model while CH_4 followed the Henry's mode of adsorption. In the case of 6FDA-DAM, the adsorption favorability followed the order $\text{n-C}_4\text{H}_{10} > \text{CO}_2 > \text{CH}_4$. Thus the gas adsorption setup developed is capable of providing reliable measure of the thermodynamic adsorption parameters of samples deposited both in powder and thin film form.

CHAPTER 4: APPLICATIONS TO GAS ADSORPTION IN NANOPOROUS MATERIALS

4.1 Theory of Adsorption in Nanoporous Materials

As mentioned in Chapter 1 (section 1.1), nanoporous materials are broadly classified into three subdivisions based on their pore diameter *viz.* microporous (0.2 – 2 nm), mesoporous (2-50 nm) and macroporous (50 – 1000 nm) materials. In this thesis, we deal only with microporous materials to exploit the size selective property in gas separation applications.

Adsorption processes in microporous materials are very complex at the molecular level. However, in order to get a fundamental understanding of the adsorption process, well known analytical models like the Langmuir adsorption model can be applied to the experimental gas adsorption isotherms [66, 71, 85, 86]. Using empirical relations like exponential relation to temperature with respect to adsorption constant in conjunction with these analytical models, thermodynamic parameters of adsorption like heat of adsorption and adsorption capacity can be derived. Such parameters help in understanding the adsorption behavior and provide useful information for subsequent computational modeling and membrane fabrication efforts.

4.1.1 Langmuir Adsorption Model

The Langmuir adsorption model is the most common model used to quantify the amount of adsorbate adsorbed on an adsorbent as a function of pressure or concentration

at a given temperature. It considers adsorption of an ideal gas onto an idealized surface. The gas is presumed to bind at a series of distinct sites on the surface of the solid.

Inherent within this model, the following assumptions are valid specifically for the simplest case: the adsorption of a single adsorbate onto a series of equivalent sites on the surface of the solid [87].

1. The surface containing the adsorbing sites is homogeneous
2. The adsorbing gas adsorbs into an immobile state.
3. All sites are equivalent.
4. Each site can hold at most one molecule of an adsorbate (mono-layer coverage only).
5. There are no interactions between adsorbate molecules on adjacent sites.

Based on the above assumptions and using simple equilibrium equation between open surface sites and adsorbate filled sites, the Langmuir equation is derived to be

$$C = \frac{C_H \times \alpha P}{1 + \alpha P} \quad (4.1)$$

where C_H is a temperature-independent Langmuir adsorption capacity (cc/g), α is the temperature-dependent Langmuir constant (psi^{-1}) and P is the pressure. However, the Langmuir equation as derived in equation 4.1 provides adsorption parameters at a particular temperature. In order to obtain thermodynamic parameters like heat of adsorption (ΔH_a), α in equation 4.1 can be used with exponential relation with respect to temperature expressed as

$$\alpha = \alpha_0 \times e^{\left(\frac{-\Delta H_a}{RT}\right)} \quad (4.2)$$

where α is the temperature-dependent Langmuir constant (psi^{-1}), α_0 is the temperature-independent Langmuir constant (psi^{-1}), ΔH_a is the heat of adsorption (kJmol^{-1}), R is the Universal Gas Constant (8.314 kJmol^{-1}) and T is the Temperature. Using equation 4.1 and 4.2, we derive the adsorption parameters; heat of adsorption (ΔH_a , kJmol^{-1}), adsorption capacity (C_H , cc/g) and temperature-independent Langmuir constant (α_0 , psi^{-1}) for each analyte in the nanoporous materials. Based on our experiments, we observed that α varied more relatively than C_H across different temperatures, hence we chose to keep C_H constant across different temperatures.

4.1.2 Henry's Law

Another model that has been applied to study the adsorption properties in microporous materials in this thesis is the Henry's Model. As per Henry's Model, at a given constant temperature, the amount of gas adsorbed on a material is directly proportional to the partial pressure of that gas. It is expressed in equation 4.3 as

$$C = K_H P \quad (4.3)$$

where C is the volume of gas adsorbed per unit mass of the adsorbent (cc/g), P is the pressure and K_H is the Henry's constant of adsorption (cc/g.psi). An important assumption for Henry's Law to be applied is that the adsorbate does not chemically react with the adsorbent, which is the case here.

4.2 Materials of Interest

4.2.1 Copper-Based MOF (*Cu-hfipbb*)

A copper – based metal–organic framework, $\text{Cu}(\text{hfipbb})(\text{H}_2\text{hfipbb})_{0.5}[\text{H}_2\text{hfipbb} = 4,4'-(\text{hexafluoro-isopropylidene})\text{bis}(\text{benzoic acid})]$ (referred to as *Cu-hfipbb*), was selected as an adsorbent because it has small cages of ($\sim 5.1 \times 5.1 \text{ \AA}$) that are accessible through smaller apertures of ($\sim 3.5 \times 3.5 \text{ \AA}$) [85]. The aperture size is comparable with kinetic diameters of CO_2 (3.3 \AA), CH_4 (3.8 \AA), N_2 (3.6 \AA), ethylene (3.9 \AA) and n-Butane (4.3 \AA) [88]. This suggests the possibility of kinetic separation by exploiting the diffusion rate difference through the micro-channels of *Cu-hfipbb*. Recently, Watanabe et al. [19] predicted using computational methods that this MOF has a selectivity of 10^4 – 10^5 for a membrane-based separation of CO_2/CH_4 mixtures [19]. The main contribution to this very large selectivity comes from the difference in CO_2 and CH_4 diffusivities. This theoretical prediction of an extremely high kinetic selectivity of CO_2/CH_4 inspired this research work. Figure 4.1 illustrates the crystal structure of this *Cu-hfipbb* MOF, which is constructed upon copper paddle-wheel and a V-shaped dicarboxylate linker. The arising 3D structure has only 1D cage-like channels oriented along the length of columnar crystals. These structures contain fluorine and they are hydrophobic, thus they can be used even in the presence of moisture.

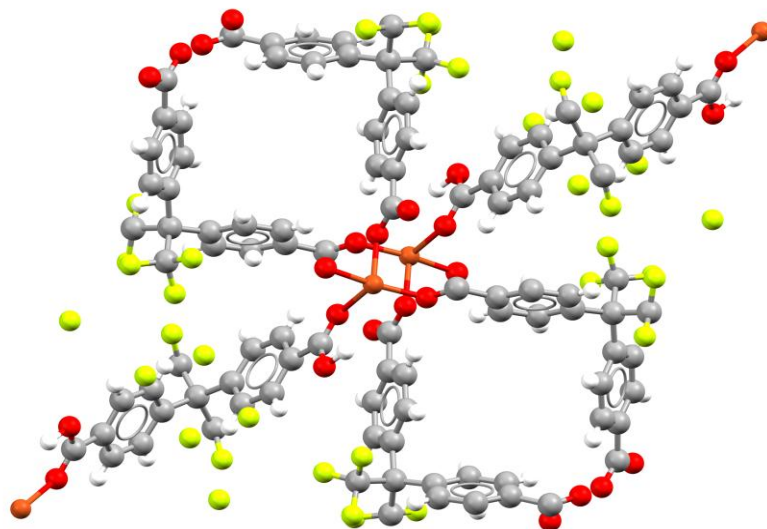


Figure 4.1 Structure of the Cu-hfipbb MOF [71]

4.2.2 Zeolitic Imidazolate Framework – 90 (ZIF-90)

A zinc-based metal – organic framework, Zeolitic Imidazolate Framework - 90 (referred to as ZIF-90), was selected as an adsorbent because it has large cages of (~11 Å diameter) that are accessible through small apertures of (~3.5 Å diameter). The aperture size is larger than the kinetic diameters of CO₂ (3.3 Å) but smaller than that of CH₄ (3.8 Å) and N₂ (3.6 Å) [88]. Although previous investigations have fabricated and tested membranes containing ZIF-90 [21, 89-91], very little was known about the intrinsic adsorption and transport properties of this material. This inspired this research work. Figure 4.2 illustrates the crystal structure of ZIF-90, which is found to be related to the sodalite topology by replacing the Si and O with Zn and ICA links, respectively [21]. This leads to an expanded ZIF structure with large voids and an extended 3-D ZIF structure with an aperture of 3.5 Å in diameter and a pore size of 11.2 Å. These structures are hydrophobic, thus they can be used even in the presence of moisture.

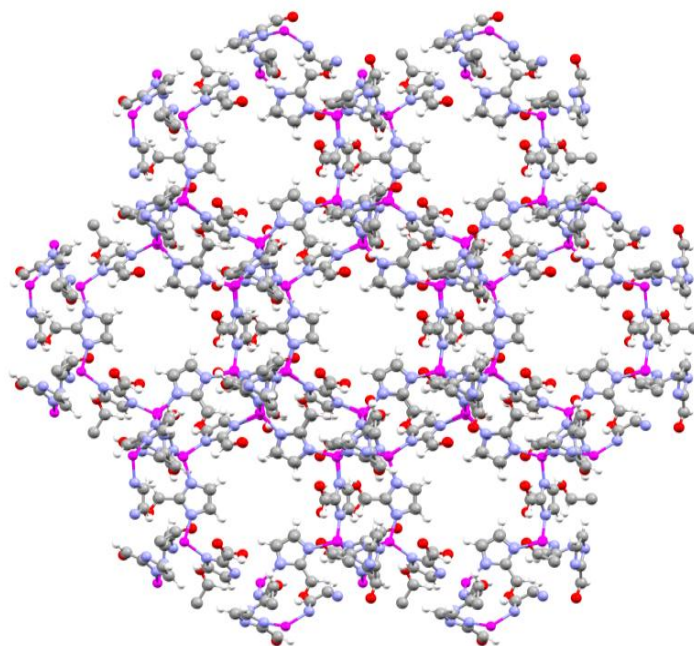


Figure 4.2 Structure of ZIF-90[71]

4.2.3 Aluminosilicate Nanotubes and its Modifications (AlSiNTs)

This type of nanotube consists of an octahedral aluminum (III) hydroxide outer wall and a tetrahedral silanol inner wall, with doubly-coordinated hydroxyl groups on the outer wall and pendant hydroxyls on the inner wall. The aluminosilicate nanotubes (AlSiNTs) in this form are known as the Bare NTs (Figure 4.3A). However the selectivity of these bare NTs is poor. In order to improve the selectivity, the bare NTs were functionalized by partially replacing the hydroxyl group (-OH) with alkyl amine group (-CH₂NH₂). Prior to functionalization with methyl amine, the first successful example of direct synthesis of organic-substituted aluminosilicate SWNTs involved the use of methyltriethoxysilane (MTES) for producing methyl-functionalized aluminosilicate nanotubes [92]. However, the methyl group only confers limited functionality, imparting

only hydrophobicity. Similar efforts using other commercially available organosiloxane precursors (e.g., aminopropyltriethoxysilane, APTES) have been unsuccessful [93].

Hence the single-walled AlSiNTs were functionalized with methyl amine groups (ANTs) with up to 15% of the interior $\equiv\text{Si-OH}$ groups substituted by $\equiv\text{Si-CH}_2\text{NH}_2$ groups, *via* the use of an in-house-synthesized precursor (aminomethyltriethoxysilane, AMTES). The structure, morphology and surface chemistry of ANTs are investigated by a range of solid-state characterization techniques, including conventional and cryogenic transmission electron microscopy (TEM/cryo-TEM), X-ray diffraction (XRD), nitrogen physisorption, elemental analysis, vibrational spectroscopy, and solid-state NMR [93]. The functionality of the primary amine groups in the interior of the SWNTs is assessed by CO_2 , CH_4 , and N_2 adsorption. The amine-functionalized nanotubes (ANTs) show a dramatic improvement in CO_2/CH_4 and CO_2/N_2 adsorptive selectivity over the bare nanotubes (BNTs). The synthesis of amine-functionalized metal oxide SWNTs can now facilitate a new class of functional SWNT materials obtainable by further chemical modifications of the amine groups. Figure 4.3 B shows the structure of the methyl amine functionalized aluminosilicate nanotubes.

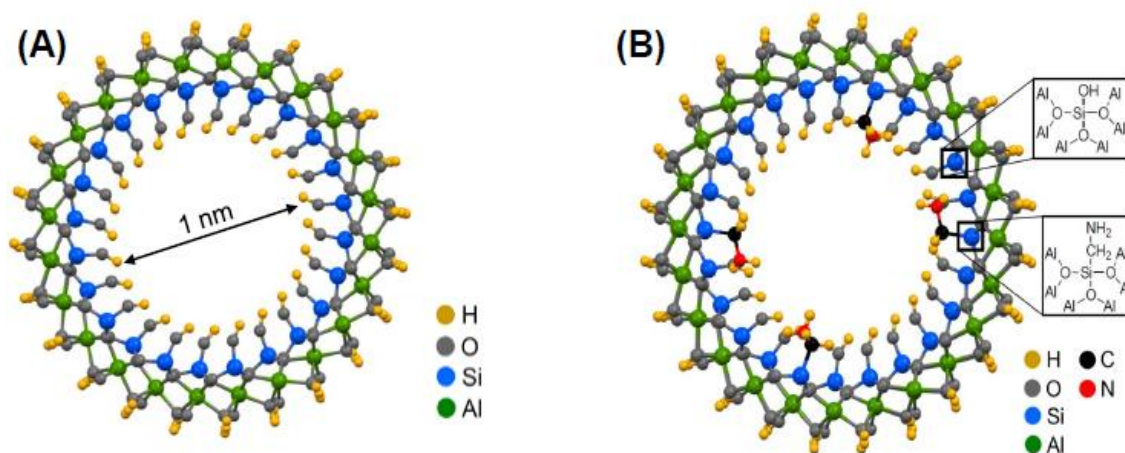


Figure 4.3 Structure of the (A) Bare aluminosilicate nanotubes (BNTs), (B) 15 % methylamine functionalized aluminosilicate nanotubes (ANTs)

4.3 Sample Preparation and Characterization of Metal Organic Frameworks (MOF)

4.3.1 Synthesis, Deposition and Characterization of Cu-hfipbb MOF (small crystals)

4.3.1.1 Synthesis of Cu-hfipbb MOF Crystal (small crystals)

Cu-hfipbb crystals were synthesized by the procedure of Carson et al. [61]. To synthesize Cu-hfipbb, 4,4'-(hexafluoroisopropylidene) bis (benzoic acid) (98%), copper(II) nitrate hemi(pentahydrate) (98%), and 2-propanol (99.5%) were used as purchased from SigmaAldrich. A 200 mg quantity of H₂hfipbb was dispersed in 75 mL of deionized water by shaking and sonication. In a separate container, 79 mg of copper (II) nitrate hemi (pentahydrate) was dissolved in 5 mL of water and 1 ml of isopropanol. The molar ratio of copper nitrate to H₂hfipbb to water was 1:1.5:12900. The two solutions were then mixed and placed in an ice bath and sonicated for 6.6 hours with a Sonics Vibracell VCX 130 sonication horn at 77 W, whereupon crystals of Cu-hfipbb

precipitated from the solution and were recovered by centrifugation and washing with water.

4.3.1.2 Deposition of Cu-hfipbb MOF Crystals on QCM Substrates (small crystals)

A 3 g/L suspension of MOF crystals was formed in isopropanol, and sonicated for 60 min. Cu-hfipbb crystals were deposited on the QCM substrate by spin-coating from the suspension at 150 rpm. A 50 μ l volume of the suspension was added at a time, and allowed to evaporate. After an interval of 0.5-1 minute, another 50 μ l aliquot was added. A total of 500 μ l volume was deposited in this manner. The substrates were then pre-baked in an oven at 195°C and atmospheric pressure for 30 min. In this manner, two samples were prepared. The samples were then mounted in the measurement apparatus and degassed *in situ* at a temperature of 185°C under vacuum for about 12 hours before adsorption measurements [71]. Following the initial degassing at 185°C under vacuum, the chamber was cooled down to room temperature and the mass of Cu-hfipbb MOF deposited was measured to be 404.7 μ g (sample 1) and 262.4 μ g (sample 2).

4.3.1.3 Characterization of Cu-hfipbb MOF Material

Following the Cu-hfipbb MOF material deposition on the QCM, the samples were examined by Scanning Electron Microscopy (SEM), and by Powder X-ray Diffraction (XRD) before and after the adsorption measurements to ensure that the structure of the MOF was preserved throughout the experiment. From the SEM images in Figure 4.4, it is apparent that the Cu-hfipbb crystals have a size distribution ranging from 0.5-2 μ m and the distribution of the sample on the QCM is not uniform as we can see patches on the

gold substrate. The PXRD patterns of the deposited Cu-hfipbb MOF samples obtained before and after the adsorption measurement, were generally consistent with the simulated PXRD patterns of highly crystalline Cu-hfipbb (see Figure 4.5). However in Figure 4.5, there is a slight shift in peak intensity between experiments. Many MOFs show minor structural changes (as seen by XRD) after activation and sorption measurements. The sources of these changes are not yet clearly understood. Two possible reasons are the loss of residual solvent molecules during activation, or slight disorder induced by heating.

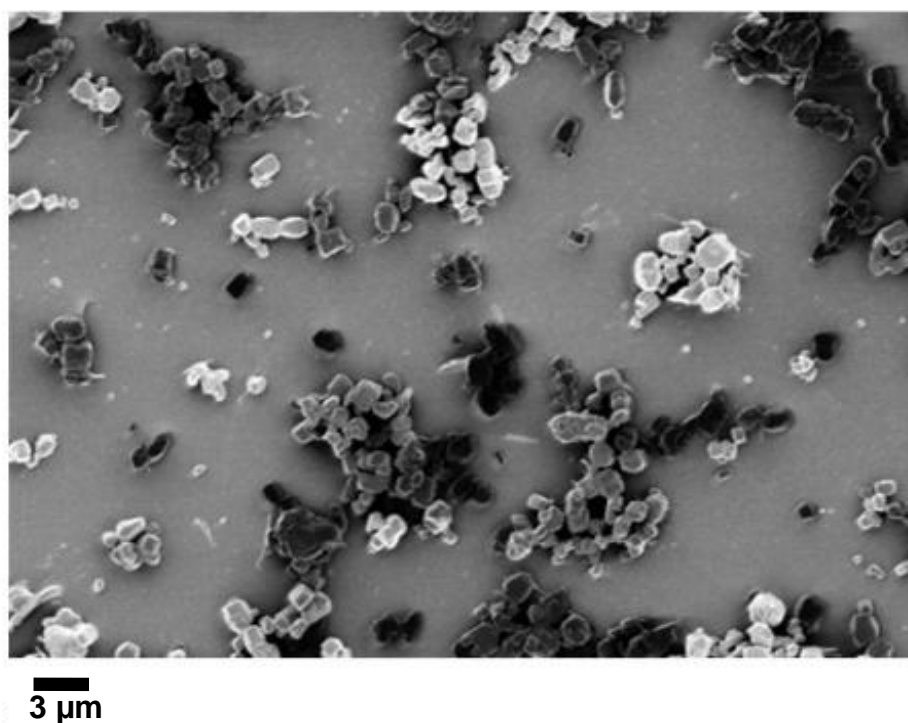


Figure 4.4 Cu-hfipbb crystals deposited on the gold surface of the QCM.

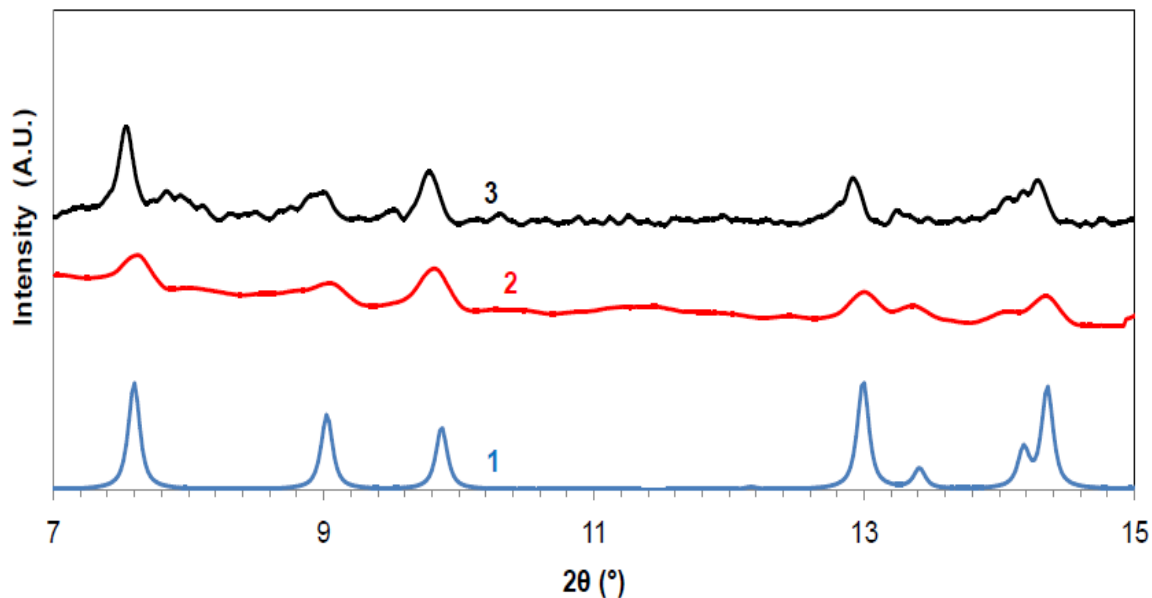


Figure 4.5 XRD patterns of Cu-hfipbb crystals taken before (marked as **2**) and after (marked as **3**) adsorption measurements, and comparison with the simulated XRD patterns of the crystal structures (marked as **1**).

4.3.2 Synthesis, Deposition and Characterization of ZIF-90 MOF

4.3.2.1 Synthesis of ZIF-90 Crystals

The synthesis procedure for ZIF-90 crystals was obtained from Bae et al. [64]. To synthesize ZIF-90, 20 mmol (1.920 g) Imidazole Carboxyaldehyde (ImCA) was added to 50 mL DMF and heated to 70°C for 1 hour until dissolved. After cooling to room temperature, 5 mmol (1.485 g) Zinc nitrate hexahydrate dissolved in 50 mL methanol was poured into the DMF/ImCA mixture and stirred for 30 min. The crystals were purified by three cycles of centrifugation and washing with methanol. The identity and high crystallinity of the synthesized MOF materials was verified by X-ray diffraction.

4.3.2.2 Deposition of ZIF-90 Crystals on QCM Substrates

A 3 g/L suspension of ZIF-90 MOF crystals was formed in a methanol, and sonicated for 60 min. ZIF-90 crystals were drop-coated by depositing about 100 μ l on the QCM substrate. The substrates were then pre-baked in an oven at 195°C and atmospheric pressure for 30 min. The samples were then mounted in the measurement apparatus and degassed *in situ* at a temperature of 185°C under vacuum for about 12 hours before adsorption measurements [71].

4.3.2.3 Characterization of ZIF-90 MOF Material

Following the ZIF-90 MOF material deposition on the QCM, the samples were examined by SEM and XRD before and after the adsorption measurements to ensure that the structure of the MOF was preserved throughout the experiment. From the SEM images in Figure 4.6, it is apparent that the size distribution of the ZIF-90 particles was considerably narrower (300-500 nm, Figure 4.6) and were of uniform shape. The distribution of the sample on the QCM is not uniform as we can see patches of the gold substrate. The PXRD patterns of the deposited ZIF-90 MOF samples obtained before and after the adsorption measurement, were generally consistent with the simulated PXRD patterns of highly crystalline ZIF-90 (see Figure 4.7).

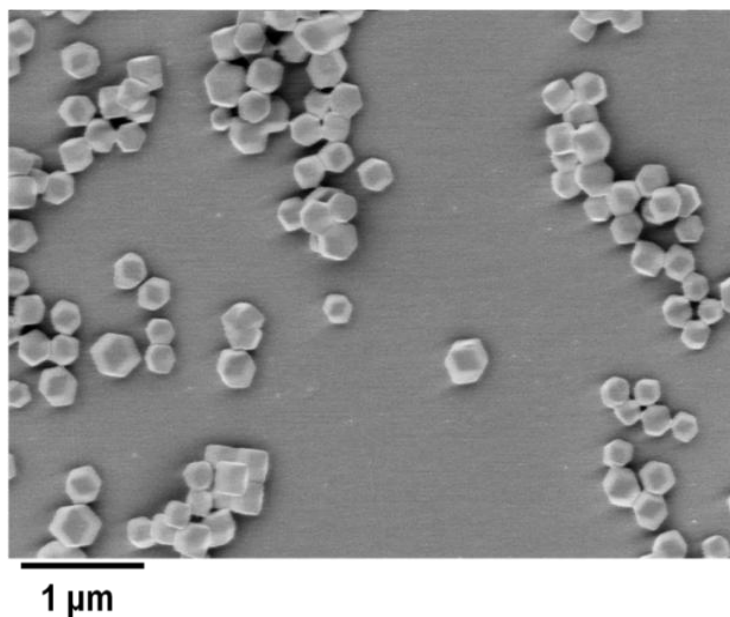


Figure 4.6 ZIF-90 crystals deposited on the gold surface of the QCM.

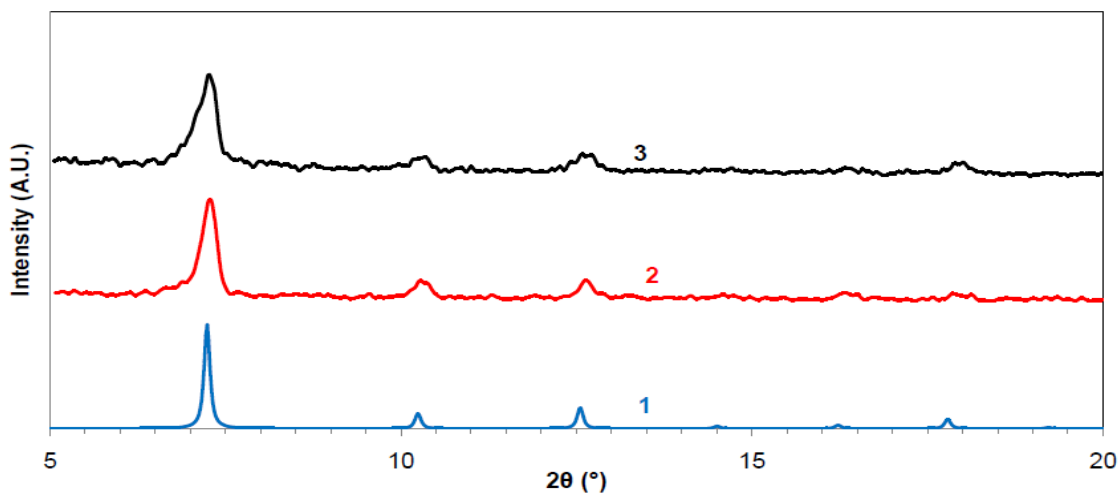


Figure 4.7 XRD patterns of ZIF-90 crystals, taken before (marked as **2**) and after (marked as **3**) adsorption measurements, and comparison with the simulated XRD patterns of the crystal structures (marked as **1**).

4.3.3 Synthesis, Deposition and Characterization of Cu-hfipbb MOF (large crystals)

4.3.1.1 Synthesis of Cu-hfipbb MOF Crystal (large crystals)

The large crystals of Cu-hfipbb were synthesized following the procedure of Ranjan et al. [20]. Specifically, 0.73 g of hfipbb ligand was dissolved in 5 mL of methanol and then diluted to 30 mL with DI water. Subsequently, 0.144 g of Copper (II) nitrate trihydrate was added to the solution. The solution was then heated for 6 hrs at 150°C. After cooling, the crystals were isolated via centrifugation and washed with isopropanol. The synthesis procedure was lengthened to 24 hours to grow longer crystals in another batch. The identity and high crystallinity of the synthesized MOF materials was verified by X-ray diffraction and the deposited crystals were studied under SEM.

4.3.1.2 Deposition of Cu-hfipbb MOF Crystals on QCM Substrates (large crystals)

During the synthesis, two batches of Cu-hfipbb MOF suspension was formed in isopropanol. Batch 1 was made with Cu-hfipbb MOF crystals with a synthesis period of 6 hours and batch 2 with a synthesis period of 24 hours under identical conditions. From both the batches a 3 g/L suspension was formed with isopropanol. Cu-hfipbb crystals from batch 1 were drop-coated by depositing about 100 µl on the QCM substrate. The small sized crystals were added in order to improve adhesion of the large sized crystals on the QCM substrate. The substrates were then pre-baked in an oven at 180°C and atmospheric pressure for 30 min. The samples were then mounted in the measurement apparatus and degassed *in situ* at a temperature of 185°C under vacuum for about 12 hours before adsorption measurements

4.3.1.3 Characterization of Cu-hfipbb MOF Material (large crystals)

Following the Cu-hfipbb MOF material deposition on the QCM, the sample was examined by Scanning Electron Microscopy (SEM), and by Powder X-ray Diffraction (XRD) before and after the adsorption measurements to ensure that the structure of the MOF was preserved throughout the experiment. From the SEM images in Figure 4.8, it is apparent that the Cu-hfipbb crystals have a wide size distribution ranging from 20 - 100 μm . The PXRD patterns of the deposited Cu-hfipbb MOF samples obtained before and after the adsorption measurement, were generally consistent with the simulated PXRD patterns of highly crystalline Cu-hfipbb (see Figure 4.9).

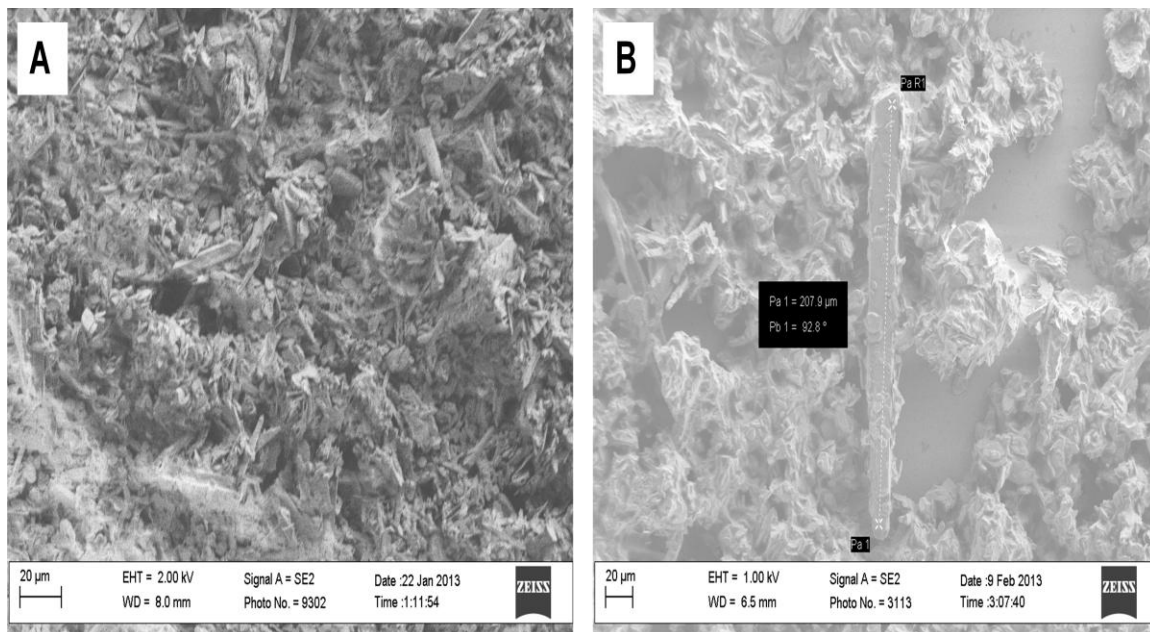


Figure 4.8 Cu-hfipbb crystals deposited on the gold surface of the QCM. **(A)** crystals obtained after 6 hrs of synthesis, **(B)** crystals obtained after 24 hr synthesis

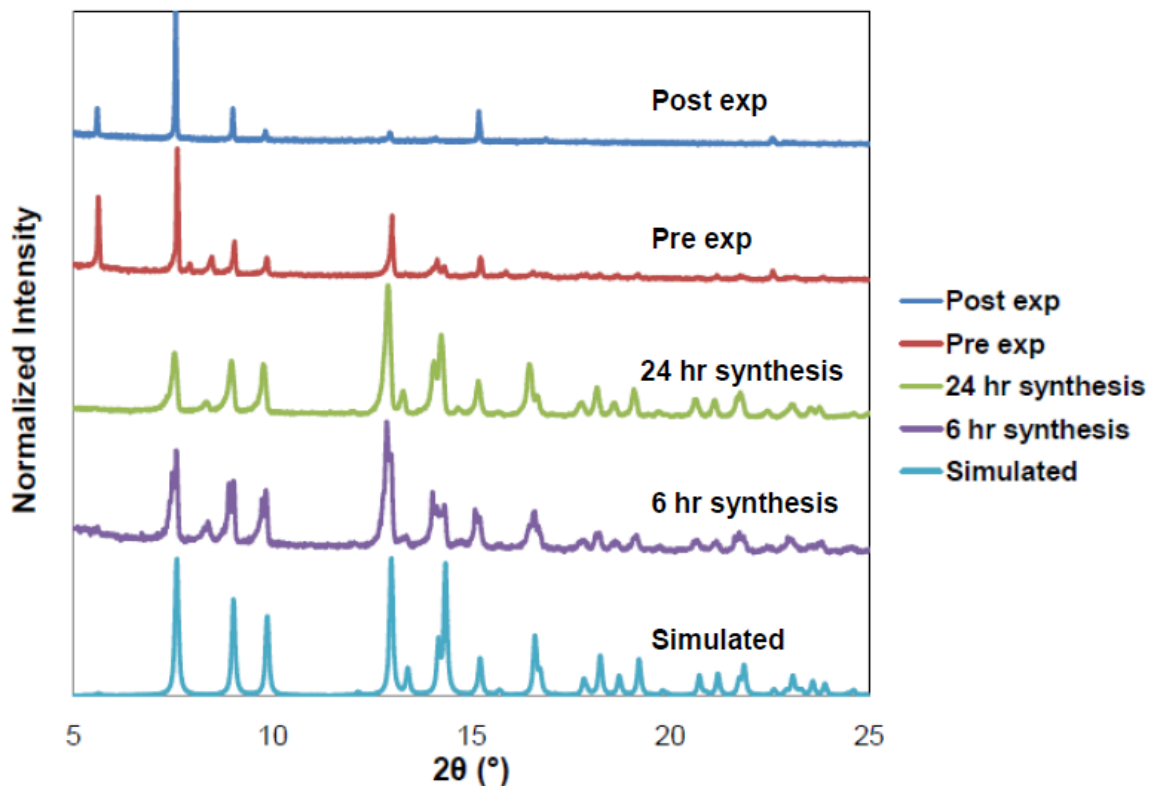


Figure 4.9 XRD patterns of Cu-hfipbb crystals taken before (**Pre exp**) and after (**Post exp**) adsorption measurements, and compared with the **simulated** and synthesized crystals (**6 hr synthesis** and **24 hr synthesis** time) XRD patterns of the crystal structures.

4.4 Gas Adsorption Measurements using Metal Organic Frameworks

4.4.1 Gas Adsorption Measurements from Cu-hfipbb MOF (small crystals)

Following the initial characterization, single-component adsorption isotherms of CO_2 , CH_4 , and N_2 in the Cu-hfipbb MOF were then collected at different temperatures ranging from 30-70°C and pressures ranging from 0.3-110 psi (about 7.5 atm). Measurements were taken in pressure intervals of 2-3 psi (below 1 atm) and ~14 psi (above 1 atm). The experimental isotherms were then analyzed in terms of a simple

Langmuir model (equations 4.1 & 4.2) to obtain thermodynamic parameters like adsorption capacity (C_H) and heat of adsorption (ΔH_a).

Following the initial degassing at 185°C under vacuum, the chamber was cooled down to room temperature and the mass of Cu-hfipbb MOF deposited was measured to be 404.7 µg (sample 1). Gas adsorption isotherms were then collected at temperatures 30°C, 50°C and 70°C for pressures up to 100 psi. Figures 4.10A-C shows the adsorption isotherms for CO₂, CH₄ and N₂ on Cu-hfipbb at different temperatures. An additional CO₂ gas adsorption isotherm was obtained at 25°C and compared to available gravimetric data 25°C (Figure 4.10A). For this comparison a separate sample was prepared and the mass of Cu-hfipbb MOF deposited on the QCM for this comparison was 262.36 µg (sample 2), and the sample preparation and pretreatment procedure of this sample was the same as in sample 1. At low and moderate pressures, there is good agreement of the two isotherms (gravimetric and QCM based sorption), but at higher pressures there are some deviations. The reasons for this behavior are not fully understood. It should be noted that when the adsorption data was collected at 25 °C with sample 2, repeated adsorption isotherms at 30 °C for CO₂ and CH₄ were collected for comparison with the corresponding data obtained from sample 1. Since the main aim of adsorption measurement in sample 2 was to compare the data collected at 25 °C from the QCM based sorption to that obtained from the gravimetric sorption at comparable temperature and pressure, detailed experiments were not conducted with sample 2. However the comparison between the two samples at 30 °C for CO₂ and CH₄ is presented in Figure A.2 in Appendix A. From the figure it was observed that there is an excellent agreement between the two samples.

The adsorption isotherms (at 30-70°C) obtained from the QCM-based high pressure sorption apparatus were then fit with the Langmuir isotherm (equations 4.1 - 4.2) and the key adsorption properties (enthalpy of adsorption, adsorption capacity, and pre-exponential entropic factor) were obtained as shown in Table 4.1. The average relative error (%) between the model and the experimental data is shown in Table 4.2.

A fundamental assumption of the Langmuir model is that adsorption occurs as a monolayer on the internal pore surfaces of the material, with all surface binding sites being equivalent and accommodating one adsorbed molecule. Furthermore, the ability of a molecule to adsorb at a given site is independent of the occupancy of neighboring sites. As explained earlier, Cu-hfipbb is a crystalline interpenetrating MOF containing 1D channels, and has cages of dimensions 5.1 x 5.1 Å connected by smaller windows of dimensions 3.5 Å x 3.2 Å as shown in Figure 4.1. The kinetic diameters of CO₂, CH₄ and N₂ molecules are 3.3 Å, 3.8 Å and 3.6 Å respectively [88]. Considering the comparable dimensions of the pore channels and the kinetic diameters of the gas molecules, we can infer that the penetrant gases are most likely to adsorb in a monolayer, hence leading to a good fit of the Langmuir model to obtain the adsorption properties. Further previous research has shown that nanoporous materials like Cu-hfipbb who have comparable structures to Zeolites and other porous materials [26, 85, 94] can be modeled with simple analytical isotherms like Langmuir isotherm model. From our experimental results we see that the adsorption capacity of CO₂, CH₄ and N₂, as well as the heat of adsorption, are in decreasing order. It is clear that CO₂ shows the strongest adsorption affinity towards the Cu-hfipbb framework, owing to its quadrupole moment [19]. Although the kinetic diameter of CH₄ is slightly greater than that of N₂, which may cause it to diffuse more

slowly in the material, it is thermodynamically more favored for adsorption in Cu-hfipbb than N₂.

Comparing the current experimental results with the previous simulation study [19], it is seen that the experimental single-component adsorption isotherms of CO₂ (at 25°C and 30°C) in Cu-hfipbb compares well with the simulated single-component adsorption isotherm at 25°C at high pressures (> 1 atm), while at low pressures the predicted adsorption is higher than the experimental measurements. This strongly indicates that the force field models and atomic charges used to simulate the adsorbate-framework interactions may require fine-tuning. At higher pressures, adsorbate-adsorbate interactions dominate and better agreement of the simulations with experimental data is seen. Single-component methane adsorption simulations in Cu-hfipbb at 25°C were also reported recently [19]. A trend similar to that of CO₂ is seen in the comparison of experimental and simulated data. We also compared the heats of adsorption of CO₂ and CH₄ from the simulation results (-9.7 kJ/mol for CO₂ and -5.8 kJ/mol for CH₄) with the experimentally obtained heats of adsorption (-21.3 kJ/mol for CO₂ and -16.1 kJ/mol for CH₄). The experimental results suggest that quantitative interpretation of currently available adsorption simulation data in Cu-hfipbb must be made with caution. As mentioned earlier [19], errors in estimation of interatomic forces (e.g., the attractive dispersion forces) could have a significant impact on the accuracy of computational predictions.

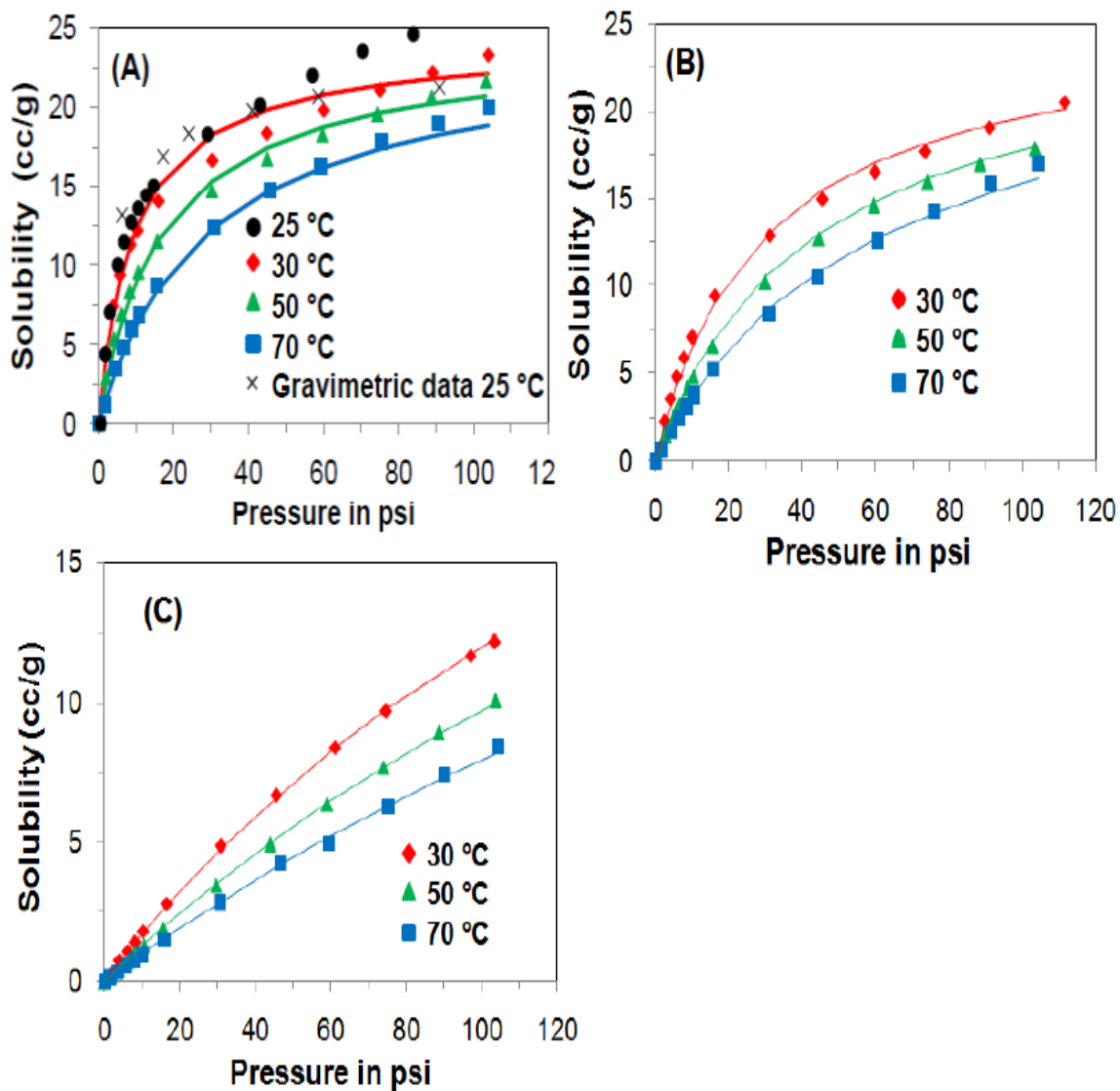


Figure 4.10 Solubility of gases (in cc STP/g) at 25°C (only CO₂), 30°C, 50°C and 70°C in the MOF Cu-hfipbb. (A) CO₂ adsorption isotherms at different temperatures, with a gravimetrically-measured CO₂ adsorption isotherm at 25°C; (B) CH₄ and (C) N₂ adsorption isotherms at different temperatures. Langmuir model fits are represented by the solid lines.

Table 4.1 Adsorption parameters for Cu-hfipbb based on the Langmuir model.

Gas	C_H (cc/g)	α_0 (psi ⁻¹) x 10 ⁻⁶	ΔH_a (kJ/mol)
CO ₂	24.1 ± 0.61	20.3 ± 0.52	-21.3 ± 0.54
CH ₄	25.4 ± 0.52	56.3 ± 1.15	-16.1 ± 0.33
N ₂	37.8 ± 0.99	33.4 ± 0.88	-12.4 ± 0.33

Table 4.2 Average relative error (%) between the experimental data and the Langmuir adsorption model for Cu-hfipbb.

Average Relative Error (ARE) (%)	30°C	50°C	70°C
CO ₂	3.28	2.87	1.49
CH ₄	3.66	1.09	1.38
N ₂	1.18	3.62	3.07

4.4.2 Gas Adsorption Measurements from ZIF- 90

Following the initial characterization, single-component adsorption isotherms of CO₂, CH₄, and N₂ in the ZIF-90 MOF were then collected at different temperatures ranging from 30-70°C and pressures ranging from 0.3-120 psi (about 8 atm). Measurements were taken in pressure intervals of 2-3 psi (below 1 atm) and ~14 psi

(above 1 atm). The experimental isotherms were then analyzed in terms of a Henry's Law (equation 4.3) to obtain thermodynamic parameters like Henry's Constant (K_H).

Following the vacuum degassing at 185°C, the sample chamber was cooled down to room temperature and the mass of the ZIF-90 MOF deposited on the QCM was measured. For gas adsorption measurements using ZIF-90, two samples were prepared. Sample 1 was measured to have 164 µg of ZIF-90 and was suitable for CO₂ and CH₄ adsorption measurements. N₂ adsorption isotherms were measured with Sample 2 (258 µg of ZIF-90), since N₂ was found to adsorb quite weakly in ZIF-90 and a larger sample is required in order to obtain valid results. Separate samples were used for CO₂, CH₄ and N₂, and furthermore adsorption isotherms from different samples were measured for CO₂ and CH₄ at 30°C for the same pressure range and were found to be identical. The adsorption isotherms for ZIF-90 were collected at temperatures of 30°C, 50°C and 70°C and pressures up to 110 psi. From the literature search, it was found that previous measurements were available for temperature ranges beyond the capability of the current setup (@ 77 K for N₂) [21] and hence are not presented. Figures 4.11A-F show the gas adsorption isotherms for CO₂, CH₄, and N₂ respectively collected at different temperatures. These adsorption isotherms were first fit with the Langmuir model. However, a poor fit of the experimental data was obtained. The ZIF-90 pore structure comprises large cages of size 11.2 Å connected by small windows of size 3.5 Å. Considering the pore structure and the kinetic diameter of the gas molecules considered in this paper, it is clear that adsorption will not obey a Langmuir model at moderate and higher pressures, due to possible multilayer adsorption in the cages. Therefore, one can only obtain parametric information on the adsorption characteristics in the low-pressure

regime wherein Henry's law can be applied (Table 4.3, Fig 4.11 B, D and F). The average relative % error between the model and the experimental data is shown in Table 4.4. It is found that CO₂ is the most thermodynamically favored, followed by CH₄ and then N₂. As expected, the Henry's constants decrease with increasing temperature. The detailed gas adsorption data presented in this work facilitates further detailed analyses using statistical thermodynamic models and molecular simulations of gas adsorption in ZIF-90, which serves as a good exemplar of the ZIF class of porous materials.

Table 4.3 Henry's constants for gas adsorption in ZIF-90.

K_H (cc/g.psi)	30°C	50°C	70°C
CO ₂	1.28 ± 0.05	0.73 ± 0.05	0.23 ± 0.02
CH ₄	0.34 ± 0.003	0.26 ± 0.023	0.22 ± 0.015
N ₂	0.32 ± 0.022	0.11 ± 0.02	0.088 ± 0.01

Table 4.4 Average relative error (%) between the experimental data and the Henry's adsorption model for ZIF-90.

Average Relative Error (ARE) (%)	30°C	50°C	70°C
CO ₂	3.67	7.11	10.11
CH ₄	0.82	8.74	6.75
N ₂	6.90	16.33	12.33

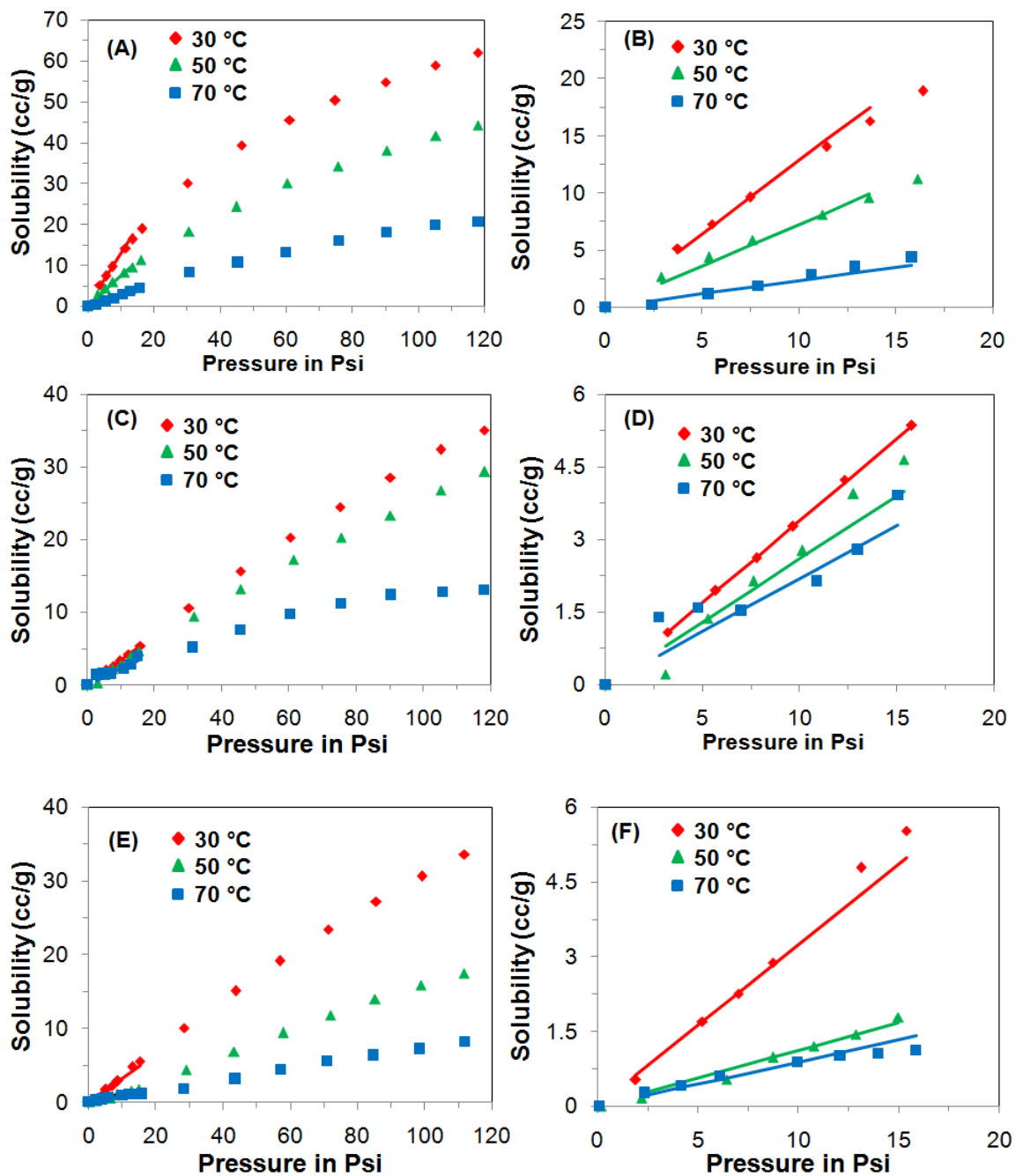


Figure 4.11 Solubility of gases (in cc STP/g) at 30°C, 50°C and 70°C in the MOF ZIF-90. CO₂ (A & B), CH₄ (C & D), and N₂ (E & F) adsorption isotherms for the entire pressure range studied, and the sub-atmospheric pressure range, respectively. Henry's constant is fitted in the sub-atmospheric pressure range as represented by the solid lines.

4.4.3 Gas Adsorption Measurements from Cu-hfipbb MOF (large crystals)

Following the initial characterization, single-component adsorption isotherms of CO₂, CH₄, N₂, Ethylene and n-Butane in the Cu-hfipbb MOF were then collected at different temperatures ranging from 25-100°C and pressures ranging from 0.3-100 psi. The high diffusion selectivity (CO₂/CH₄) of the order of 10⁴ - 10⁵ was the prime motivating factor for this study with Cu-hfipbb MOF. Previous study with Cu-hfipbb (section 4.4.1) was done with small crystals (< 2 μm) and could not yield reliable diffusion parameters. Hence this study with large crystals was performed. The experimental isotherms were then analyzed in terms of a simple Langmuir model (equations 4.1 & 4.2 for CH₄, N₂ and n-Butane) and Dual mode adsorption model (equations 3.5, 3.6 and 3.8 for CO₂ and Ethylene) to obtain the thermodynamic parameters of adsorption.

Following the initial degassing at 180°C under vacuum, the chamber was cooled down to room temperature and the mass of Cu-hfipbb MOF deposited was measured to be 460.3 μg. Figures 4.12A-E shows the adsorption isotherms for CO₂, CH₄, N₂, Ethylene and n-Butane on Cu-hfipbb at different temperatures. The adsorption isotherms obtained from the QCM-based high pressure sorption apparatus were then fit with the Langmuir isotherm (equations 4.1 & 4.2 for CH₄, N₂ and n-Butane) and Dual mode adsorption model (equations 3.5, 3.6 and 3.8 for CO₂ and Ethylene) to obtain the key adsorption properties as shown in Table 4.5. From the average relative error (%) between the model and the experimental data shown in Table 4.6, we can infer that there is a high quality of fit between the experimental and model isotherms.

The applicability of Langmuir model to study adsorption in Cu-hfipbb pores has been previously explained in section 4.4.1. Hence considering the comparable dimensions of the pore channels and the kinetic diameters of the gas molecules, we can infer that the penetrant gases are most likely to adsorb in a monolayer in the pores, hence leading to a good fit of the Langmuir model to obtain the adsorption properties. As in section 4.4.1, all the gases were fit with Langmuir model and showed acceptable degree of error and matched with comparable previous literature data (CO₂, CH₄ and N₂) [71]. However in the case of CO₂ and Ethylene, there was scope for improvement in the quality of the fit. Hence CO₂ and Ethylene were fit with Dual mode model, consisting of Langmuir mode for adsorption in the pores and adsorption in the interstitial spaces given by Henry's mode. From our experimental results we see that the adsorption favorability within the pores are in the descending order of n-Butane > CO₂ > Ethylene > CH₄ > N₂. In the case of CO₂ and Ethylene, the addition of Henry's part improves the quality; however it remains a smaller fraction compared to Langmuir part. Hence Langmuir mode of adsorption remains the dominant mode of adsorption in Cu-hfipbb.

Further on comparing the adsorption measurements (CO₂, CH₄ and N₂) obtained from the Cu-hfipbb samples (small and large crystals) in Figure 4.13, it was observed that there are some differences in the equilibrium adsorption isotherms between the two samples, more strongly observed in the case of CO₂ than in CH₄ and N₂. This may be due to sample to sample inhomogeneity although the exact reason for this deviation is not known. However the CO₂ adsorption isotherm obtained at 25°C from the small and large sized crystals agree very well. In general, the adsorption isotherms between the two samples are comparable.

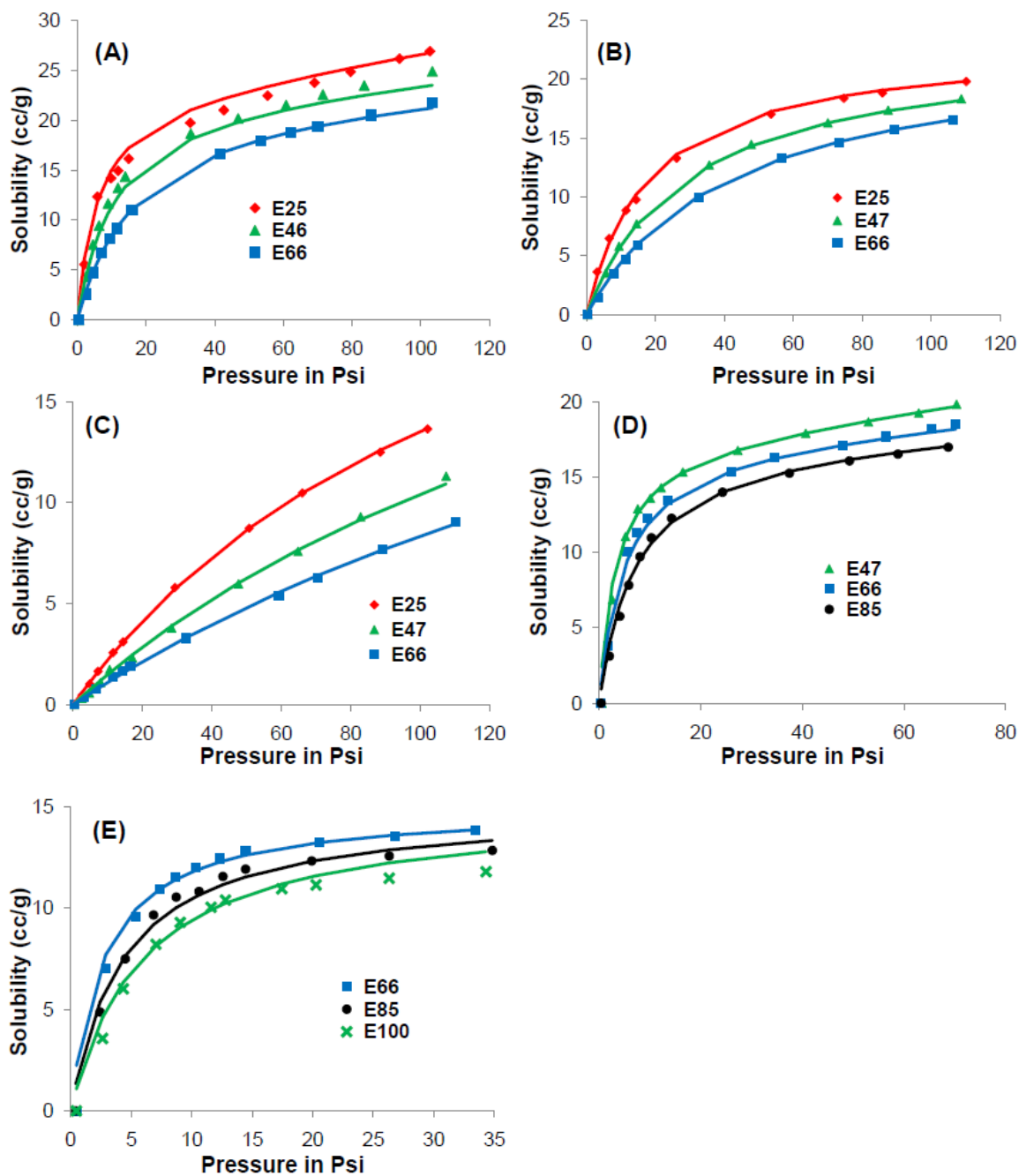


Figure 4.12 Solubility of gases (in cc STP/g) at different temperatures in the MOF Cu-hfipbb. (A) CO₂ adsorption isotherms at different temperatures, (B) CH₄ and (C) N₂, (D) Ethylene and (E) n-Butane. The fits with simple analytical models like Langmuir (for CH₄, N₂ and n-Butane) and dual mode adsorption model (CO₂ and Ethylene) are represented by the solid lines.

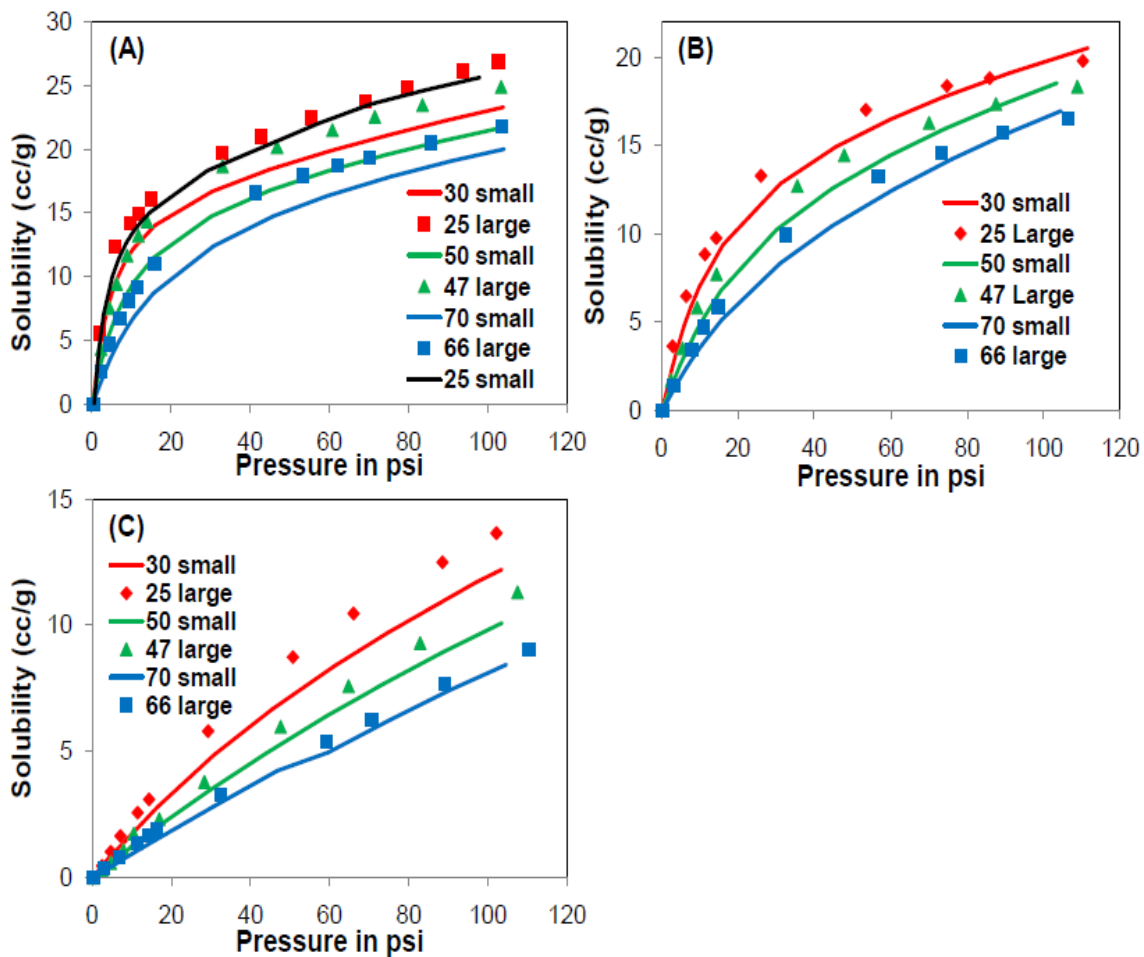


Figure 4.13 Comparison of gas adsorption isotherm obtained from large and small sized Cu-hfipbb crystals at different temperatures. (A) CO₂, (B) CH₄ and (C) N₂. Isotherms obtained from large sized Cu-hfipbb crystals are represented by markers and that obtained from small sized Cu-hfipbb crystals are represented by solid lines,

Table 4.5 Adsorption parameters for Cu-hfipbb based on the Langmuir model (CH₄, N₂ and n-Butane) and dual mode adsorption model (CO₂ and Ethylene)

Gas	C_H (cc/cc)	α₀ (psi⁻¹) x10⁻⁵	ΔH_a (kJmol⁻¹)	K_{d0} x10⁻⁶ (cc/cc.psi)	m
CO₂	22.5 ± 0.72	1.68 ± 0.053	-23 ± 0.74	1.12 ± 0.036	12.9 ± 0.41
CH₄	23.1 ± 0.67	5.56 ± 0.16	-17.1 ± 0.5	-	-
N₂	31 ± 1.77	1.74 ± 0.1	-15.1 ± 0.86	-	-
Ethylene	17.4 ± 0.61	22.1 ± 0.77	-19.3 ± 0.68	9.3 ± 0.33	12 ± 0.42
n-Butane	15 ± 0.59	7.92 ± 0.31	-23.8 ± 0.93	-	-

Table 4.6 Average relative error (%) between the experimental data and the Langmuir model (CH₄, N₂ and n-Butane) and dual mode adsorption model (CO₂ and ethylene) for Cu-hfipbb.

Average					
Relative Error (ARE) (%)	25°C	47°C	66°C	85°C	100°C
CO₂	3.75	2.74	3.18	-	-
CH₄	3.1	2.3	3.25	-	-
N₂	4.26	8.55	4.36	-	-
Ethylene	-	1.89	3.94	4.73	-
n-Butane	-	-	1.94	3.68	6.11

4.5 Sample Preparation and Characterization of AluminoSilicate Nanotubes

4.5.1 Synthesis of Bare Single Wall AluminoSilicate Nanotubes (BNTs)

Tetraethylorthosilicate (TEOS) was mixed with aluminum-tri-sec-butoxide in a glove box filled with nitrogen. The mixture was added to an aqueous 38mM perchloric acid solution with a molar ratio $\text{Si}:\text{Al}:\text{HClO}_4 = 1.1:2:1$, under vigorous stirring at room temperature in ambient conditions for 24 h. The solution was then diluted with DI water by a factor of 3.6 and refluxed at 95°C for 4 days. Once the temperature was brought to 95°C, the solution turned from cloudy to clear in about 1 h. After the solution was decreased to room temperature, a 30 wt % ammonia solution was added dropwise into the product solution until gelation of the suspended nanotubes occurred. The gel was isolated by centrifugation at 7000 rpm for 15 min. The supernatant was discarded, and a few drops of 10 N hydrochloric acid were added to the gel, thereby redispersing the nanotubes. The resulting viscous solution was purified by dialysis against DI water for 3 days using a 15k Dalton membrane. The purified suspension was dried at 60°C to obtain a powder sample of the SWNTs [27].

4.5.2 Synthesis of Aminomethyltriethoxysilane (AMTES)

AMTES was synthesized by treating the commercially available chloromethyltriethoxysilane with gaseous ammonia using a Parr reactor. The reaction was performed anhydrously at 900-1000 psi and 100°C for five hours. The synthesis detail was identical to that described in Brunelli et al. [27, 95].

4.5.3 Synthesis of Aminefunctionalized Single Wall AluminoSilicate Nanotubes (ANTs)

TEOS and AMTES were mixed with aluminum-tri-*sec*-butoxide in a glove box filled with nitrogen. The mixture, with a TEOS:AMTES:Al:HClO₄ molar ratio of (1-x): x: 2:1 was added into a Teflon jar (1000 mL capacity) containing 500 mL of 38 mM perchloric acid. Bare Aluminosilicate Nanotubes, referred to as ‘BNTs’, were obtained when $x = 0$; whereas ANTs’ were synthesized when $x = 0.2$. The aqueous mixture was vigorously stirred at room temperature in ambient conditions for 24 h. The solution was then diluted with DI water by a factor of 3.8 with respect to volume, and then stirred at 95°C for 96 h. Once the temperature was brought to 95°C, the solution turned from cloudy to clear in about one hour. After the solution was cooled to room temperature, a 30 wt% ammonia solution was added dropwise until gelation of the suspended nanotubes occurred. The gel was isolated by centrifugation at 7000 rpm for 10 min. The supernatant was discarded and a few drops of 10N hydrochloric acid were added to the gel, thereby re-dispersing the nanotubes. The gel was dialyzed against 10 wt% ammonium hydroxide solution for 24 h and then against DI water for 3 days, using a dialysis membrane with a 15 kDa molecular weight cutoff. To obtain powder samples, the purified gel was dried at 60 °C and then ground lightly to disperse the agglomerated nanotubes. Approximately 1 g of powder sample is obtained from a 1L synthesis batch volume [27, 93]. The morphology of the ANTs was evaluated by conventional and cryogenic TEM from which it was observed that the ANTs show a smaller average length than the NTs (The average length of NT is 160 nm and of ANT 50 nm) [93] while the outer diameter of the nanotubes was ~2.1nm and the inner pore diameter was ~1nm.

4.5.4 Deposition of BNTs and ANTs on QCM Substrates

Post synthesis, the as-synthesized Bare NT (BNTs) or Amine functionalized NT (ANTs) gel were drop-coated by depositing a few drops on the QCM substrate. The substrates were then pre-baked in an oven at 110°C and atmospheric pressure for 30 min. The sample deposited QCMs were studied using XRD for characterizing the substrate. Post initial characterization, the samples were then mounted in the measurement apparatus and degassed *in situ* at a temperature of 180°C under a vacuum of 6 mTorr for about 24 hours before adsorption measurements. Following the degassing by baking under vacuum, the samples were cooled down to the room temperature and the mass of NTs deposited on the surface of QCMs were measured. The mass of BNTs were measured to be 950 µg and that of ANTs were measured to be 1347.5 µg.

4.5.5 Characterization of the BNTs and ANTs Deposited on the QCM

Following sample deposition on the QCM and initial baking at atmospheric pressure, the samples were studied using XRD. Similarly after the baking and degassing under vacuum at 180°C, the samples were studied under XRD to ensure the structural integrity of the sample was preserved.

Figure 4.14 and Figure 4.15 shows the XRD patterns from BNTs and ANTs deposited on the QCM, pre and post experiment. From the plots we observe that there are no appreciable shifts in the peaks and that the structural integrity of the sample deposited on the QCM is preserved.

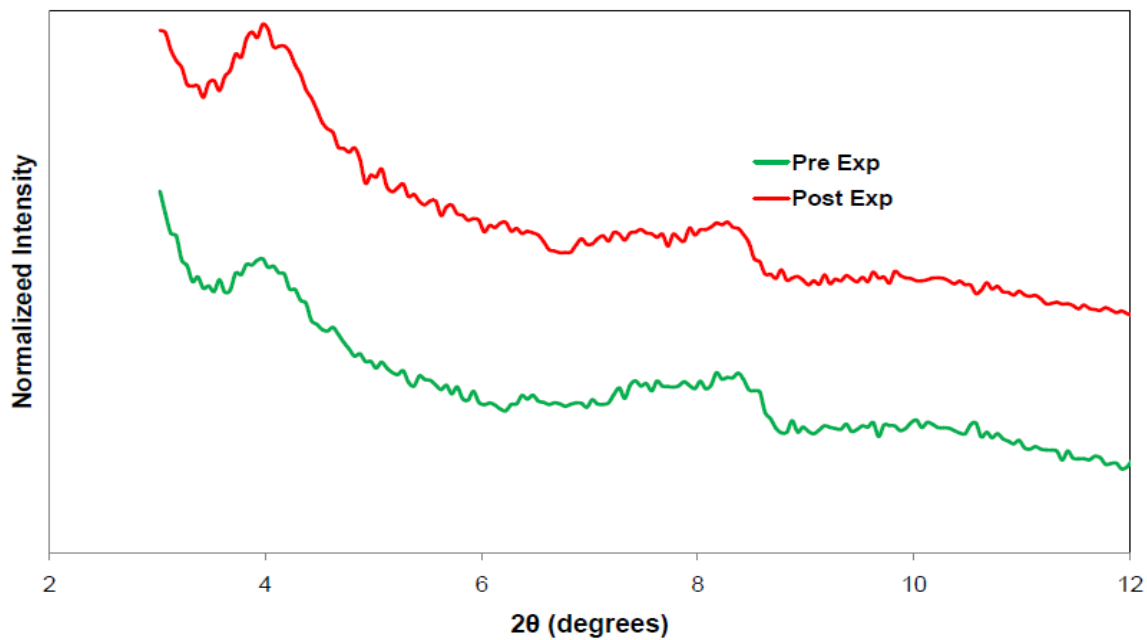


Figure 4.14 XRD pattern obtained from BNTs deposited on the QCM

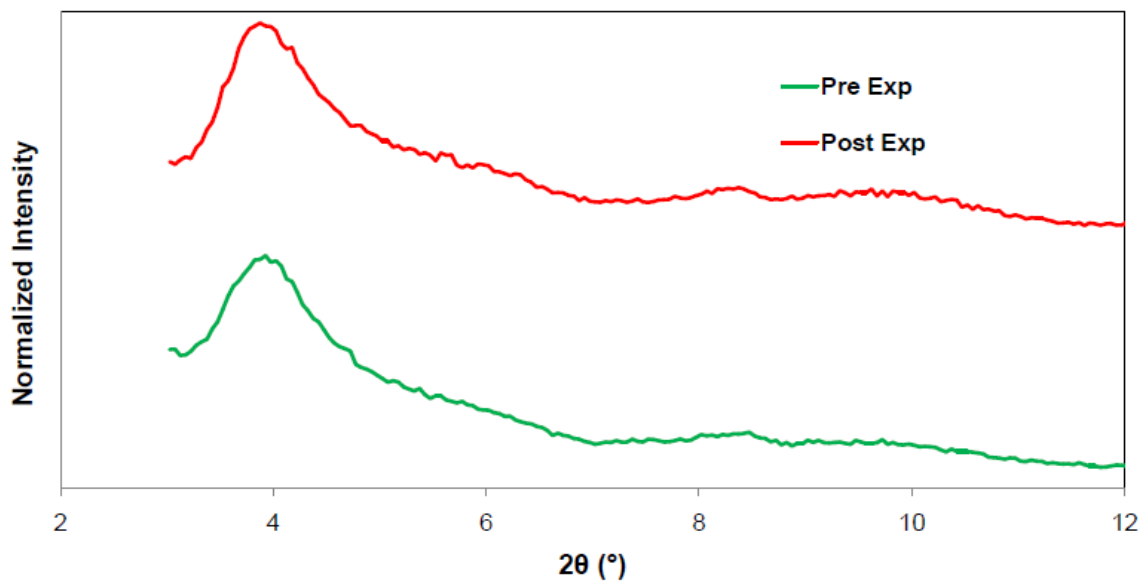


Figure 4.15 XRD pattern obtained from ANTs deposited on the QCM

4.6 Gas Adsorption Measurements using Nanotubes

4.6.1 Gas Adsorption Measurements from BNTs and its Modifications

Following the initial characterization, single-component adsorption isotherms of CO₂, CH₄, and N₂ in the BNTs and ANT_s were then collected at different temperatures ranging from 30-70°C and pressures ranging from 0.3-110 psi (about 7.5 atm). Measurements were taken in pressure intervals of 2-3 psi (below 1 atm) and ~40 psi (above 1 atm). The experimental isotherms were then analyzed in terms of a simple Langmuir model (equations 4.1 & 4.2) to obtain thermodynamic parameters like adsorption capacity (C_H) and heat of adsorption (ΔH_a).

Following the initial degassing at 180°C under vacuum, the chamber was cooled down to room temperature and the mass of BNTs and ANT_s deposited were measured to be 950 μg and 1347.5 μg respectively. Figure 4.16 shows the gas adsorption isotherms from BNTs for CO₂, CH₄ and N₂ at different temperatures for pressures up to 120 psi fitted with Langmuir adsorption model. The thermodynamic adsorption parameters obtained from the fit and the corresponding measure for the quality of the fit are presented in Tables 4.7 & 4.8 respectively. From the Table 4.7 and Figure 4.16, we observe that compared to CO₂ and CH₄, N₂ has a lower capacity of adsorption. Further from Table 4.8, it can be inferred that there is generally a high quality of fit between the Langmuir model and the adsorption data. The reason to choose Langmuir adsorption model is given below.

A fundamental assumption of the Langmuir model is that adsorption occurs as a monolayer on the internal pore surfaces of the material, with all surface binding sites being equivalent and accommodating one adsorbed molecule. Furthermore, the ability of

a molecule to adsorb at a given site is independent of the occupancy of neighboring sites. As explained earlier, BNT's are crystalline small pore nanotube with pore diameter (ID) of 10 Å, outer diameter (OD) of 21 Å and are 160 nm in length as shown in Figure 4.3A. The kinetic diameters of CO₂, CH₄ and N₂ molecules are 3.3 Å, 3.8 Å and 3.6 Å respectively [88]. Considering the comparable dimensions of the pore channels and the kinetic diameters of the gas molecules, we can infer that the penetrant gases are most likely to adsorb in a monolayer, hence leading to a good fit of the Langmuir model to obtain the adsorption properties.

Following the gas adsorption measurement with BNTs, adsorption measurement with ANTs was conducted. The degassing and sample mass measurement procedures were similar to that of BNTs. Figures 4.17, 4.18 & 4.19 presents the gas adsorption measurement with ANTs for CO₂, CH₄ and N₂ respectively and compares the corresponding gas uptake with the BNTs. From the plots we can infer that the ANTs show a decreased gas uptake at comparable pressures and temperatures. This is possible due to steric constraints due to the amine functionalization. The diameters (ID and OD) of the ANTs are the same as that of BNTs and are of shorter length compared to the BNTs, 50 nm ANT versus 160 nm for the BNT. Hence Langmuir adsorption model may be applicable to ANTs to obtain the adsorption parameters.

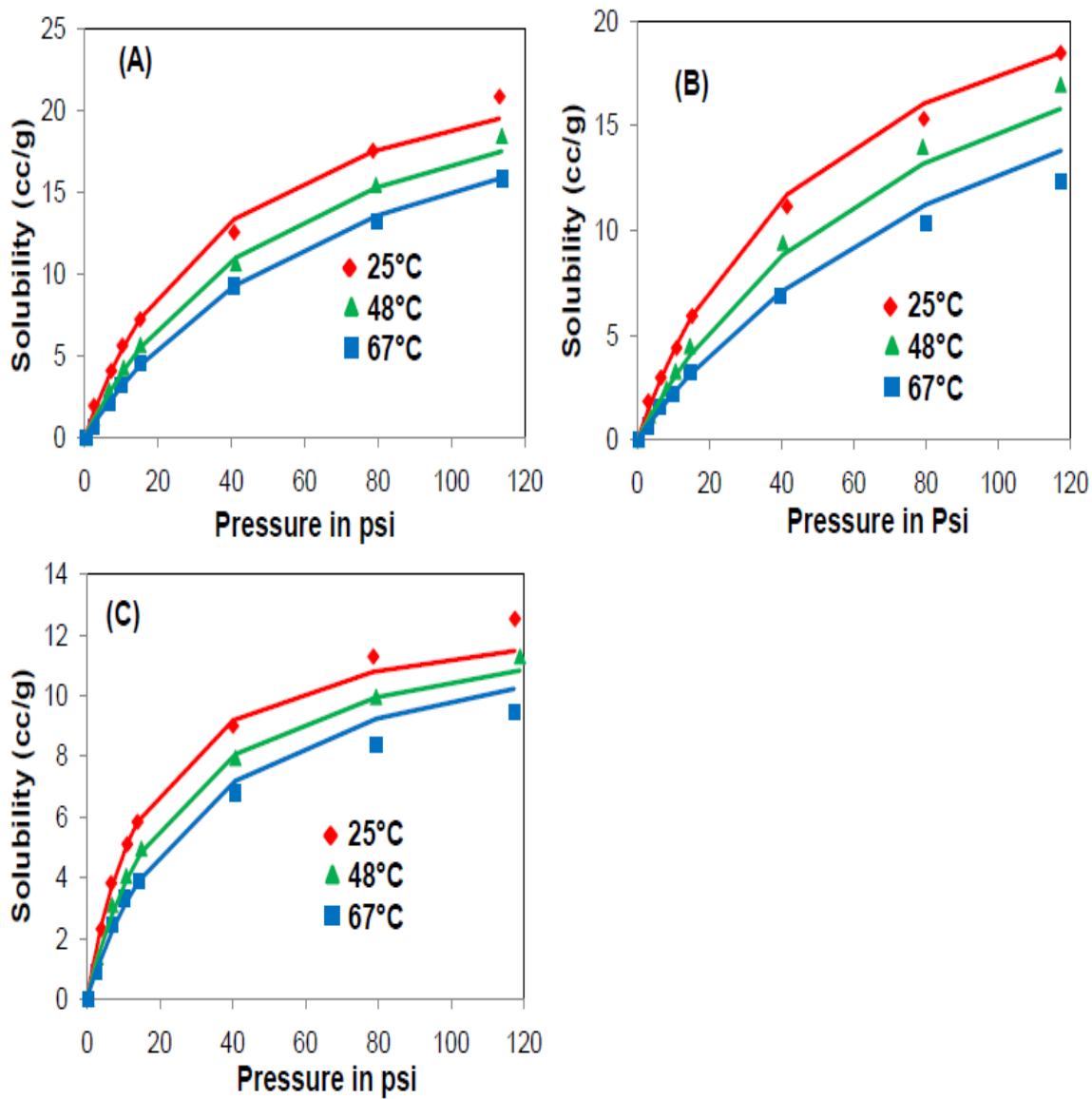


Figure 4.16 Solubility of gases (in cc STP/g) at 25°C, 48°C and 67°C in the BNTs. **(A)** CO₂ adsorption isotherms at different temperatures. **(B)** CH₄ and **(C)** N₂ adsorption isotherms at different temperatures. Langmuir model fits are represented by the solid lines.

Table 4.7 Adsorption parameters for BNTs based on the Langmuir model.

Gas	C_H (cc/g)	α_0 (psi ⁻¹) x 10 ⁻⁴	ΔH_a (kJ/mol)
CO ₂	26.31 ± 1.2	1.57 ± 0.07	-12.58 ± 0.57
CH ₄	27.01 ± 1.4	0.57 ± 0.03	-14.3 ± 0.76
N ₂	13.19 ± 0.6	2.93 ± 0.13	-13.05 ± 0.58

Table 4.8 Average relative error (%) between the experimental data and the Langmuir adsorption model for BNTs.

Average Relative Error (ARE) (%)	25°C	48°C	67°C
CO ₂	5	4	4.4
CH ₄	5	6	5
N ₂	3.8	3.8	5.9

Figures 4.17 (C & D), 4.18 (C & D) and 4.19 (C & D) show the gas adsorption isotherm for ANTs fitted with Langmuir model for pressures up to 1 atm. Initial efforts to fit the entire pressure range with Langmuir model did not yield satisfactory results. As mentioned previously, the gas adsorption isotherm for BNTs can be fit with Langmuir isotherm model for the entire pressure range (0-120 psi). However for ANTs, due to the steric effects of the amine functionalization, there may be complex interactions at high pressures which are currently not fully understood. Hence the Langmuir adsorption model was fit only up to 1 atm. Tables 4.9 and 4.10 shows the thermodynamic adsorption

parameters and the quality of fit in terms of average relative error respectively. From Table 4.9, we observe significant reduction in adsorption capacity in the amine functionalized molecule. This corroborates the fact that there are effects of steric interactions in amine functionalized molecule that lead to lower adsorption. From Table 4.10, we observe that there is in general a high quality of fit between the Langmuir model and the adsorption data for the chosen pressure range.

The primary reason for this study was to understand quantitatively the adsorption selectivity of ANTs in relation to the BNTs. In that regard, Figure 4.20 compares the adsorption selectivity (CO_2/CH_4 & CO_2/N_2) between BNTs and ANTs. The selectivity was measured by fitting individual isotherms with Langmuir isotherm and then recalculating the adsorption at specific pressures. Using the calculated isotherm, the adsorption selectivity was found at specific temperature and pressures. From the plots, it can be observed that the ANTs with a 15% aminomethyl group substitution for hydroxyls exhibit a dramatic improvement in selectivity over the BNTs for both CO_2/CH_4 (up to four-fold increase) and CO_2/N_2 (up to ten-fold increase). It should be noted that only the adsorption selectivity at 25°C and 67°C show a distinct behavior (adsorption selectivity at 47°C is very similar to 25°C) and hence further analysis will be presented only for these two temperatures.

To gain more insight into the observed selectivity enhancements and evaluate the affinity of the ANT and BNT walls for the adsorbate molecules, the Henry's constants for adsorption in each nanotube material were deduced from fits of the full isotherms to the Langmuir model ($K_H = C_H \alpha$). The Henry's constant ratios between ANTs and BNTs ($K_{\text{ANT}}/K_{\text{BNT}}$) are summarized in Table 4.11. The detailed Langmuir fitting parameters and

the isotherms are presented below in Table 4.12 and Figure 4.21. In general, the Henry's constants decrease for all the adsorbates when partially replacing surface hydroxyl groups with aminomethyl groups. This suggests that the isolated aminomethyl ($\equiv\text{Si-CH}_2\text{NH}_2$) groups in the ANTs in fact possess a weaker affinity for the adsorbates in comparison to the hydroxyls ($\equiv\text{Si-OH}$) groups. The Henry's constant reduction is much more significant for CH_4 and N_2 than for CO_2 , a phenomenon that provides the main contribution to the enhanced CO_2/CH_4 and CO_2/N_2 selectivity.

The smaller reduction of Henry's constant for CO_2 is likely due to the mechanisms of amine group binding to CO_2 molecules. Specifically, previous studies show that one equivalent of a free base moiety, typically water, is needed for a primary amine to adsorb one equivalent of CO_2 [96, 97]. However, under anhydrous conditions such as in the present adsorption measurements, two adjacent primary amines are required to adsorb one equivalent of CO_2 . The primary amine groups are expected to be distributed in a random manner at the inner surface of the ANTs, and there is no evidence available for preferred clustering of the aminomethylsilane groups. Given the adsorption mechanism discussed above, amine groups that have a second amine group nearby, immobilized on a concaved surface with high degree of curvature, may provide a positive contribution to CO_2 adsorption, whereas the isolated amines would likely show lower CO_2 affinity than the surface hydroxyls. These two competing effects, present only for CO_2 adsorption but not for CH_4 and N_2 , are likely to be the key factor leading to a relatively small reduction of Henry's constant for CO_2 and the high CO_2/CH_4 and CO_2/N_2 selectivity in ANTs [93].

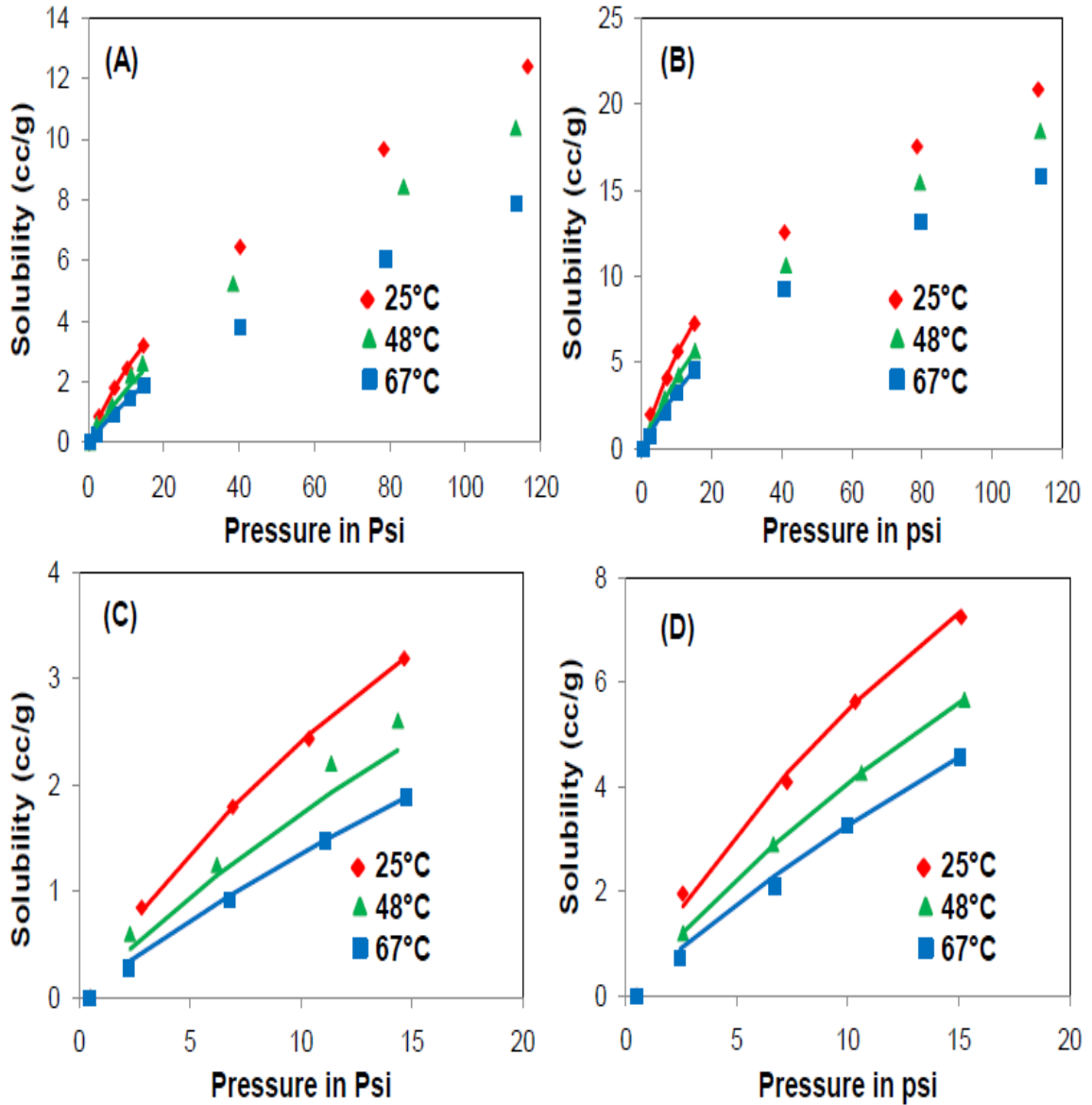


Figure 4.17 Solubility of CO₂ (in cc STP/g) at 25°C, 48°C and 67°C in the ANTs (**A & C**) and Bare AISi NTs (**B & D**). Adsorption isotherms for the entire pressure range (0-120 psi) presented in (**A & B**) and the sub-atmospheric pressure range (**C & D**), respectively. Langmuir adsorption model is fitted in the sub-atmospheric pressure range as represented by the solid lines (**C & D**).

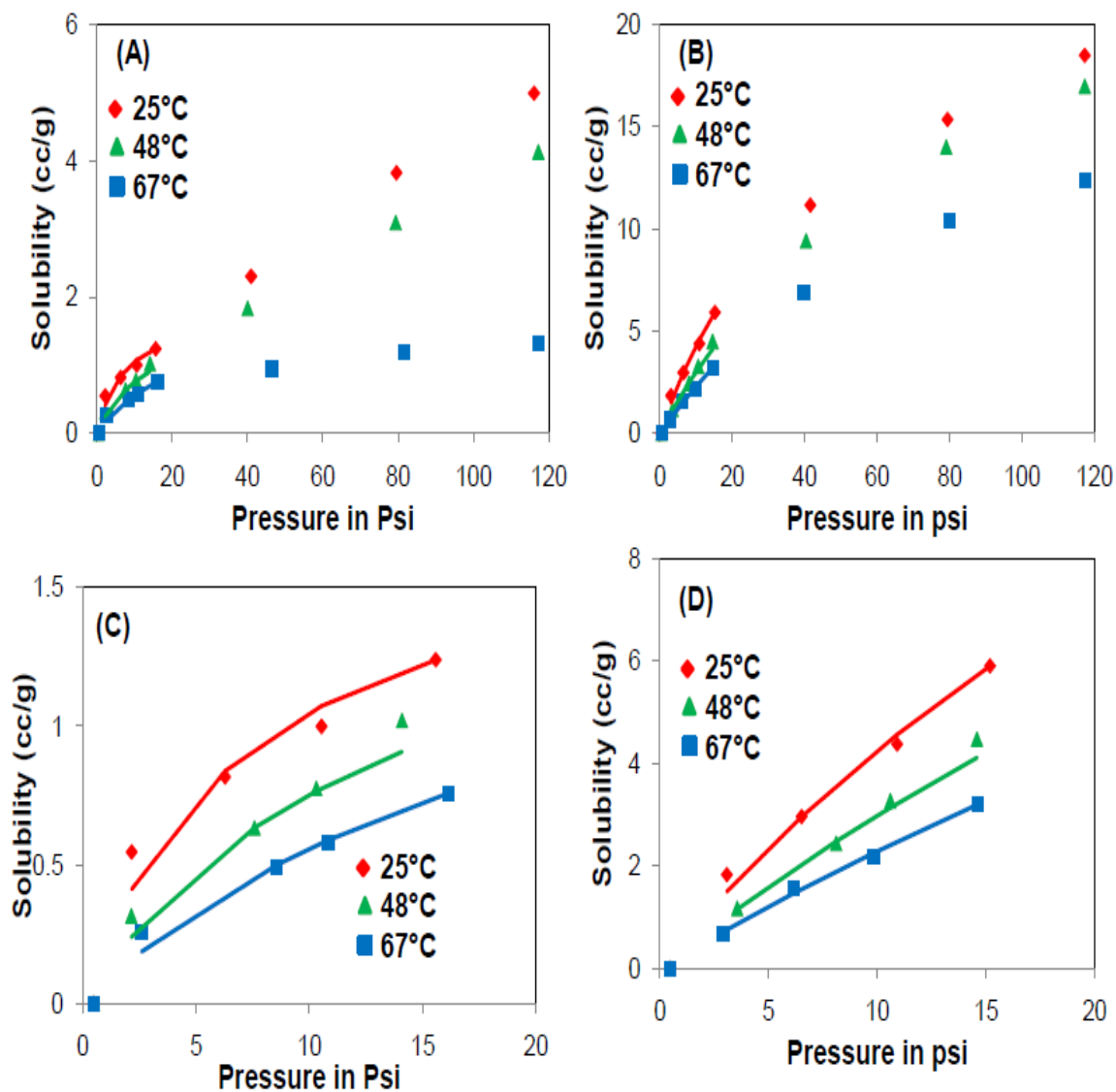


Figure 4.18 Solubility of CH₄ (in cc STP/g) at 25°C, 48°C and 67°C in the ANTs (A & C) and Bare AlSi NTs (B & D). Adsorption isotherms for the entire pressure range (0-120 psi) presented in (A & B) and the sub-atmospheric pressure range (C & D), respectively. Langmuir adsorption model is fitted in the sub-atmospheric pressure range as represented by the solid lines (C & D).

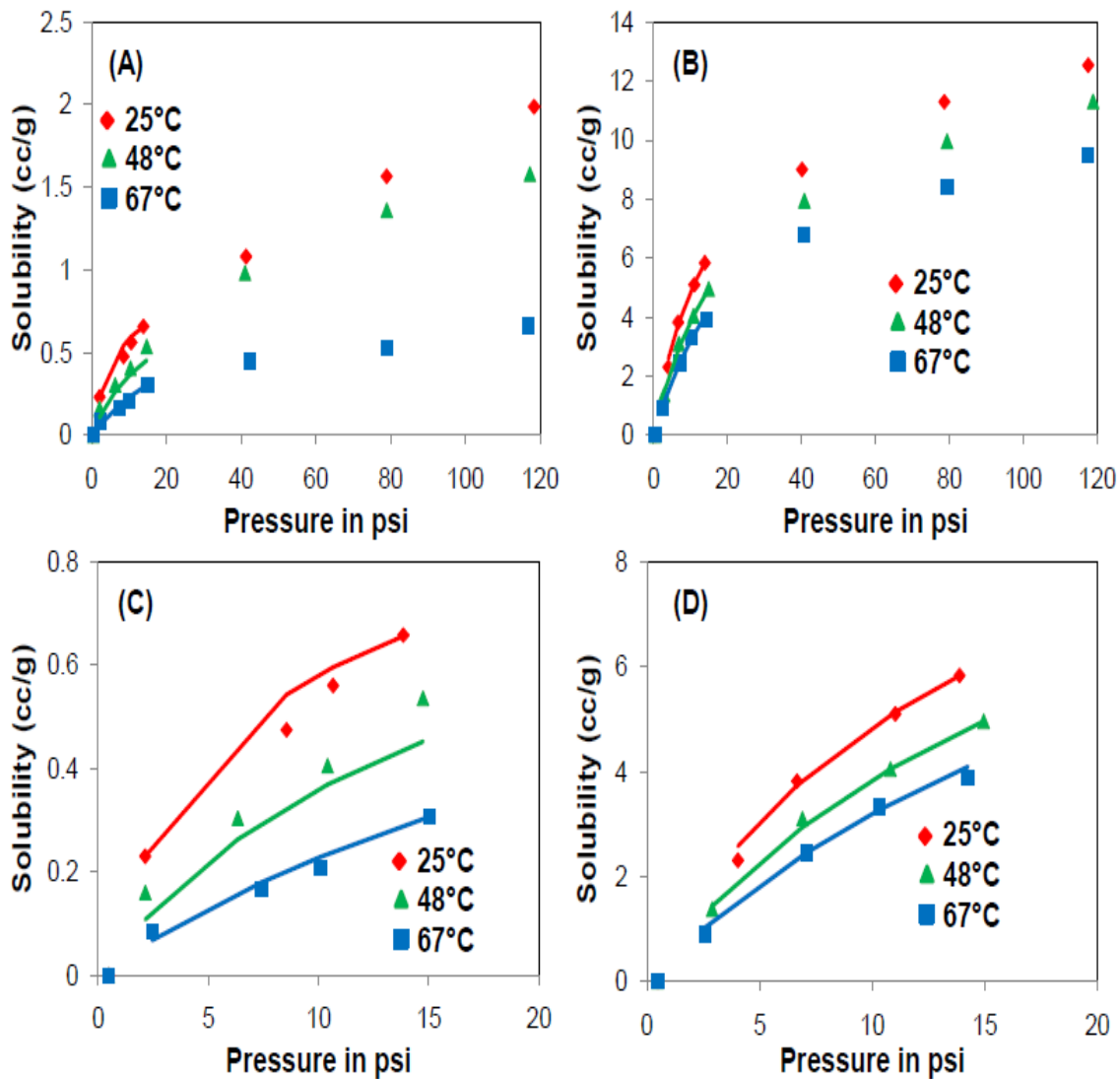


Figure 4.19 Solubility of N₂ (in cc STP/g) at 25°C, 48°C and 67°C in the ANTs (**A & C**) and Bare AlSi NTs (**B & D**). Adsorption isotherms for the entire pressure range (0-120 psi) presented in (**A & B**) and the sub-atmospheric pressure range (**C & D**), respectively. Langmuir adsorption model is fitted in the sub-atmospheric pressure range as represented by the solid lines (**C & D**).

Table 4.9 Comparison of Langmuir adsorption model parameters between BNT's and ANT's for the sub-atmospheric pressure range

Gas		C_H (cc/g)	α_0 (psi ⁻¹)	Δh_a (kJmol ⁻¹)
CO₂	Bare	22.56 ± 1.06	(1.96 ± 0.09) x10 ⁻⁴	-12.61 ± 0.6
	Amine	10.55 ± 0.75	(11.44 ± 0.81)x10 ⁻⁵	-13.75 ± 0.98
CH₄	Bare	23.7 ± 1.04	(7.3 ± 0.32)x10 ⁻⁵	-14.11 ± 0.62
	Amine	1.83 ± 0.16	(1.8 ± 0.15)x10 ⁻⁵	-22.07 ± 0.18
N₂	Bare	12.03 ± 0.45	(4.62 ± 0.17)x10 ⁻⁴	-12.34 ± 0.46
	Amine	0.99 ± 0.11	(5.61 ± 0.61)x10 ⁻⁷	-30.79 ± 3.33

Table 4.10 Average relative error (ARE in %) between the Langmuir adsorption model and the experimental data

Gas		25°C	48°C	67°C
CO₂	Bare	4.7 ± 5.6	0.6 ± 0.5	8.7 ± 11.8
	Amine	1.4 ± 1.9	13.8 ± 7.1	6.2 ± 9.8
CH₄	Bare	5.6 ± 8.6	3.8 ± 3.2	3.7 ± 2.5
	Amine	8.7 ± 11	9.2 ± 11.2	7.7 ± 13.2
N₂	Bare	3.7 ± 5.5	2.4 ± 2.7	5.1 ± 6.1
	Amine	5.2 ± 6.7	17.7 ± 10.3	9.5 ± 8

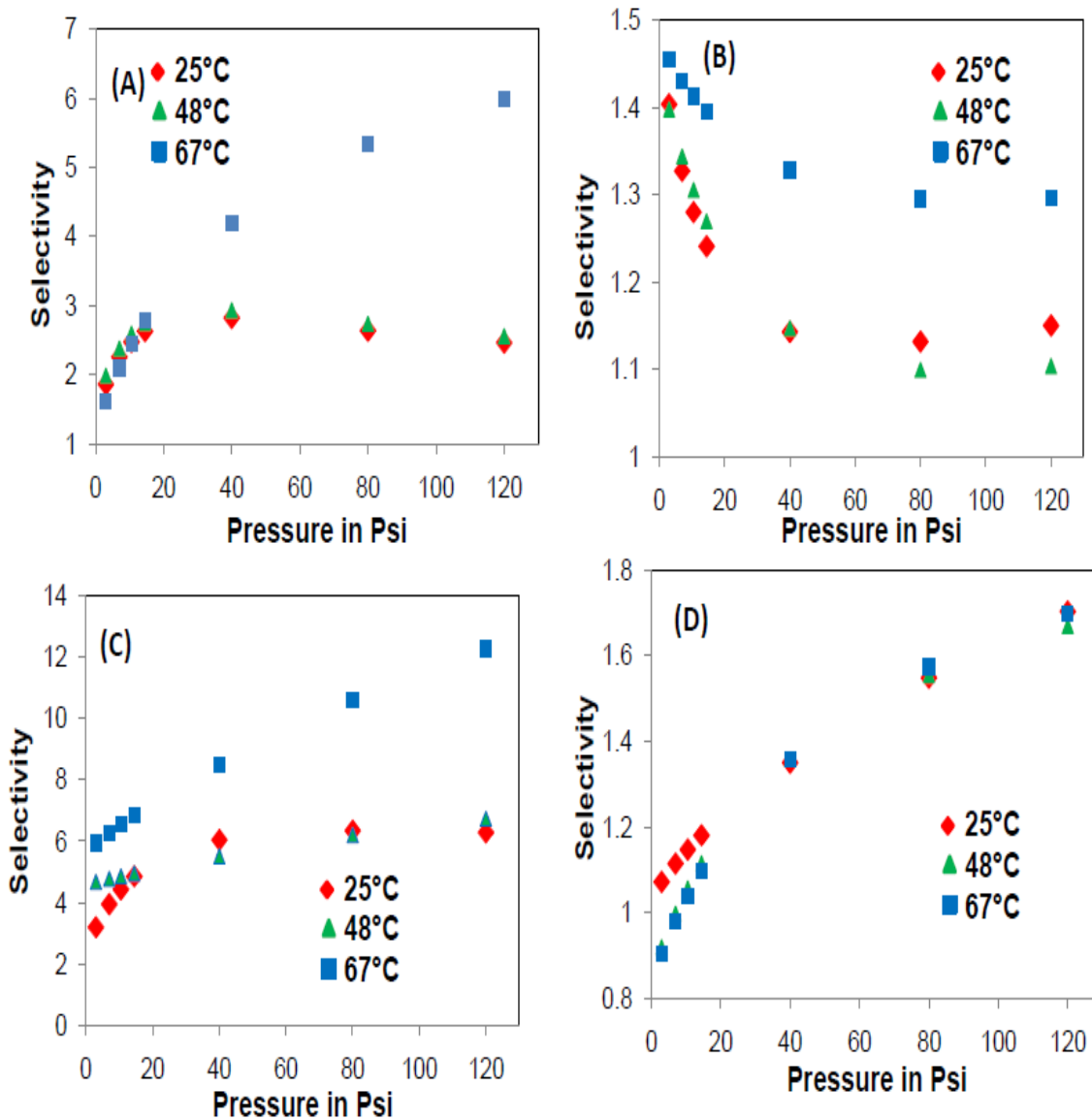


Figure 4.20 Comparison of adsorption selectivity between BNTs and ANTs at different temperatures. (A) CO₂/CH₄ adsorption selectivity for ANTs, (B) CO₂/CH₄ adsorption selectivity for BNTs, (C) CO₂/N₂ adsorption selectivity for ANTs, (D) CO₂/N₂ adsorption selectivity for BNTs

Table 4.11 Henry's constant ratio between ANT and BNT (K_{ANT}/K_{BNT}) for three adsorbates.

T (°C)	CO ₂	CH ₄	N ₂
25°C	0.41	0.18	0.08
67°C	0.36	0.34	0.07

Table 4.12 Fitted Langmuir parameters of the gas adsorption isotherms. The product of C_i and α is the Henry's constant K

		CO ₂		CH ₄		N ₂	
		25°C	67°C	25°C	67°C	25°C	67°C
NT	C_H (cm ³ /g STP)	28.7	25.4	26.8	20.9	14.4	11.5
	α (1/psi)	0.02	0.014	0.018	0.012	0.048	0.037
	K_H (cc/g.psi)	0.574	0.356	0.482	0.251	0.691	0.426
ANT	C_H (cm ³ /g STP)	21.4	16.46	9.5	1.42	2.6	0.76
	α (1/psi)	0.011	0.0078	0.0089	0.06	0.022	0.038
	K_H (cc/g.psi)	0.235	0.128	0.085	0.085	0.057	0.029

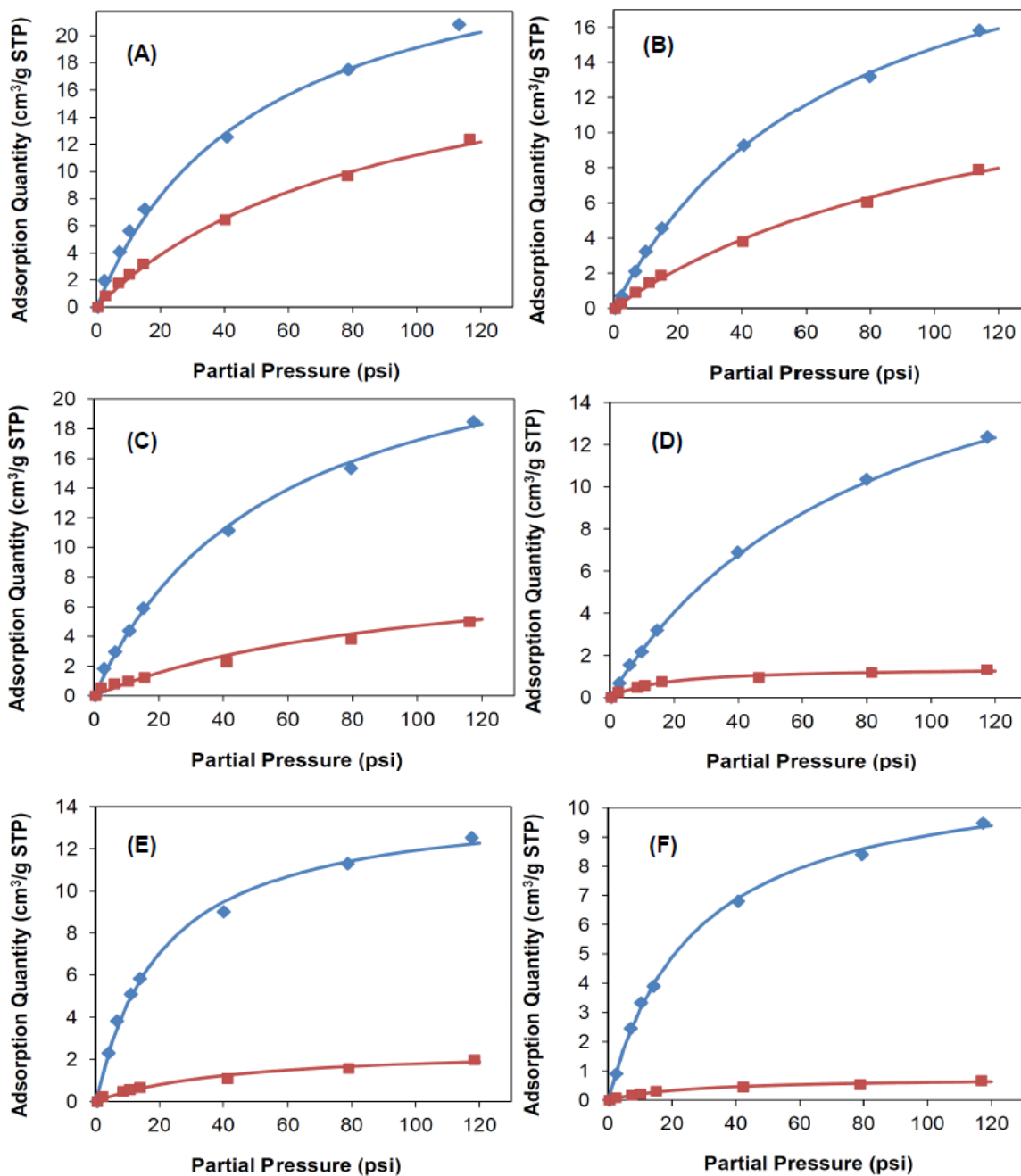


Figure 4.21 The adsorption isotherms of (A) CO₂ at 25 °C, (B) CO₂ at 67 °C, (C) CH₄ at 25 °C, (D) CH₄ at 67 °C, (E) N₂ at 25 °C, and (F) N₂ at 67 °C for BNTs (blue diamonds) and ANTs (red squares); and the fitted curves (solid lines) of the Langmuir model.

4.7 Conclusions

In this chapter, the gas adsorption measurements in nanoporous materials are presented. The nanoporous materials studied include MOFs such as Cu-hfipbb and ZIF-90 and metal oxide nanotubes such as single walled aluminosilicate nanotubes whose inner pore have been partially functionalized with methyl amine molecule. Gas adsorption measurements from Cu-hfipbb MOF were fit with simple Langmuir model to yield thermodynamic adsorption parameters such as heat of adsorption and adsorption capacity. From the parameters, it was clear that the adsorption favorability followed the order $\text{CO}_2 > \text{CH}_4 > \text{N}_2$. Following the adsorption measurement with Cu-hfipbb, the adsorption of CO_2 , CH_4 and N_2 in ZIF-90 was examined at different temperatures. Given the pore structure of ZIF-90 and the kinetic diameter of the gases tested, it was inferred that Langmuir model is not applicable. Hence the sub-atmospheric pressure data was fitted with Henry's model, and the adsorption favorability based on Henry's law followed the order $\text{CO}_2 > \text{CH}_4 > \text{N}_2$. Since the Cu-hfipbb was identified to have high diffusion selectivity (CO_2/CH_4) based on a computational study and earlier study with smaller crystals did not yield satisfactory results, larger crystals of Cu-hfipbb were synthesized and the gas adsorption isotherms with CO_2 , CH_4 , N_2 , Ethylene and n-Butane were collected. The CH_4 , N_2 and n-Butane isotherms were fit with Langmuir isotherm while CO_2 and Ethylene were fit with Dual mode isotherms to account for interstitial space filling in addition to the pore filling accounted by Langmuir model. From the parameters it was observed that the adsorption favorability followed the order n-Butane $>$ $\text{CO}_2 >$ Ethylene $>$ $\text{CH}_4 >$ N_2 . Subsequently the gas adsorption measurements from AlSiNTs are presented. For comparison the adsorption measurements from BNTs are presented followed by that

from ANTs. From the measurements it is clear that partial functionalization of the BNTs has improved the selectivity (four fold for CO₂/CH₄ and ten fold for CO₂/N₂) appreciably. Further the adsorption favorability follows the order CO₂ > CH₄ > N₂. Thus the gas adsorption setup is capable of providing reliable measure of thermodynamic adsorption parameters from novel nanoporous materials.

CHAPTER 5: APPLICATIONS TO DIFFUSION MEASUREMENTS

5.1 Theory of Gas Diffusion in Thin Films

The 1-D conservation of species equation is given by

$$\frac{\partial c}{\partial t} = -\frac{\partial}{\partial x} j_x \quad (5.1)$$

Where c is the concentration of the diffusion species, t is the time, and j_x is the flux in the x-direction, which is along the thickness of a membrane and the only direction in which mass transfer is taking place. If A is the area of the face of the membrane and $A^{1/2} \gg L$, the membrane thickness, the mass transfer dynamics is one dimensional [98]. In this equation, the swelling of the polymer due to gas adsorption is assumed to be negligible.

The entire problem is converted to a boundary value problem in concentration c , which requires that the flux be related to the concentration field. The simplest way to do this is to employ Fick's law,

$$j_x = -D \frac{\partial c}{\partial x} \quad (5.2)$$

Combining equation 5.1 and 5.2, we have

$$\frac{\partial c}{\partial t} = \frac{\partial}{\partial x} \left(D \frac{\partial c}{\partial x} \right) \quad (5.3)$$

This equation can then be solved subject to appropriate initial and boundary conditions to obtain an explicit equation for diffusion coefficient D , following which the theory and experiments can be compared to obtain the value of D [98].

In our experiments, the sample is deposited on a flat substrate and is suspended in vacuum. A gas is then introduced and maintained at constant pressure. The gas molecules

diffuse through the membrane and the mass uptake is measured by the QCM. The data are reported as the fractional uptake (with respect to the equilibrium value) as a function of time. For constant diffusion coefficient D , the solution to equation 5.3 leads to

$$\frac{M_t}{M_\infty} = 1 - \frac{8}{\pi^2} \sum_{n=0}^{\infty} \frac{1}{(2n+1)^2} \exp\left(-\frac{D(2n+1)^2 \pi^2 t}{L^2}\right) \quad (5.4)$$

Where M_t and M_∞ are the mass uptakes at time t and at infinite time (i.e at equilibrium) and L is the membrane thickness. The integer n refers to the number of terms in the summation in equation 5.4. In our fitting, n was taken to be 50 after initial convergence studies.

Following the gas uptake measurements with thin film samples, the permeability can be calculated using equation 5.5.

$$P = D \times S \quad (5.5)$$

where D is the Diffusion coefficient in cm^2s^{-1} and S is the solubility coefficient obtained by dividing the equilibrium adsorption by the corresponding pressure expressed in cm of Hg. The gas permeability is measured in units of Barrer ($1 \text{ Barrer} = 10^{-10} \text{ cm}^3 \text{ (STP) cm cm}^{-2}\text{s}^{-1}\text{cmHg}^{-1}$ [59]).

5.2 Gas Diffusion Measurements in Matrimid 5218

5.2.1 Sample Preparation of Matrimid 5218 film Deposited on the QCM

Since the adsorption and diffusion analysis were done on the same samples, the sample deposition, annealing and degassing procedure are the same as mentioned before in Section 3.3.2.

5.2.2 Gas Diffusion Analysis in Matrimid 5218

Since the adsorption and diffusion analysis were done on the same samples, the annealing and degassing procedure are the same as mentioned before in section 3.3.2. From the transient uptake curves, the Fickian diffusion coefficient (D) was obtained by fitting equation 5.4 to the transient adsorption data by the method of least squares error. The quality of fit was ascertained both in terms of average relative error measured between the model and the transient and also by visual means. Figure 5.1 shows a typical fit between the experimental transient and the model for the Matrimid 5218 thin film sample. From the plot we can understand that the quality of fit is satisfactory. Further Figure 5.2 A & B shows the diffusion coefficients for CO_2 and CH_4 in Matrimid at different pressures and temperatures. It should be noted that while adsorption data from Matrimid 5218 film were presented at temperatures 30°C , 35°C and 45°C (section 3.4.2), diffusion data at 30°C was observed to be noisy and hence only data at 35°C and 45°C are presented. From the Figure we observe that the diffusion coefficients for CO_2 to be approximately an order of magnitude above that of CH_4 (due to kinetic effects which is governed by the kinetic diameters K_d ($K_{d\text{CO}_2} < K_{d\text{CH}_4}$)) and that it does not have much variation across different pressures at each temperature. Hence we have used the average diffusion coefficient with the appropriate error bars to calculate the permeability using equation 5.5 in Figure 5.2 C.

It should be noted that while collecting the gas adsorption isotherm, the equilibrium pressure points at different temperatures varied slightly, and hence the adsorption isotherms were fitted with individual dual mode isotherms and then re-plotted

to obtain adsorption data at specific pressures. This maintains ease of comparison of permeation data with the literature.

Figure 5.3 A & B shows the permeation in Barrers for CO₂ and CH₄ in Matrimid at different pressures and temperatures along with the error bars obtained from Figure 5.2C and is compared against the literature [59]. From the plot we note that at an equilibrium pressure of 2 atm (as available in the literature [59]), the permeation data for CO₂ and CH₄ at 35°C and 45°C have a strong agreement, thus demonstrating the capability of the current setup to measure the adsorption and diffusion characteristics simultaneously. Further from Figure 5.3, we also observe that there is a smooth downward trend in permeability with increase in pressure, which is due to the solubility of the gas normalized with respect to pressure. The permeability of CO₂ and CH₄ increase with temperature following the trend with diffusion coefficients.

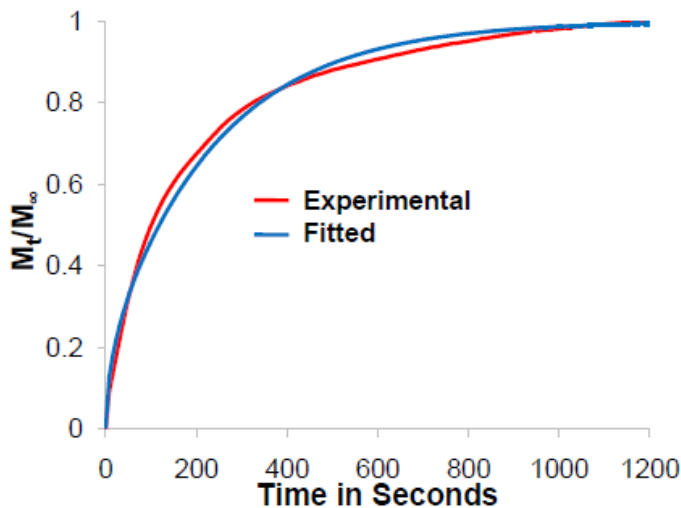


Figure 5.1 Typical fit of the experimental transient data with fitted equation (equation 5.4) for Matrimid 5218.

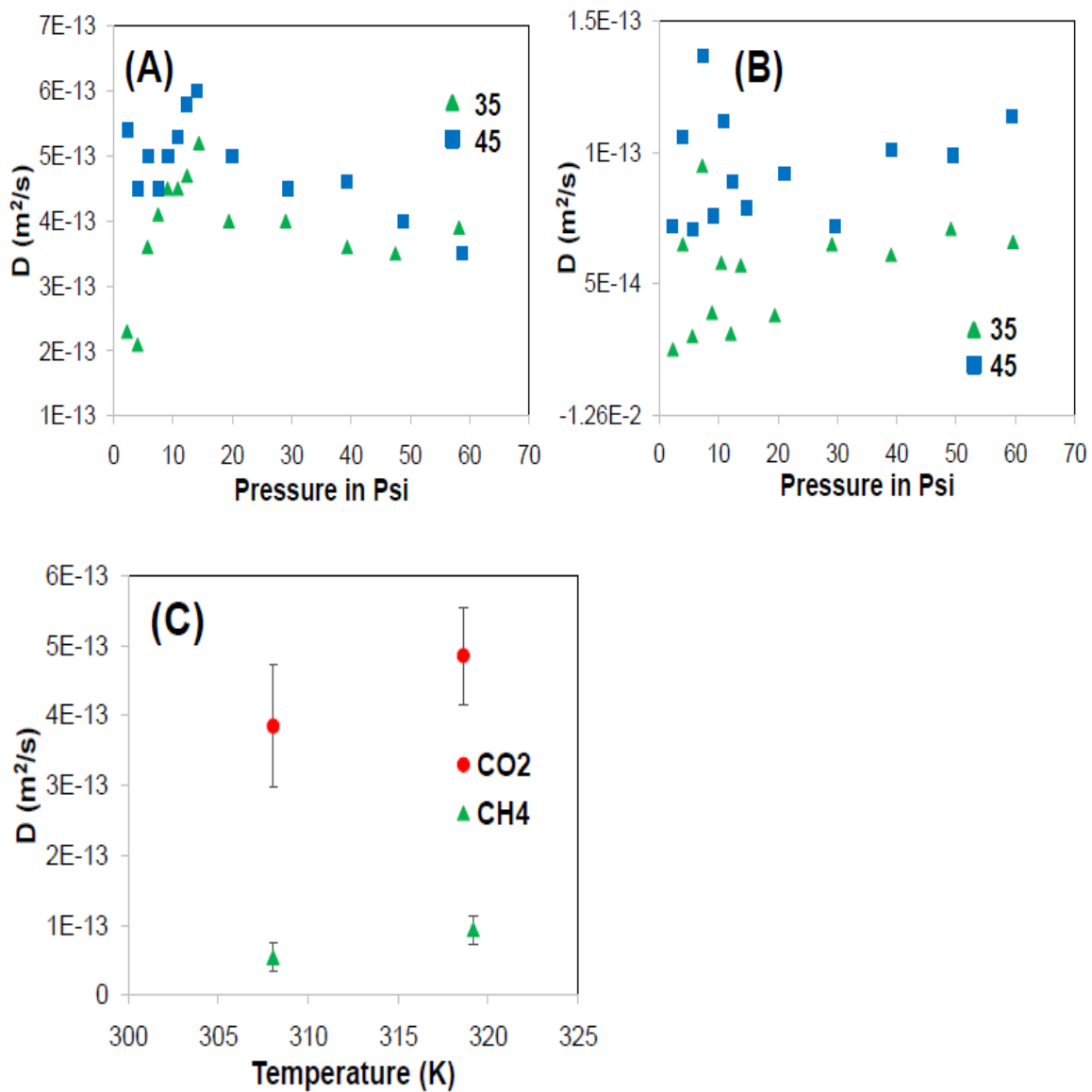


Figure 5.2 Gas diffusion coefficients vs pressure at different temperatures in Matrimid 5218 for (A) CO₂ and (B) CH₄, (C) Average gas diffusion coefficients (based on all pressures) at different temperatures.

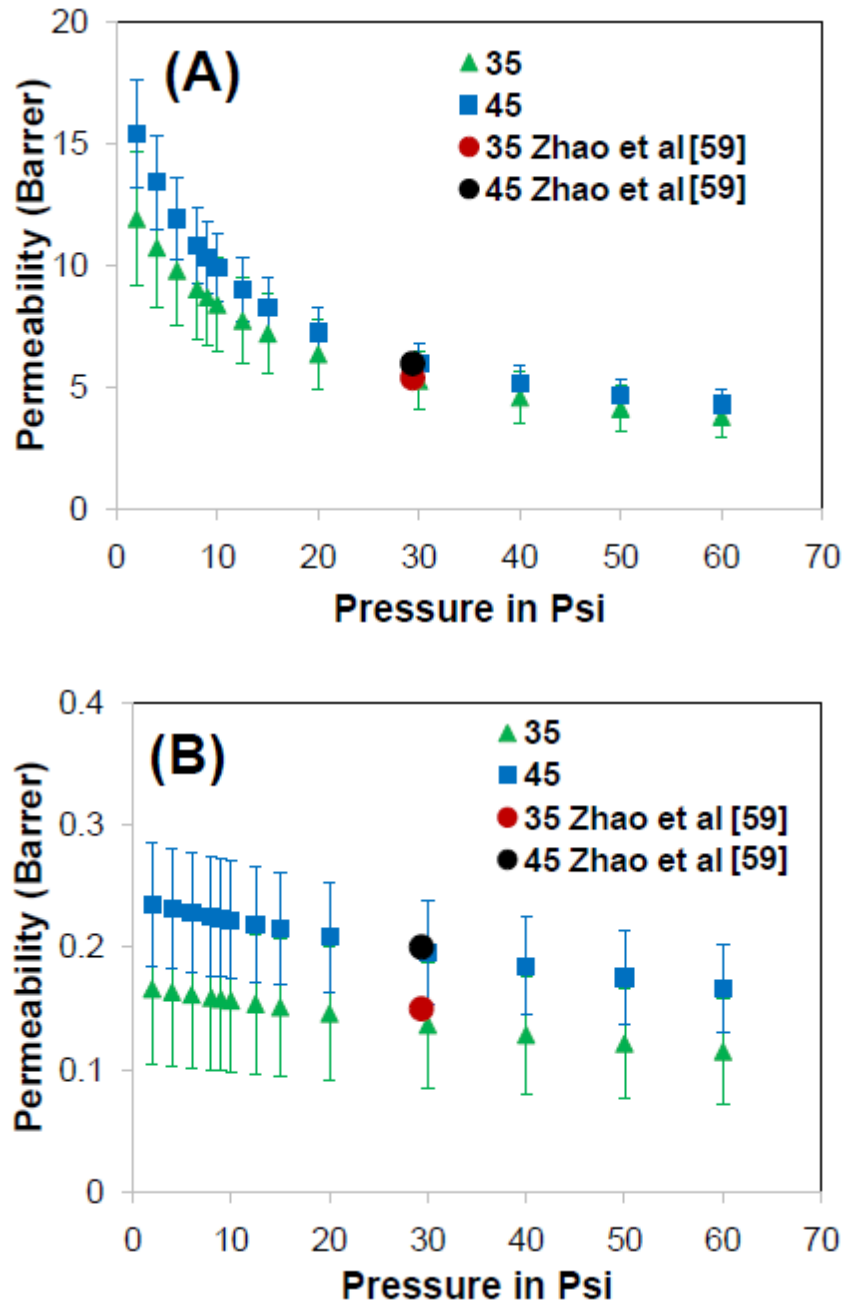


Figure 5.3 Permeability of gases in Matrimid 5218 at different temperatures compared with literature data [59] (A) CO₂ permeability (B) CH₄ permeability

5.3 Gas Diffusion Measurements in 6FDA-DAM

5.3.1 Sample Preparation, Deposition and Characterization of 6FDA-DAM film Deposited on the QCM

The sample deposition, annealing and degassing procedures are the same as mentioned in section 3.5.1.

5.3.2 Gas Diffusion Analysis in 6FDA-DAM

Since the adsorption and diffusion analysis were done on the same samples, the annealing and degassing procedure are the same as mentioned before in section 3.5.1. From the transient uptake curves, the Fickian diffusion coefficient (D) was obtained by fitting equation 5.4 to the transient adsorption data by the method of least squares error. The quality of fit was ascertained both in terms of average relative error measured between the model and the transient and also by visual means. Figure 5.4 shows a typical fit between the experimental transient and the model for the 6FDA-DAM thin film sample. From the plot we can understand that the quality of fit is satisfactory.

By using the above mentioned method of fit for CO₂, CH₄ and n-C₄H₁₀ gas uptake in 6FDA-DAM, we observed that for CO₂ and CH₄, the diffusion coefficients so obtained were not reliable because the gas uptake transients were too fast to be measured by the setup. This may be essentially limited by external mass transfer effects and the current electrical instrumentation to measure resonant frequency. However for n-C₄H₁₀, the uptake was slow enough to obtain reliable parameters. Figure 5.5A shows the gas diffusion coefficients at different temperatures for n-Butane in 6FDA-DAM. From the plot we observe that the diffusion coefficients generally decrease with increasing

pressure, although at lower pressures (< 5 psi), the diffusion coefficients increase with increasing pressure and decreasing temperature. This is most likely due to the void filling action (Langmuir mode) at low pressures. Above 5 psi, the adsorption regime changes from Langmuir to Henry's mode (linear relation to pressure) which may result in lesser availability of void spaces. Further, the diffusion and solubility coefficients (equation 5.5) were used to calculate the permeability and compared with the literature [61] in Figure 5.5B. From the plot we observe that the measured permeability data agrees well with the literature and the trends are consistent with that of diffusion coefficients. The highlight of this study with polymer materials was the establishment of the capability of the QCM based sorption cell to measure diffusion coefficients and investigation of diffusion properties of candidate polymer materials with respect to pressure and temperature.

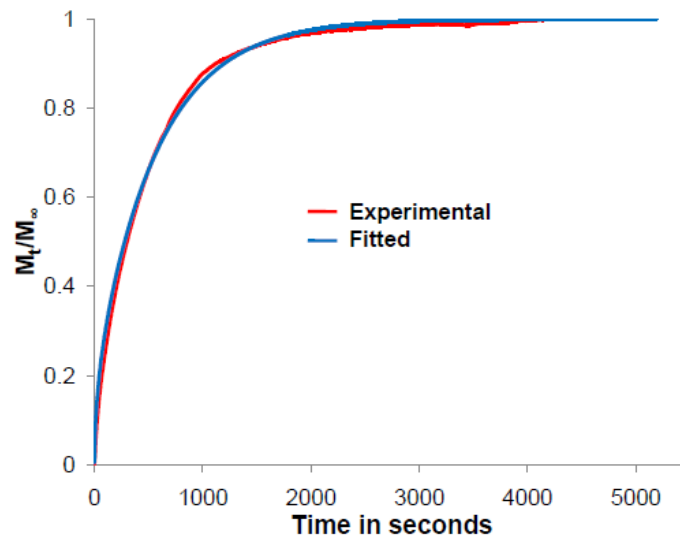


Figure 5.4 Typical fit of the experimental transient data with the fitted equation (equation 5.4) for 6FDA-DAM

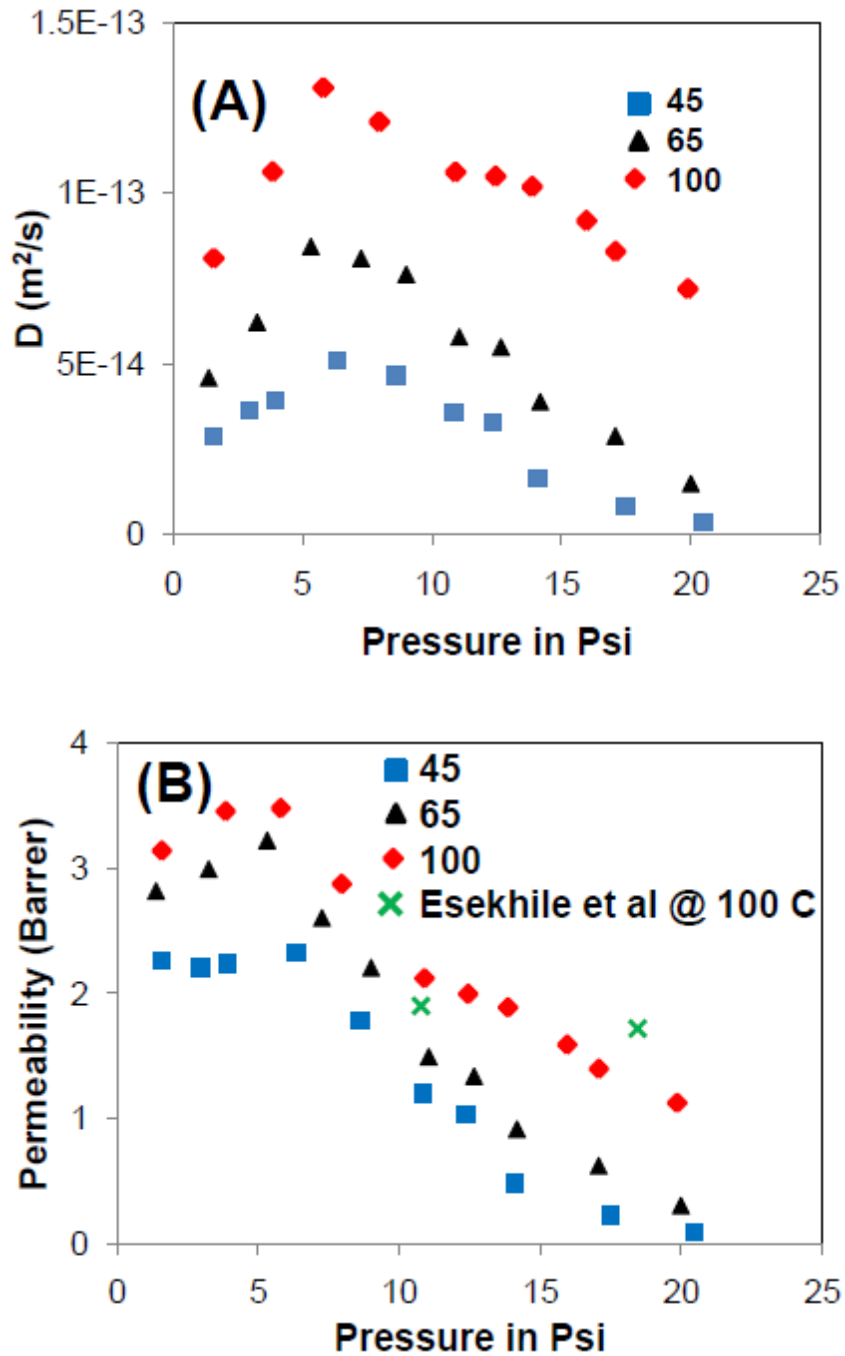


Figure 5.5 (A) Gas diffusion coefficients vs pressure at different temperatures for n-Butane in 6FDA-DAM, (B) Permeability of n-Butane in 6FDA-DAM at different temperatures compared with literature data.

5.4 Theory of Diffusion in a Porous Solid Particles

The governing equation for micropore diffusion in an isothermal adsorbent particle of roughly spherical shape may be written in the form

$$\frac{\partial c}{\partial t} = \frac{1}{r^2} \frac{\partial}{\partial r} \left(r^2 D \frac{\partial c}{\partial r} \right) \quad (5.6)$$

For a step change in concentration at time zero the relevant initial and boundary conditions are:

$$t < 0, c = c_0 \quad (5.7)$$

$$t \geq 0, c = c_\infty \quad (5.8)$$

$$t \rightarrow \infty, c = c_\infty \quad (5.9)$$

$$\frac{\partial c}{\partial r} \Big|_{r=0} = 0 \text{ for all } t \quad (5.10)$$

And we obtain the familiar solution for the transient sorption curve [99]:

$$\frac{M_t}{M_\infty} = 1 - \frac{6}{\pi^2} \sum_{n=1}^{\infty} \frac{1}{n^2} \exp\left(-\frac{n^2 \pi^2 D t}{r^2}\right) \quad (5.11)$$

where the c is the concentration of the diffusion species, D is the diffusion coefficient, t is the time and r is the particle or crystal radius. The integer n refers to the number of terms in the discrete function in equation 5.11. In our fitting, n was taken to be 50 after initial convergence studies. It should be noted that the adsorbent particles used in our studies are not uniform spheres and in such cases it is common practice to replace the spherical particle radius (r) with an equivalent spherical radius r_c , which is defined as the radius of the sphere having the same external surface area to volume ratio. In our case since the size of the particle deposited on the QCM varies, we opted to replace the r^2/D with the diffusion time constant τ .

5.5 Gas Diffusion Measurements in MOFs

5.5.1 Sample Preparation, Deposition and Characterization of Cu-hfipbb Crystals (small and large crystals) Deposited on the QCM

Since the adsorption and diffusion analysis were done on the same samples, the sample deposition, annealing and degassing procedure are the same as mentioned before in sections 4.3.1 (small crystals) and 4.3.3 (large crystals).

5.5.2 Gas Diffusion Analysis in Cu-hfipbb Crystals (small and large crystals)

Since the adsorption and diffusion analysis were done on the same samples, the degassing procedure is the same as mentioned before in sections 4.3.3. The primary reason for experimentally understanding diffusion behavior in Cu-hfipbb was due to a computational study by Watanabe et al. [19] in which the CO₂/ CH₄ selectivity was computed to be about 10⁴-10⁵ for membrane based application. From the transient uptake curves, the Fickian diffusion coefficient (D) was obtained by fitting equation 5.11 to the transient adsorption data by the method of least squares error. The quality of fit was ascertained in terms of average relative error measured between the model and the transient curve and is plotted as error bars in Figure 5.6. From the plot we can understand that the quality of fit is satisfactory.

By using the above mentioned method of fit for CO₂, CH₄, N₂, Ethylene and n-C₄H₁₀ gas uptake in Cu-hfipbb MOF, we observed that for CO₂, the diffusion time constants so obtained were not reliable because the gas uptake transients were too fast to be measured by the setup. The gas diffusion time scales so obtained for CO₂ are presented in Figure 5.6 A. From the Figure we observe that the gas uptake reaches ~

90 % of the equilibrium adsorption within the first 5-10 seconds. Based on the frequency of the data acquisition in the current setup, this corresponds to about 1-2 data points. Therefore we can infer that there is not sufficient number of datapoints to obtain dependable diffusion time constant. Hence the diffusion time constants obtained for CO₂ in Cu-hfipbb MOF were considered unreliable. However for CH₄, N₂, Ethylene and n-C₄H₁₀, the uptake was slow enough to obtain reliable parameters. An example of the typical plot obtained for other gases (CH₄, N₂, Ethylene and n-C₄H₁₀) in Cu-hfipbb MOF is shown in Figure 5.6 B. From the plot we observe that there is sufficient number of data points until equilibrium adsorption to obtain reliable diffusion time constant.

Figure 5.7A-D shows the gas diffusion time constants at different temperatures for CH₄, N₂, Ethylene and n-Butane in Cu-hfipbb MOF. From the plots we observe that CH₄ and N₂ had a fast uptake with the time constant around 1000-2000 sec. Even though the gas uptake of CO₂ was fast, a rough estimate of the diffusion time scale was obtained and it was found to be around 10 seconds. Thus through our setup only a lower bound diffusion selectivity (CO₂/CH₄ and CO₂/N₂) can be estimated and was found to be about ~ 100-200. Also between CH₄ and N₂ there was not much differences in the diffusion time scale. On the other hand, Ethylene and n-Butane showed large differences in diffusivity, with n-Butane diffusing much slower than Ethylene (which is faster than methane). The diffusion selectivity of Ethylene over n-Butane is presented in Figure 5.8 and from the plot we observe that the selectivity is initially high and then decreases with increase in pressure due to saturation of the adsorption isotherm at higher pressures. Thus we are able to observe strong evidence of size selective separation. One constant trend in all these measurements is that at higher pressures (> 20psi), the time constants and hence

fickian diffusivities become almost constant due to saturation of pores as evidenced by the adsorption isotherm.

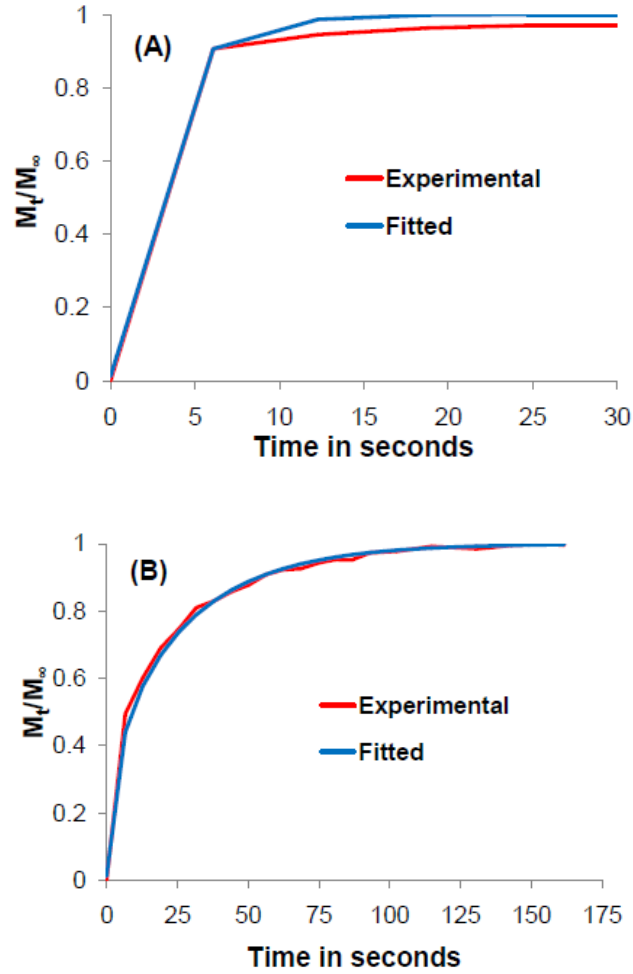


Figure 5.6 (A) Typical fit of the experimental transient data with the fitted equation (equation 5.11) for CO₂ in Cu-hfipbb MOF, (B) Typical fit of the experimental transient data with the fitted equation (equation 5.11) for other gases in Cu-hfipbb MOF

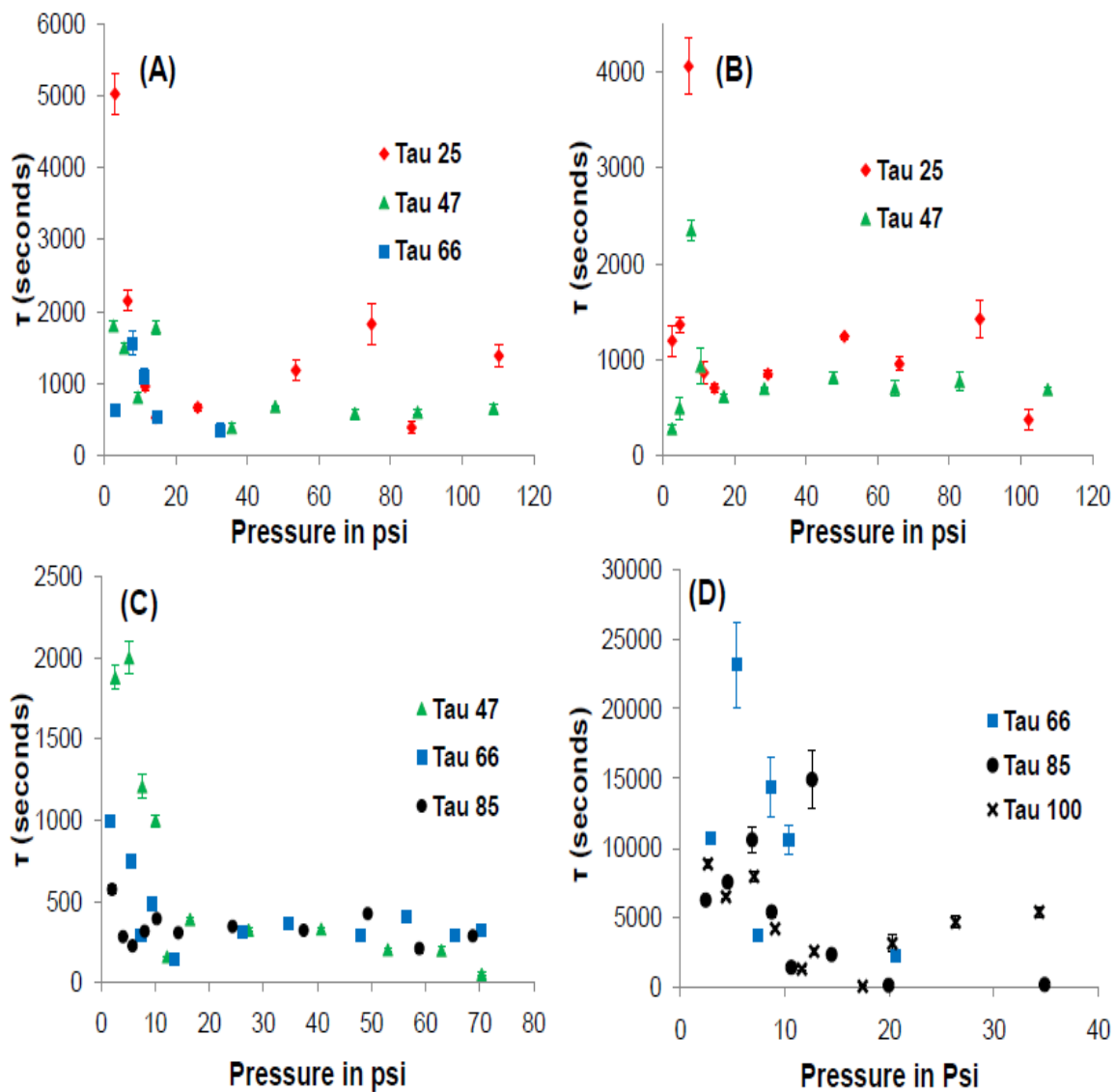


Figure 5.7 Gas diffusion time scale vs pressure at different temperatures in Cu-hfipbb for
(A) CH₄, **(B)** N₂, **(C)** Ethylene and **(D)** n-Butane

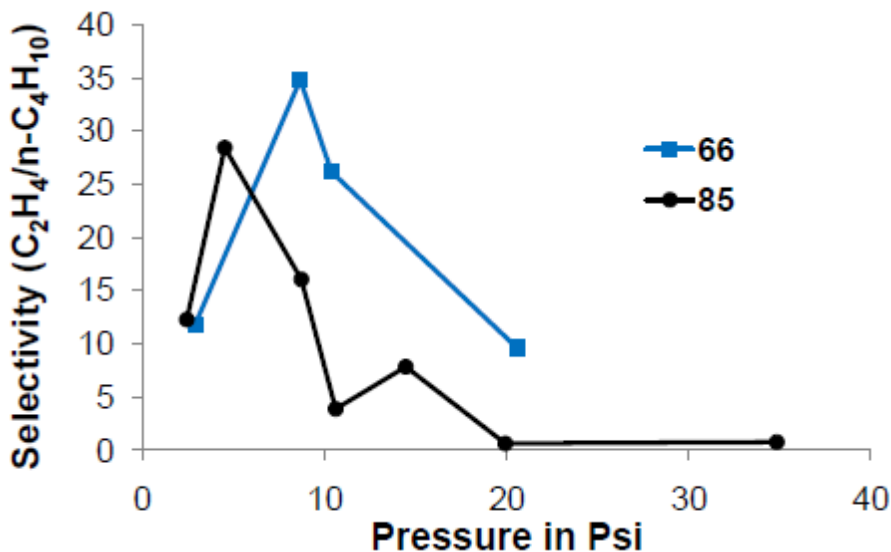


Figure 5.8 Diffusion selectivity of ethylene over n-Butane in Cu-hfipbb MOF. The lines connecting the points are only a guide to the eye.

Further comparison with diffusion time scale obtained from small crystals of Cu-hfipbb MOF (Section 4.3.1) was performed. As in the case of large sized Cu-hfipbb crystals, the adsorption and diffusion analysis were done on the same samples and the degassing procedure is the same as mentioned before in sections 4.3.1. From our comparison in Figure 5.9, we observe that as in the case of large sized crystals, the diffusion time scale of CO₂ obtained from small sized crystals is not reliable due to fast transients. However the diffusion time scale obtained for CH₄ in the small sized crystals follows the trend and magnitude of the diffusion time scale comparable to that from the large sized crystals. In conclusion, this study showed that qualitative trends could be discerned from the data, although quantitatively the data is not as good as the polymeric materials which may be the result of sample non-uniformity of the Cu-hfipbb MOF material. While further investigation of the above issues is a topic of future work, initial

studies showed that the technique is at least suitable for screening of materials with small amounts of sample before detailed measurements.

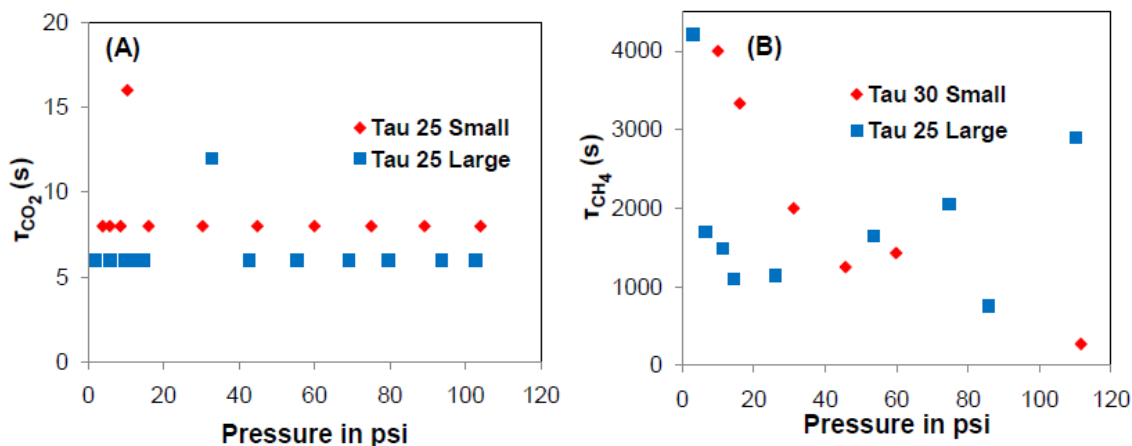


Figure 5.9 Comparison of diffusion time scale obtained from large and small sized Cu-hfipbb crystals for (A) CO₂ and (B) CH₄

5.6 Conclusions

In this chapter we have investigated the measurement of diffusion coefficients in polymeric and microporous materials using the controlled-environment QCM apparatus. By fitting the transient uptake (resonant frequency) curves with the equation for transient diffusion into a thin film, the diffusion coefficients were obtained for CO₂ and CH₄ in Matrimid 5218. On comparing the obtained diffusion coefficient with that in the literature, a strong agreement was found. Further to test the limits of data acquisition and to study another candidate membrane material, gas diffusion experiments with 6FDA-DAM were performed with CO₂, CH₄ and n-Butane. From analysis, it was found that the diffusion coefficients obtained for CO₂ and CH₄ were not reliable possibly due to external mass transfer effects or due to low data acquisition frequency of the current

electrical instrumentation. However, further experiments with n-Butane yielded reliable diffusion coefficients in strong agreement with the literature. Thus it was inferred that the setup was currently capable of measuring diffusion coefficients of species in an appropriate range of diffusivities, and modifications to the setup was necessary to study fast diffusing species. Following our studies with polymeric materials, we also studied the MOF, Cu-hfipbb. The Cu-hfipbb MOF was found to have a diffusion selectivity (CO_2/CH_4) of 10^4 - 10^5 based on a computational study. From experimental gas uptake measurements, it was found that barring CO_2 all the other gases (CH_4 , N_2 , Ethylene and n-Butane) yielded reliable estimates the diffusion time scale and the lower bound diffusion selectivity (CO_2/CH_4 & CO_2/N_2) was approximately 10^2 . Also between CH_4 and N_2 there was not much differences in the diffusion time scale. On the other hand, Ethylene and n-Butane showed large differences in diffusivity, with n-Butane diffusing much slower than Ethylene. In conclusion, this study showed that qualitative trends could be discerned from the data, although quantitatively the data is not as good as the polymeric materials which may be the result of sample non-uniformity of the Cu-hfipbb MOF material. While further investigation of the above issues is a topic of future work, initial studies showed that the technique is atleast suitable for screening of materials with small amounts of sample before detailed measurements.

CHAPTER 6: CONCLUSIONS AND RECOMMENDATIONS FOR FUTURE WORK

6.1 Conclusions

Nanoporous materials like metal organic frameworks and metal oxide nanotubes are rapidly developing classes of materials with immense potential in the areas of molecular separation, catalysis, and sensing, among many others. Experimental knowledge of the adsorption characteristics of these materials are a critical component in their progress in gas separation applications. In this thesis, the development and application of a controlled-pressure and controlled-temperature QCM-based system for adsorption measurements in nanoporous materials is presented, and its use has been demonstrated by studying gas adsorption in two important small-pore MOF materials widely considered for separation applications. The apparatus was first validated by gas adsorption measurements of a polyimide material, Matrimid 5218. Following which, detailed CO₂, CH₄, and N₂ adsorption studies were then carried out on the two MOF materials (Cu-hfipbb and ZIF-90). The adsorption isotherms were then fit to simple analytical models and key adsorption thermodynamic parameters were obtained. Cu-hfipbb was found to obey Langmuir adsorption behavior, consistent with its pore structure composed essentially of 1D channels without significant cage-like spaces. On the other hand, the cage-window duality present in ZIF-90 leads to large deviations from Langmuir adsorption. In both MOF materials, the order of adsorption affinity was CO₂>CH₄>N₂, reflecting the stronger polar interactions of the MOF frameworks with CO₂ molecules. The results from the present, and forthcoming, studies are also expected

to be useful in validating and parametrizing analytical and molecular (force-field) models for adsorption in MOF materials.

Following the measurements with the MOF materials, adsorption isotherms were collected from single-walled aluminosilicate nanotubes (BNTs) and single walled aminoaluminosilicate nanotubes (ANTs) with a 15% aminomethyl group substitution for the hydroxyl groups on the interior nanotube wall. Following detailed characterization to yield conclusive structural information on the ANTs at the molecular level, CO₂, CH₄, and N₂ adsorption measurements on the BNTs and ANTs have demonstrated that the interior surface properties can be significantly tailored by the incorporation of the primary amines. The modified interior surface results in dramatically enhanced CO₂/CH₄ and CO₂/N₂ ideal adsorption selectivity. In conclusion, this work elucidates the fabrication of functionalized single-walled metal-oxide nanotube materials with altered interior surface properties. Such an approach to synthesize functional nanotube materials can enable a wider range of applications for nanotubes, which have so far been inaccessible to other nanotube systems such as carbon nanotubes.

In addition to the adsorption measurements, experimental knowledge of the permeation characteristics of the nanoporous materials is also critical component for their progress in gas separation applications. Further with the development of an alternate route to synthesize nanocomposites of these porous materials in polymers, it is important to understand the adsorption and permeation characteristics of the widely used polymer materials. Hence in this thesis, the gas adsorption and permeation characteristics in two important polymer materials, namely Matrimid 5218 and 6FDA-DAM have been studied. Detailed CO₂ and CH₄ adsorption studies were carried out on Matrimid and 6FDA-DAM,

with the addition of n-C₄H₁₀ on 6FDA-DAM. The adsorption isotherms were then fit to simple analytical models and key adsorption thermodynamic parameters were obtained. Both the materials were found to obey the dual mode isotherm, consistent with the void structure due to improper arrangement of polymer chains annealed below the glass transition temperature. Further the order of adsorption strength followed CO₂ > CH₄ in Matrimid and n-C₄H₁₀ > CO₂ > CH₄ in 6FDA-DAM. Further analysis on permeation in Matrimid and 6FDA-DAM revealed that the QCM based setup is capable of measuring permeation parameters with strong agreement to the literature. Permeation analysis with 6FDA-DAM also revealed the limitations in measuring highly permeable gas species. Such limitations may be due to external mass transfer effects and electrical instrumentation used in the setup. Hence from this study, we found that the setup was capable of measuring diffusion coefficients, although there are limitations to highly permeable gas species.

Following the studies with polymeric materials, the candidate MOF, Cu-hfipbb was studied for its diffusion properties. The Cu-hfipbb MOF was found to have a diffusion selectivity (CO₂/CH₄) of 10⁴-10⁵ based on a computational study. From experimental gas uptake measurements, it was found that barring CO₂ all the other gases (CH₄, N₂, Ethylene and n-Butane) yielded reliable estimates the diffusion time scale and the lower bound diffusion selectivity (CO₂/CH₄ & CO₂/N₂) was approximately 10². Also between CH₄ and N₂ there was not much differences in the diffusion time scale. On the other hand, Ethylene and n-Butane showed large differences in diffusivity, with n-Butane diffusing much slower than Ethylene. In conclusion, this study showed that qualitative trends could be discerned from the data, although quantitatively the data is not as good as

the polymeric materials which may be the result of sample non-uniformity of the Cu-hfipbb MOF material. While further investigation of the above issues is a topic of future work, initial studies showed that the technique is at least suitable for screening of materials with small amounts of sample before detailed measurements.

In summary, the QCM-based adsorption and permeation measurement technique is shown to be valuable in the quantitative and qualitative study of molecular recognition by nanoporous materials. Being more compact/miniaturized, microanalytical techniques such as QCM show promise for future adsorption and diffusion measurement methodologies. To conclude, this work has demonstrated a sound basis for wider application of microanalytical techniques, specifically QCM-based measurements, in fundamental research on adsorption and diffusion in porous materials.

6.2 Future work

While this thesis has conclusively proved that controlled-environment QCM based techniques show promise as a microanalytical gas adsorption and diffusion measurement methodology, there is however significant scope for improvements. Some aspects that can be improved are: - (1) the electrical instrumentation and data acquisition system to increase speed of data acquisition, (2) modifying the design of the adsorption apparatus to enable multicomponent measurements and (3) developing a synchronized “multi-method” approach in conjunction with micro devices such as piezoresistive microcantilever. More detailed descriptions of the above suggested improvements are provided below.

6.2.1 Improvements to the Electrical Instrumentation and Data Acquisition System

Some of the improvements that can be made to electrical instrumentation may be replacing the IEEE GPIB interface which has a handshake mode to transfer data with the RS232 digital interface which send the digital information in parallel to the computer. Further additional frequency counter may also be used for faster data transfer. We can also use additional A/D convertor to collect damping voltage, temperature and pressure for faster and accurate data acquisition. From the microbalance perspective, a high resonant frequency QCM (resonant frequency up to 20 MHz by thinning the QCM substrate) can used to improve the mass resolution.

6.2.2 Improvements to the design for multicomponent measurements

As mentioned before, it is imperative to decrease the volume of the chamber so that the temperature gradient can be minimized and better control over the heating process can be achieved. The system of the present development can be used in a multi component gas system pending modifications. In this section, a brief description of the modified design is presented. Figure 6.1 shows an embodiment capable of detecting gas adsorption in a multicomponent-gas system, and the detail of the high pressure cell chamber is illustrated in Figure 6.2 – 6.4. Detailed and enlarged illustration of each step, including gas intake, thermocouple fitting, pressure gauge fitting, GC/MS exit gas analyzer, gas feed valve, alternative pressure gauge fitting, and exit gas analyzer are provided in Figure B1 to B7 in Appendix B. The detailed specifications of the components in these Figures are exemplary only, and can be modified as needed.

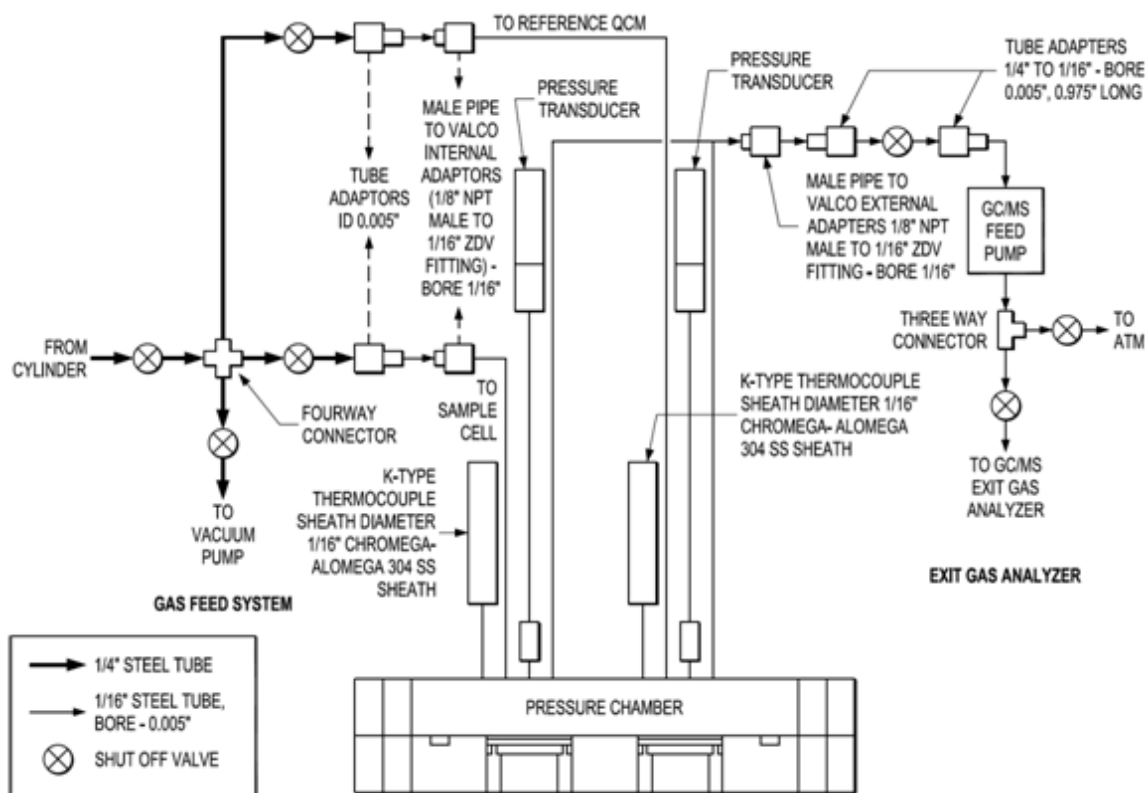


Figure 6.1 Schematic of the suggested multicomponent gas sorption apparatus.

In Figure 6.1, two 5 MHz quartz crystal microbalances can be placed inside a stainless steel high pressure chamber. The temperature and pressure of the high pressure chamber can be monitored by thermocouple and pressure transducer, respectively. One of the two quartz crystal microbalances sensor can be coated with the nanoporous material, and the other one serves as a reference QCM. This system is capable of measuring the simultaneous adsorption and desorption of several gases in a mixture.

Unlike the single gas system, the multiple gas system mentioned in this example has a smaller bulk volume above the QCM, and is connected to an exit gas analyzer system (GC/MS or infra absorption spectrum) to determine the compositional change of gas mixture from the sample cell. Since the compositional change upon

adsorption/desorption needs to be measured, and the amount of sample on the QCM crystal is very small, the total volume of the gas above the sample also must be very small in order for the compositional analysis system to be able to measure a significant change in composition.

The pressure and temperature exemplified herein ranges from a few milli-torr up to 8 bar pressure and up to 185°C respectively. However, other ranges are also contemplated and can be implemented without deviating from the spirit of the present development.

Referring to Figure 6.2, where the chamber head of the high pressure cell of the present invention is illustrated. The chamber head comprises two sets of instruments, each comprising a gas inlet for providing gas into the chamber, a thermocouple for measuring and monitoring the temperature, a gas outlet for evacuating the chamber after the measurement is completed, and a pressure gauge for measuring and monitoring the pressure inside the chamber. Referring to Figure 6.3, where the chamber bottom of the high pressure cell of the present invention is illustrated. Two quartz crystal microbalance sensors are provided. One of the quartz crystal microbalance sensors is coated with the candidate material and serves as a sample sensor. The other quartz crystal microbalance sensor is not coated and serves as a reference sensor.

Referring to Figure 6.4, which is a cross-sectional view of the chamber bottom shown in Figure 6.3 along the broken line. Assuming the air gap above and below the sample QCM to be 0.5 mm, the total sample volume to be calculated is about 0.5078 cm³, including the dead volume in the inlet valves, pressure gauges, exit gas analyzer and electrical connections. For this volume, assuming a 50:50 concentration of CO₂ and CH₄

at STP, the total mass of gas in this sample cell volume is 0.684 mg, corresponding to 22.8 μ moles. The number of moles is the mass of gas divided by the molecular weight. For a 50% mixture of CO₂ and CH₄, the average of the two molecular weights was used. The reference and sample QCM sensors are connected to a computer through SMB (sub-miniature B coaxial feed-throughs) connections to read and record the measured resonant frequencies there from.

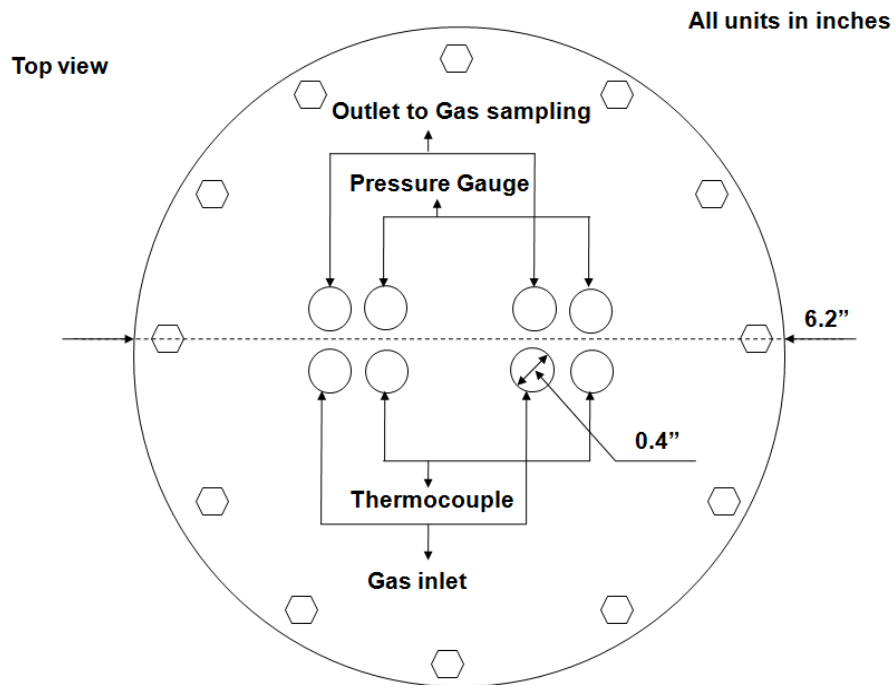


Figure 6.2 Schematic diagram of the chamber head to be developed

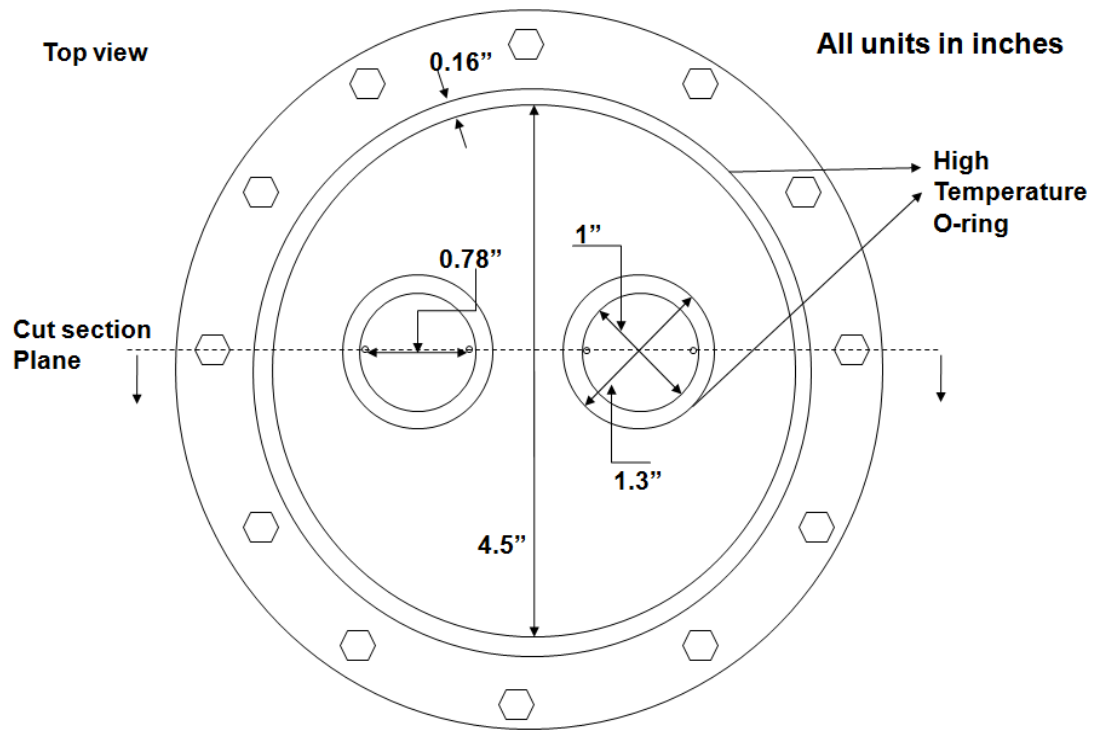


Figure 6.3 Schematic view of the chamber bottom

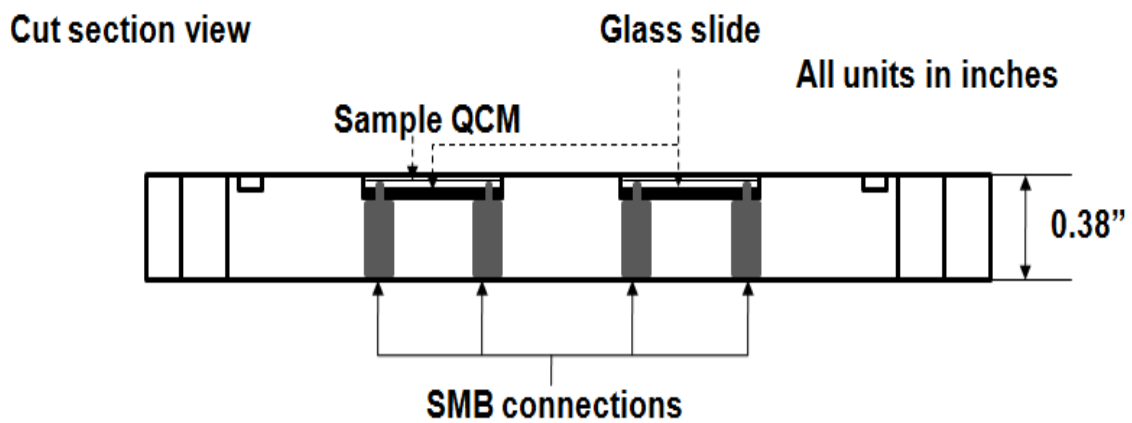


Figure 6.4 Schematic diagram of the cut section view of the chamber bottom

6.2.3 Synchronized Approach with Piezoresistive Microcantilever

Up until now, we had discussed developing and improving a QCM based adsorption setup for gas separation applications. However, with growing emphasis on material cost and sensitivity, newer gas sensing technology needs to be developed in order to broaden the range of analytical techniques. Further, the materials that are used for gas separation application can also function as gas sensing layers. Particularly the MOFs with their ultra high surface area, tunable pore chemistry, chemical and thermal stability can function as gas separation and gas sensing material. Also, some MOFs exhibit a degree of structural flexibility not observed in conventional recognition layers [15, 100-104]. Such structural flexibility can be used in conjunction with surface stress-based transduction mechanisms such as the piezoresistive microcantilever sensors which possess exquisite sensitivity, ultra-low power consumption, and simple instrumentation. Previous demonstration that this property can be used for chemical detection by strain-based transduction mechanisms is provided by Allendorf et al [10].

Given the availability of large number of MOFs and that the piezoresistive microcantilever technology is in its early stages and is not yet suitable for obtaining thermodynamic parameters of adsorption, it would be ideal to use the QCM based adsorption cell to analyze candidate materials and use it to calibrate and test on the microcantilever. Such efforts would not only develop smaller, sensitive and cost effective sorption devices, but also contribute to the field of miniature gas sensor for chemical sensing in hazardous applications.

Research efforts have already been focused on designing and fabricating piezoresistive microcantilever arrays [105]. Based on our initial experiments, the

detection resolution of microcantilever is about few tens of ppm's. However one challenge that remains is the deposition of different MOFs. Unlike QCM, microcantilever requires a film type deposition which is developed only for a few MOFs [17, 106, 107]. However, there is a growing body of work directed to address this challenge.

APPENDIX A

A.1 Snapshot the Experimental Setup

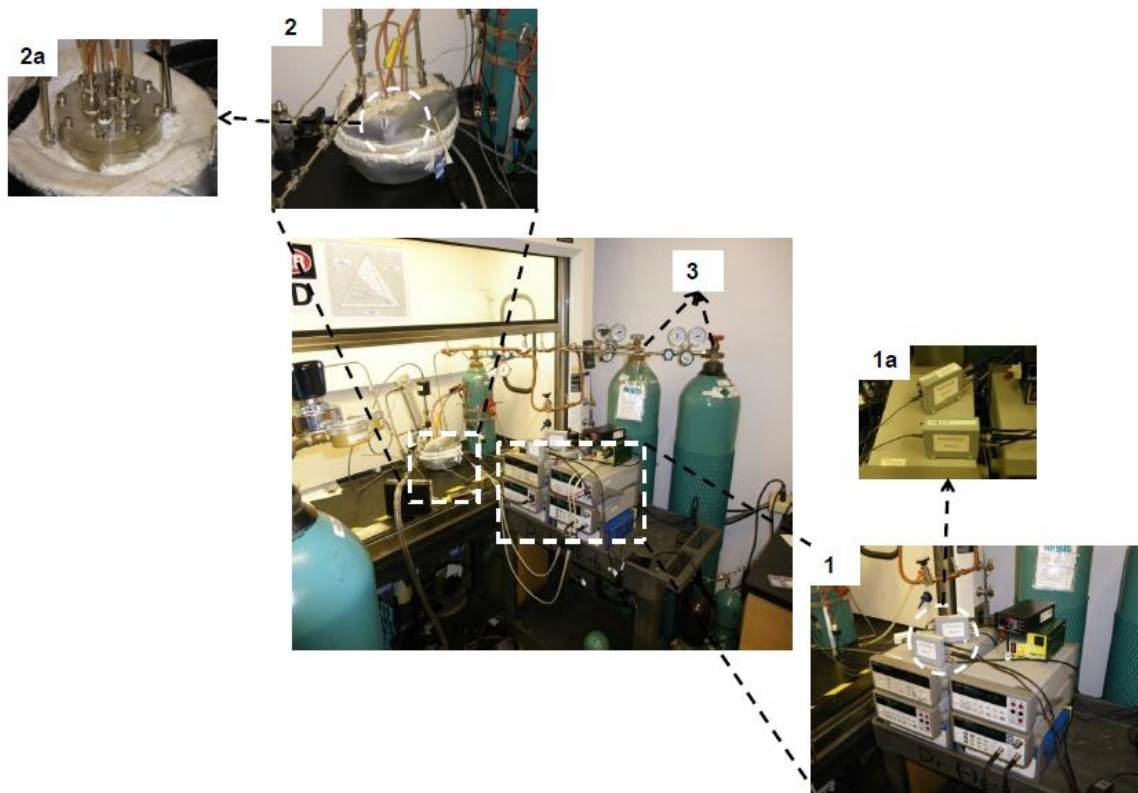


Figure A.1 Labeled photograph of the QCM-based adsorption measurement apparatus. Inset **1** shows the frequency counter, voltmeter, PID temperature controller and pressure reader. Inset **1a** shows the phase lock oscillator used to measure the resonant frequency. Inset **2** and **2a** shows the detailed view of the high temperature, high pressure stainless steel chamber with the heating jacket. **3** represent the gas cylinder used for dosing gas to the chamber.

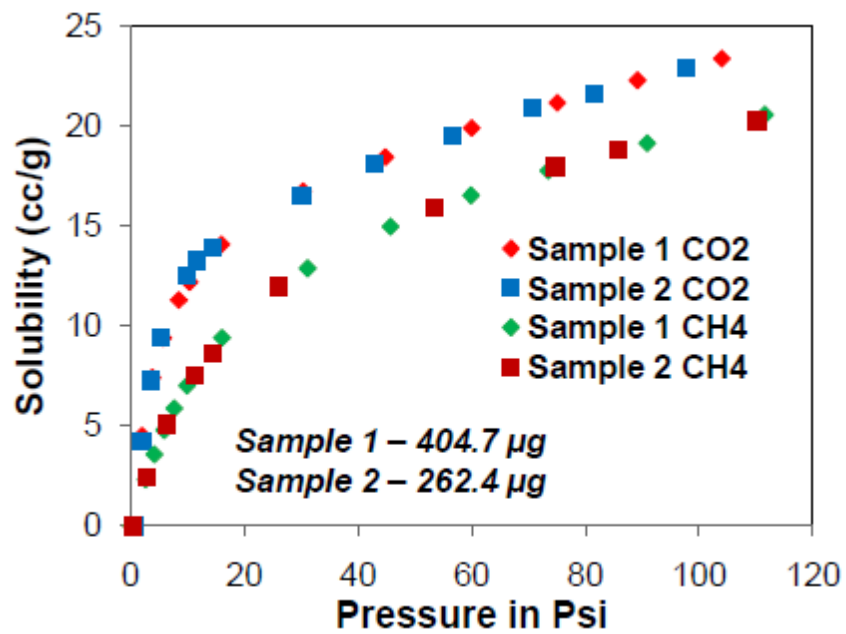


Figure A.2 Comparison of gas adsorption measurements between sample 1 and sample 2 of the small sized Cu-hfipbb MOF crystals at 30°C (Refer section 4.4.1)

APPENDIX B

B.1 Improvement in QCM Cell Design

Figure B.1 shows the gas feed design corresponding to Figure 6.1 for providing a gas to both the reference QCM sensor and the sample QCM sensor. The four-way connector functions to divert the gas from gas source to the reference QCM sensor or the sample QCM sensor. The specifications of the various components in Figures B.1 – B.7 are for reference only, and can be modified.

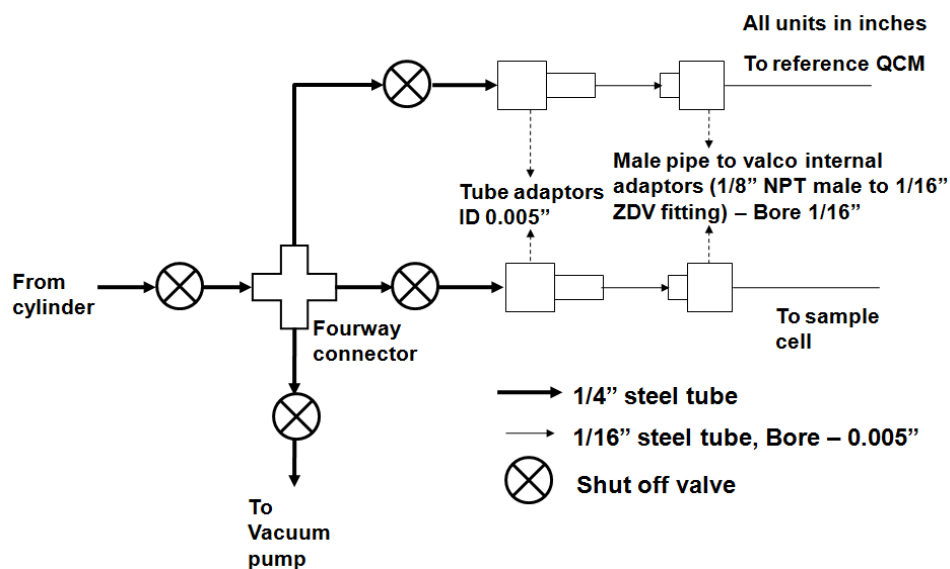


Figure B.1 Schematic diagram of the gas feed system for the multi component QCM based adsorption setup

Figure B.2 shows the thermocouple fitting to the reference QCM sensor and the sample QCM sensor. A K-type Chromega-Alomega 304 SS Sheath 1/16" thermocouple is used in this configuration. However, thermocouples of different types and/or diameters may also be used, depending on the design and other relevant parameters.

All units in inches

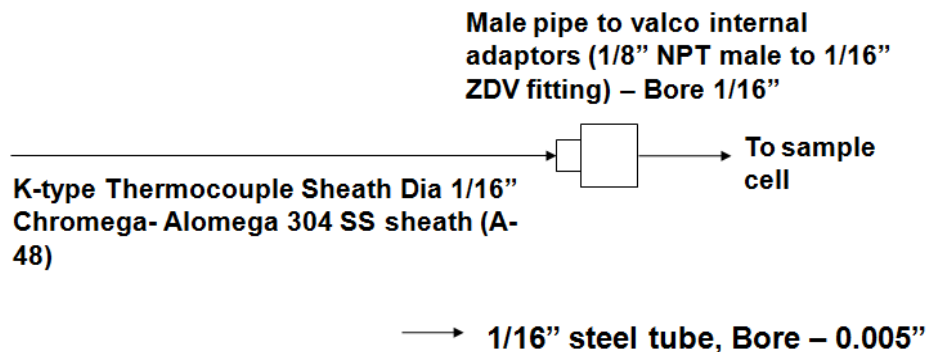


Figure B.2 Schematic diagram of the temperature measurement module

Figure B.3 shows the pressure gauge fitting to the reference QCM sensor and the sample QCM sensor, in order to measure the pressure inside the high pressure cell before and after the isothermal equilibrium is reached. After the adsorption experiments have been completed, the response of the reference QCM is subtracted from the sample deposited QCM to determine the actual adsorption in the porous material, correcting for pressure and temperature effect on the QCM. In this embodiment, a pressure transducer capable of measuring the range between 1 to 250 psi is used to detect the pressure inside the high pressure cell and to convert the reading to an electrical signal. The pressure transducer is optionally connected to a signal conditioner to condition the electrical signal output from the pressure transducer. The optional signal conditioner is in turn connected to a computer to read and record the pressure inside the high pressure cell. It is to be noted that other pressure transducers/sensors capable of measuring a different range of pressure can also be used.

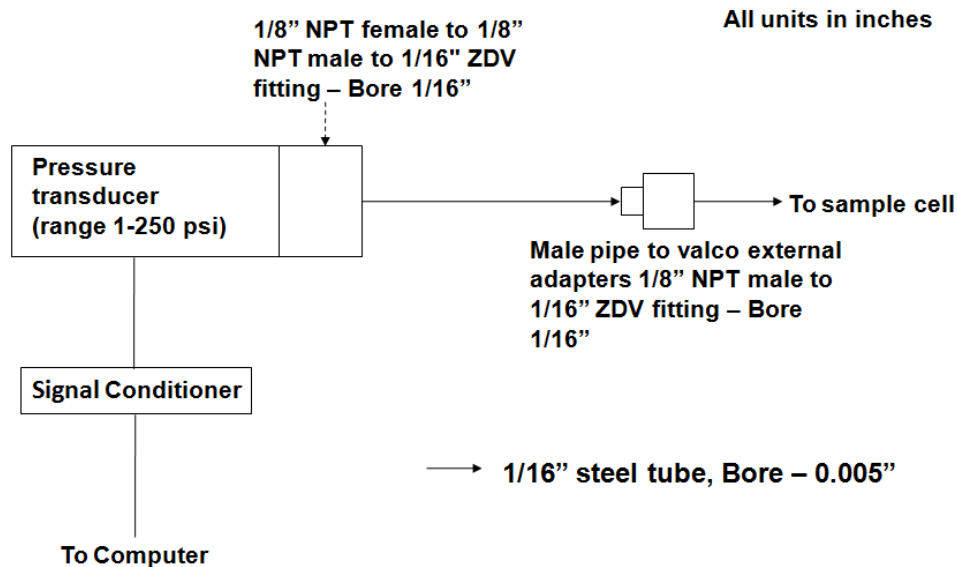


Figure B.3 Schematic view of the pressure measurement module

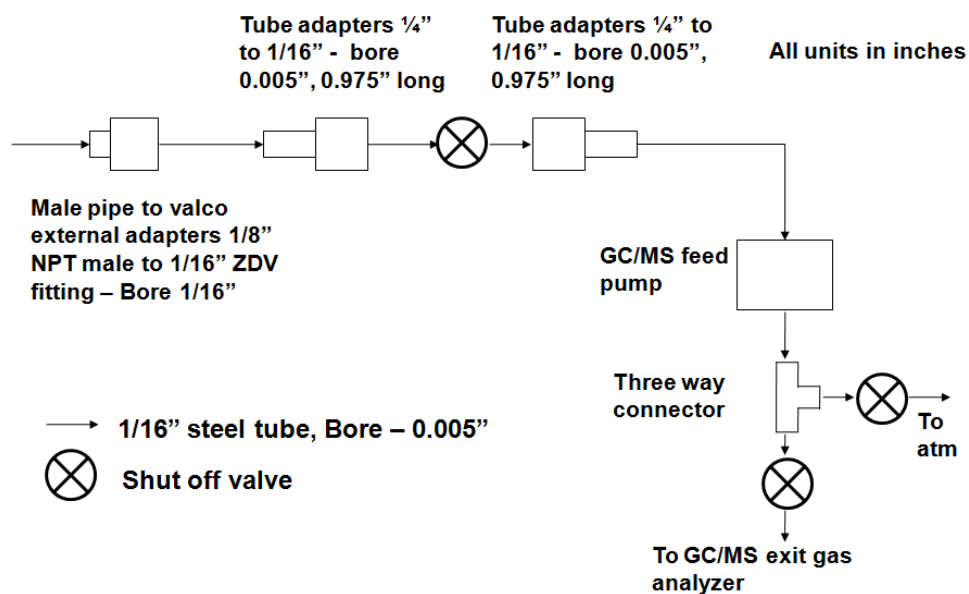


Figure B.4 Schematic representation of the exit gas analyzer module connecting the sample chamber to the GC/MS set up

Figure B.4 shows the configuration of exit gas analyzer connected to the high pressure cell. The gas from the high pressure cell is extracted by a GC/MS feed pump, which in turn connects to a three way connector. Thereafter, the extracted gas is either directed to a GC/MS exit gas analyzer to analyze the content of the gas, or exhausted to the atmosphere.

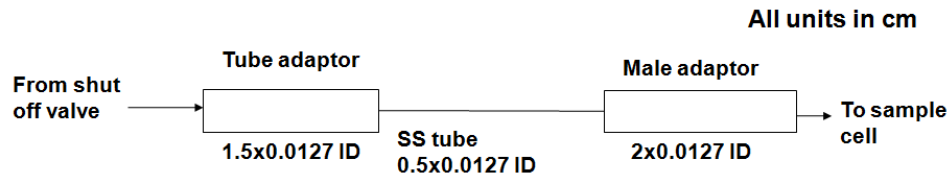


Figure B.5 Detailed schematic view of the gas feed valve fittings to connect the sample chamber to the dosing gas cylinder

Figure B.5 shows the selection of tubes and adaptors between the shut off valve connected to the four-way connector and pressure transducer.

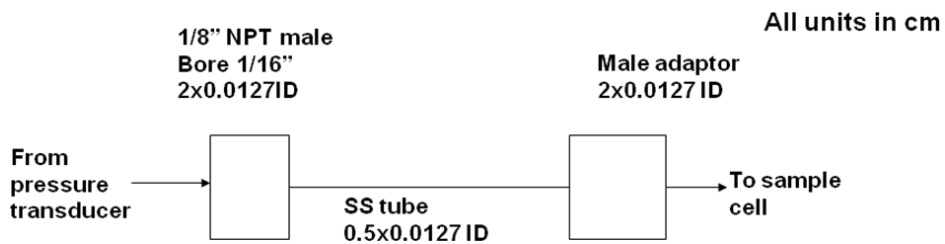


Figure B.6 Detailed schematic view of the pressure gauge fittings between the sample chamber and pressure transducer

Figure B.6 shows the selection of tubes and adaptors between the pressure transducer and the reference/sample QCM sensors in the high pressure cell.

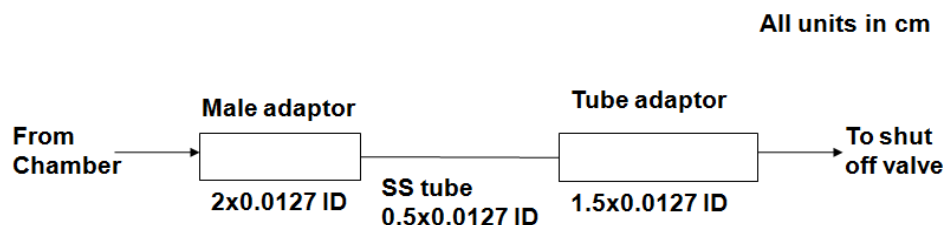


Figure B.7 Detailed schematic view of the exit gas analyzer fitting to connecting the sample chamber to first shut off valve downstream.

Figure B.7 shows the selection of tubes and adaptors between the gas outlet of the high pressure cell and the shut-off valve connected to the GC/MS exit gas analyzer shown in Figure B.4.

The exact configuration and sizes described in Figures 6.1- 6.4 and Figures B.1 – B.7 can be modified according to temperature and pressure needs, and according to sample size and availability of components. However, the device shown illustrates one working embodiment of the invention.

REFERENCES

- [1] R.J. Kuppler, D.J. Timmons, Q.R. Fang, J.R. Li, T.A. Makal, M.D. Young, D.Q. Yuan, D. Zhao, W.J. Zhuang, H.C. Zhou, Potential applications of metal-organic frameworks, *Coord. Chem. Rev.*, 253 (2009) 3042-3066.
- [2] S. Polarz, B. Smarsly, Nanoporous materials, *J. Nanosci. Nanotechnol.*, 2 (2002) 581-612.
- [3] S.T. Meek, J.A. Greathouse, M.D. Allendorf, Metal-Organic Frameworks: A Rapidly Growing Class of Versatile Nanoporous Materials, *Adv. Mater.*, 23 (2011) 249-267.
- [4] J.L.C. Rowsell, O.M. Yaghi, Metal-organic frameworks: a new class of porous materials, *Microporous Mesoporous Mat.*, 73 (2004) 3-14.
- [5] T.H. Bae, J.S. Lee, W.L. Qiu, W.J. Koros, C.W. Jones, S. Nair, A High-Performance Gas-Separation Membrane Containing Submicrometer-Sized Metal-Organic Framework Crystals, *Angew. Chem.-Int. Edit.*, 49 (2010) 9863-9866.
- [6] Y.S. Li, F.Y. Liang, H. Bux, A. Feldhoff, W.S. Yang, J. Caro, Molecular Sieve Membrane: Supported Metal-Organic Framework with High Hydrogen Selectivity, *Angew. Chem.-Int. Edit.*, 49 (2010) 548-551.
- [7] Y.S. Li, F.Y. Liang, H.G. Bux, W.S. Yang, J. Caro, Zeolitic imidazolate framework ZIF-7 based molecular sieve membrane for hydrogen separation, *J. Membr. Sci.*, 354 (2010) 48-54.
- [8] M.C. McCarthy, V. Varela-Guerrero, G.V. Barnett, H.K. Jeong, Synthesis of Zeolitic Imidazolate Framework Films and Membranes with Controlled Microstructures, *Langmuir*, 26 (2010) 14636-14641.

- [9] S. Achmann, G. Hagen, J. Kita, I.M. Malkowsky, C. Kiener, R. Moos, Metal-Organic Frameworks for Sensing Applications in the Gas Phase, *Sensors*, 9 (2009) 1574-1589.
- [10] M.D. Allendorf, R.J.T. Houk, L. Andruszkiewicz, A.A. Talin, J. Pikarsky, A. Choudhury, K.A. Gall, P.J. Hesketh, Stress-induced Chemical Detection Using Flexible Metal-Organic Frameworks, *J. Am. Chem. Soc.*, 130 (2008) 14404-+.
- [11] E. Biemmi, C. Scherb, T. Bein, Oriented growth of the metal organic framework Cu-3(BTC)(2)(H2O)(3)center dot xH(2)O tunable with functionalized self-assembled monolayers, *J. Am. Chem. Soc.*, 129 (2007) 8054-+.
- [12] S. Bordiga, L. Regli, F. Bonino, E. Groppo, C. Lamberti, B. Xiao, P.S. Wheatley, R.E. Morris, A. Zecchina, Adsorption properties of HKUST-1 toward hydrogen and other small molecules monitored by IR, *Phys. Chem. Chem. Phys.*, 9 (2007) 2676-2685.
- [13] K.W. Chapman, G.J. Halder, P.J. Chupas, Guest-dependent high pressure phenomena in a nanoporous metal-organic framework material, *J. Am. Chem. Soc.*, 130 (2008) 10524-+.
- [14] J.-H. Lee, R. Houk, A. Robinson, S. Thornberg, M. Allendorf, P. Hesketh, Nanoporous Metal-Organic Framework Coated Microcantilever Sensors for Water and Methanol Detection, *ECS Meeting Abstracts*, 1001 (2010) 1800.
- [15] K. Uemura, R. Matsuda, S. Kitagawa, Flexible microporous coordination polymers, *J. Solid State Chem.*, 178 (2005) 2420-2429.

- [16] Q.M. Wang, D.M. Shen, M. Bulow, M.L. Lau, S.G. Deng, F.R. Fitch, N.O. Lemcoff, J. Semanscin, Metallo-organic molecular sieve for gas separation and purification, *Microporous Mesoporous Mat.*, 55 (2002) 217-230.
- [17] D. Zacher, O. Shekhah, C. Woll, R.A. Fischer, Thin films of metal-organic frameworks, *Chem. Soc. Rev.*, 38 (2009) 1418-1429.
- [18] E. Haldoupis, S. Nair, D.S. Sholl, Efficient Calculation of Diffusion Limitations in Metal Organic Framework Materials: A Tool for Identifying Materials for Kinetic Separations, *J. Am. Chem. Soc.*, 132 (2010) 7528-7539.
- [19] T. Watanabe, S. Keskin, S. Nair, D.S. Sholl, Computational identification of a metal organic framework for high selectivity membrane-based CO₂/CH₄ separations: Cu(hfipbb)(H₂hfipbb)(0.5), *Phys. Chem. Chem. Phys.*, 11 (2009) 11389-11394.
- [20] R. Ranjan, M. Tsapatsis, Microporous Metal Organic Framework Membrane on Porous Support Using the Seeded Growth Method, *Chem. Mat.*, 21 (2009) 4920-4924.
- [21] W. Morris, C.J. Doonan, H. Furukawa, R. Banerjee, O.M. Yaghi, Crystals as molecules: Postsynthesis covalent functionalization of zeolitic imidazolate frameworks, *J. Am. Chem. Soc.*, 130 (2008) 12626-+.
- [22] L. Bokobza, Multiwall carbon nanotube elastomeric composites: A review, *Polymer*, 48 (2007) 4907-4920.
- [23] W. Choi, J.T. Abrahamson, J.M. Strano, M.S. Strano, Carbon nanotube-guided thermopower waves, *Mater. Today*, 13 (2010) 22-33.
- [24] H.J. Dai, A. Javey, E. Pop, D. Mann, W. Kim, Y.R. Lu, Electrical transport properties and field effect transistors of carbon nanotubes, *Nano*, 1 (2006) 1-13.

- [25] S. Iijima, HELICAL MICROTUBULES OF GRAPHITIC CARBON, *Nature*, 354 (1991) 56-58.
- [26] K.T. Lau, C. Gu, D. Hui, A critical review on nanotube and nanotube/nanoclay related polymer composite materials, *Compos. Pt. B-Eng.*, 37 (2006) 425-436.
- [27] D.-Y. Kang, SINGLE-WALLED METAL OXIDE NANOTUBES AND NANOTUBE MEMBRANES FOR MOLECULAR SEPARATIONS, in: *School of Chemical & Biomolecular Engineering, Georgia Institute of Technology, Atlanta, Georgia, 2012.*
- [28] J.K. Holt, H.G. Park, Y.M. Wang, M. Stadermann, A.B. Artyukhin, C.P. Grigoropoulos, A. Noy, O. Bakajin, Fast mass transport through sub-2-nanometer carbon nanotubes, *Science*, 312 (2006) 1034-1037.
- [29] S. Konduri, H.M. Tong, S. Chempath, S. Nair, Water in single-walled aluminosilicate nanotubes: Diffusion and adsorption properties, *J. Phys. Chem. C*, 112 (2008) 15367-15374.
- [30] D.S. Sholl, J.K. Johnson, Making high-flux membranes with carbon nanotubes, *Science*, 312 (2006) 1003-1004.
- [31] M. Whitby, N. Quirke, Fluid flow in carbon nanotubes and nanopipes, *Nat. Nanotechnol.*, 2 (2007) 87-94.
- [32] J. Zang, S. Konduri, S. Nair, D.S. Sholl, Self-Diffusion of Water and Simple Alcohols in Single-Walled Aluminosilicate Nanotubes, *Acs Nano*, 3 (2009) 1548-1556.
- [33] G. Arora, S.I. Sandler, Air separation by single wall carbon nanotubes: Thermodynamics and adsorptive selectivity, *J. Chem. Phys.*, 123 (2005).

- [34] M.S. Mauter, M. Elimelech, C.O. Osuji, Nanocomposites of Vertically Aligned Single-Walled Carbon Nanotubes by Magnetic Alignment and Polymerization of a Lyotropic Precursor, *Acs Nano*, 4 (2010) 6651-6658.
- [35] S. Pujari, S.S. Rahatekar, J.W. Gilman, K.K. Koziol, A.H. Windle, W.R. Burghardt, Orientation dynamics in multiwalled carbon nanotube dispersions under shear flow, *J. Chem. Phys.*, 130 (2009).
- [36] C.S. Song, T. Kwon, J.H. Han, M. Shandell, M.S. Strano, Controllable Synthesis of Single-Walled Carbon Nanotube Framework Membranes and Capsules, *Nano Lett.*, 9 (2009) 4279-4284.
- [37] M. Moniruzzaman, K.I. Winey, Polymer nanocomposites containing carbon nanotubes, *Macromolecules*, 39 (2006) 5194-5205.
- [38] L. Vaisman, H.D. Wagner, G. Marom, The role of surfactants in dispersion of carbon nanotubes, *Adv. Colloid Interface Sci.*, 128 (2006) 37-46.
- [39] Y.L. Zhao, J.F. Stoddart, Noncovalent Functionalization of Single-Walled Carbon Nanotubes, *Accounts Chem. Res.*, 42 (2009) 1161-1171.
- [40] P. Singh, S. Campidelli, S. Giordani, D. Bonifazi, A. Bianco, M. Prato, Organic functionalisation and characterisation of single-walled carbon nanotubes, *Chem. Soc. Rev.*, 38 (2009) 2214-2230.
- [41] C.N.R. Rao, A. Govindaraj, Synthesis of Inorganic Nanotubes, *Adv. Mater.*, 21 (2009) 4208-4233.
- [42] R. Tenne, G. Seifert, Recent Progress in the Study of Inorganic Nanotubes and Fullerene-Like Structures, in: *Annual Review of Materials Research*, Annual Reviews, Palo Alto, 2009, pp. 387-413.

- [43] V.C. Farmer, A.R. Fraser, J.M. Tait, SYNTHESIS OF IMOGOLITE - TUBULAR ALUMINUM SILICATE POLYMER, *J. Chem. Soc.-Chem. Commun.*, (1977) 462-463.
- [44] S. Mukherjee, V.A. Bartlow, S. Nair, Phenomenology of the growth of single-walled aluminosilicate and aluminogermanate nanotubes of precise dimensions, *Chem. Mat.*, 17 (2005) 4900-4909.
- [45] S. Mukherjee, K. Kim, S. Nair, Short, highly ordered, single-walled mixed-oxide nanotubes assemble from amorphous nanoparticles, *J. Am. Chem. Soc.*, 129 (2007) 6820-6826.
- [46] S.I. Wada, A. Eto, K. Wada, SYNTHETIC ALLOPHANE AND IMOGOLITE, *Journal of Soil Science*, 30 (1979) 347-&.
- [47] G.I. Yucelen, R.P. Choudhury, A. Vyalikh, U. Scheler, H.W. Beckham, S. Nair, Formation of Single-Walled Aluminosilicate Nanotubes from Molecular Precursors and Curved Nanoscale Intermediates, *J. Am. Chem. Soc.*, 133 (2011) 5397-5412.
- [48] B. Bonelli, I. Bottero, N. Ballarini, S. Passeri, F. Cavani, E. Garrone, IR spectroscopic and catalytic characterization of the acidity of imogolite-based systems, *J. Catal.*, 264 (2009) 15-30.
- [49] J. Zang, S. Chempath, S. Konduri, S. Nair, D.S. Sholl, Flexibility of Ordered Surface Hydroxyls Influences the Adsorption of Molecules in Single-Walled Aluminosilicate Nanotubes, *J. Phys. Chem. Lett.*, 1 (2010) 1235-1240.

- [50] T. Borrego, M. Andrade, M.L. Pinto, A.R. Silva, A.P. Carvalho, J. Rocha, C. Freire, J. Pires, Physicochemical characterization of silylated functionalized materials, *J. Colloid Interface Sci.*, 344 (2010) 603-610.
- [51] K. Kupiec, P. Konieczka, J. Namiesnik, Characteristics, Chemical Modification Processes as well as the Application of Silica and its Modified Forms, *Crit. Rev. Anal. Chem.*, 39 (2009) 60-69.
- [52] J.H. Choi, Y.W. Cho, W.S. Ha, W.S. Lyoo, C.J. Lee, B.C. Ji, S.S. Han, W.S. Yoon, Preparation and characterization of syndiotacticity-rich ultra-high molecular weight poly(vinyl alcohol) imogolite blend film, *Polym. Int.*, 47 (1998) 237-242.
- [53] C.A. Scholes, W.X. Tao, G.W. Stevens, S.E. Kentish, Sorption of Methane, Nitrogen, Carbon Dioxide, and Water in Matrimid 5218, *J. Appl. Polym. Sci.*, 117 (2010) 2284-2289.
- [54] D. Punsalan, W.J. Koros, Drifts in penetrant partial molar volumes in glassy polymers due to physical aging, *Polymer*, 46 (2005) 10214-10220.
- [55] D. Punsalan, W.J. Koros, Thickness-dependent sorption and effects of physical aging in a polyimide sample, *J. Appl. Polym. Sci.*, 96 (2005) 1115-1121.
- [56] R.L. Burns, W.J. Koros, Defining the challenges for C₃H₆/C₃H₈ separation using polymeric membranes, *J. Membr. Sci.*, 211 (2003) 299-309.
- [57] T.T. Moore, W.J. Koros, Gas sorption in polymers, molecular sieves, and mixed matrix membranes, *J. Appl. Polym. Sci.*, 104 (2007) 4053-4059.
- [58] T.S. Chung, S.S. Chan, R. Wang, Z.H. Lu, C.B. He, Characterization of permeability and sorption in Matrimid/C-60 mixed matrix membranes, *J. Membr. Sci.*, 211 (2003) 91-99.

- [59] H.Y. Zhao, Y.M. Cao, X.L. Ding, M.Q. Zhou, Q. Yuan, Effects of cross-linkers with different molecular weights in cross-linked Matrimid 5218 and test temperature on gas transport properties, *J. Membr. Sci.*, 323 (2008) 176-184.
- [60] Q.L. Song, S.K. Nataraj, M.V. Roussenova, J.C. Tan, D.J. Hughes, W. Li, P. Bourgoïn, M.A. Alam, A.K. Cheetham, S.A. Al-Muhtaseb, E. Sivaniah, Zeolitic imidazolate framework (ZIF-8) based polymer nanocomposite membranes for gas separation, *Energy Environ. Sci.*, 5 (2012) 8359-8369.
- [61] O. Esekhhile, W.L. Qiu, W.J. Koros, Permeation of Butane Isomers through 6FDA-DAM Dense Films, *J. Polym. Sci. Pt. B-Polym. Phys.*, 49 (2011) 1605-1620.
- [62] J.Q. Liu, T.H. Bae, W.L. Qiu, S. Husain, S. Nair, C.W. Jones, R.R. Chance, W.J. Koros, Butane isomer transport properties of 6FDA-DAM and MFI-6FDA-DAM mixed matrix membranes, *J. Membr. Sci.*, 343 (2009) 157-163.
- [63] L.L. Cui, W.L. Qiu, D.R. Paul, W.J. Koros, Physical aging of 6FDA-based polyimide membranes monitored by gas permeability, *Polymer*, 52 (2011) 3374-3380.
- [64] L.L. Cui, W.L. Qiu, D.R. Paul, W.J. Koros, Responses of 6FDA-based polyimide thin membranes to CO₂ exposure and physical aging as monitored by gas permeability, *Polymer*, 52 (2011) 5528-5537.
- [65] P.I. Reyes, Z. Zhang, H.H. Chen, Z.Q. Duan, J. Zhong, G. Saraf, Y.C. Lu, O. Taratula, E. Galoppini, N.N. Boustany, A ZnO Nanostructure-Based Quartz Crystal Microbalance Device for Biochemical Sensing, *IEEE Sens. J.*, 9 (2009) 1302-1307.

- [66] J.B. Zheng, G. Li, X.F. Ma, Y.M. Wang, G. Wu, Y.N. Cheng, Polyaniline-TiO₂ nano-composite-based trimethylamine QCM sensor and its thermal behavior studies, *Sens. Actuator B-Chem.*, 133 (2008) 374-380.
- [67] C.Y. Huang, M. Song, Z.Y. Gu, H.F. Wang, X.P. Yan, Probing the Adsorption Characteristic of Metal-Organic Framework MIL-101 for Volatile Organic Compounds by Quartz Crystal Microbalance, *Environ. Sci. Technol.*, 45 (2011) 4490-4496.
- [68] O. Zybaylo, O. Shekhah, H. Wang, M. Tafipolsky, R. Schmid, D. Johannsmann, C. Woll, A novel method to measure diffusion coefficients in porous metal-organic frameworks, *Phys. Chem. Chem. Phys.*, 12 (2010) 8092-8097.
- [69] J.H. Kim, W.J. Koros, D.R. Paul, Physical aging of thin 6FDA-based polyimide membranes containing carboxyl acid groups. Part I. Transport properties, *Polymer*, 47 (2006) 3094-3103.
- [70] K.H. Park, M.S. Koh, C.H. Yoon, H.W. Kim, H.D. Kim, The behavior of quartz crystal microbalance in high pressure CO₂, *J. Supercrit. Fluids*, 29 (2004) 203-212.
- [71] A. Venkatasubramanian, M. Navaei, K.R. Bagnall, K.C. McCarley, S. Nair, P.J. Hesketh, Gas Adsorption Characteristics of Metal-Organic Frameworks via Quartz Crystal Microbalance Techniques, *J. Phys. Chem. C*, 116 (2012) 15313-15321.
- [72] O.a.S. Manual, PLO-10 Series Phase Lock Oscillator, in: Inficon (Ed.), NY, 2000.
- [73] A. Arnau, *Piezoelectric Transducers And Application*, Springer, 2004.

- [74] C.S. Lu, O. Lewis, INVESTIGATION OF FILM-THICKNESS DETERMINATION BY OSCILLATING QUARTZ RESONATORS WITH LARGE MASS LOAD, J. Appl. Phys., 43 (1972) 4385-&.
- [75] C. Steinem, Janshoff, Andreas. , Piezoelectric Sensors, 2007.
- [76] K. Keiji Kanazawa, J.G. Gordon, The oscillation frequency of a quartz resonator in contact with liquid, Analytica Chimica Acta, 175 (1985) 99-105.
- [77] K.K. Kanazawa, J.G. Gordon, THE OSCILLATION FREQUENCY OF A QUARTZ RESONATOR IN CONTACT WITH A LIQUID, Analytica Chimica Acta, 175 (1985) 99-105.
- [78] T. Kohler, D. Woermann, CHANGES OF THE OSCILLATION FREQUENCY OF A QUARTZ RESONATOR IN CONTACT WITH A BINARY-LIQUID MIXTURE OF CRITICAL COMPOSITION AS FUNCTION OF TEMPERATURE, REVISITED, Berichte Der Bunsen-Gesellschaft-Physical Chemistry Chemical Physics, 98 (1994) 983-985.
- [79] M. Yang, M. Thompson, Surface morphology and the response of the thickness-shear mode acoustic wave sensor in liquids, Langmuir, 9 (1993) 1990-1994.
- [80] D. Johannsmann, I. Reviakine, E. Rojas, M. Gallego, Effect of Sample Heterogeneity on the Interpretation of QCM(-D) Data: Comparison of Combined Quartz Crystal Microbalance/Atomic Force Microscopy Measurements with Finite Element Method Modeling, Anal. Chem., 80 (2008) 8891-8899.
- [81] J.D. Wind, Improving Polyimide Membrane Resistance to Carbon Dioxide Plasticization in Natural Gas Separations, in, University of Texas, Austin, Austin, TX, 2002.

- [82] J.H. Kim, W.J. Koros, D.R. Paul, Effects of CO₂ exposure and physical aging on the gas permeability of thin 6FDA-based polyimide membranes - Part 1. Without crosslinking, *J. Membr. Sci.*, 282 (2006) 21-31.
- [83] C.K. Yeom, J.M. Lee, Y.T. Hong, K.Y. Choi, S.C. Kim, Analysis of permeation transients of pure gases through dense polymeric membranes measured by a new permeation apparatus, *J. Membr. Sci.*, 166 (2000) 71-83.
- [84] B.E. Poling, *The properties of gases and liquids*, 5th ed. ed., New York, McGraw-Hill, 2001.
- [85] Z.B. Bao, S. Alnemrat, L.A. Yu, I. Vasiliev, Q.L. Ren, X.Y. Lu, S.G. Deng, Kinetic separation of carbon dioxide and methane on a copper metal-organic framework, *J. Colloid Interface Sci.*, 357 (2011) 504-509.
- [86] A.I. Skoulidas, D.S. Sholl, Molecular dynamics Simulations of self-diffusivities, corrected diffusivities, and transport diffusivities of light gases in four silica zeolites to assess influences of pore shape and connectivity, *J. Phys. Chem. A*, 107 (2003) 10132-10141.
- [87] R.I. Masel, *Principles of adsorption and reaction on solid surfaces*, New York, Wiley, 1996.
- [88] T. Tomita, K. Nakayama, H. Sakai, Gas separation characteristics of DDR type zeolite membrane, *Microporous Mesoporous Mat.*, 68 (2004) 71-75.
- [89] A.S. Huang, J. Caro, Covalent Post-Functionalization of Zeolitic Imidazolate Framework ZIF-90 Membrane for Enhanced Hydrogen Selectivity, *Angew. Chem.-Int. Edit.*, 50 (2011) 4979-4982.

- [90] A.S. Huang, W. Dou, J. Caro, Steam-Stable Zeolitic Imidazolate Framework ZIF-90 Membrane with Hydrogen Selectivity through Covalent Functionalization, *J. Am. Chem. Soc.*, 132 (2010) 15562-15564.
- [91] A.S. Huang, N.Y. Wang, C.L. Kong, J. Caro, Organosilica-Functionalized Zeolitic Imidazolate Framework ZIF-90 Membrane with High Gas-Separation Performance, *Angew. Chem.-Int. Edit.*, 51 (2012) 10551-10555.
- [92] I. Bottero, B. Bonelli, S.E. Ashbrook, P.A. Wright, W. Zhou, M. Tagliabue, M. Armandi, E. Garrone, Synthesis and characterization of hybrid organic/inorganic nanotubes of the imogolite type and their behaviour towards methane adsorption, *Physical Chemistry Chemical Physics*, 13 (2011) 744-750.
- [93] D.-Y. Kang, Brunelli, N A., Yucelen, G. I., Venkatasubramanian, A., Zang, J., Leisen, J., Hesketh, P.J., Jones, C. W., and Nair, S., Direct Synthesis of Single-Walled Aminoaluminosilicate Nanotubes: One-Dimensional Nanomaterials with Enhanced Molecular Adsorptive Selectivity, Submitted, (2013).
- [94] H. Zheng, L. Han, H. Ma, Y. Zheng, H. Zhang, D. Liu, S. Liang, Adsorption characteristics of ammonium ion by zeolite 13X, *J. Hazard. Mater.*, 158 (2008) 577-584.
- [95] N.A. Brunelli, S.A. Didas, K. Venkatasubbaiah, C.W. Jones, Tuning Cooperativity by Controlling the Linker Length of Silica-Supported Amines in Catalysis and CO₂ Capture, *J. Am. Chem. Soc.*, 134 (2012) 13950-13953.
- [96] S. Choi, J.H. Drese, C.W. Jones, Adsorbent Materials for Carbon Dioxide Capture from Large Anthropogenic Point Sources, *ChemSusChem*, 2 (2009) 796-854.

- [97] P. Bollini, S.A. Didas, C.W. Jones, Amine-oxide hybrid materials for acid gas separations, *J. Mater. Chem.*, 21 (2011) 15100-15120.
- [98] P. Neogi, Transport Phenomena in Polymer Membranes, in: P. Neogi (Ed.) *Diffusion in Polymers*, Marcel Dekker Inc, New York, 1996, pp. 173-178.
- [99] *Molecular sieves : science and technology*, Berlin :, Springer-Verlag, 1998.
- [100] D.S. Coombes, F. Cora, C. Mellot-Draznieks, R.G. Bell, Sorption-Induced Breathing in the Flexible Metal Organic Framework CrMIL-53: Force-Field Simulations and Electronic Structure Analysis, *Journal of Physical Chemistry C*, 113 (2009) 544-552.
- [101] T. Devic, P. Horcajada, C. Serre, F. Salles, G. Maurin, B. Moulin, D. Heurtaux, G. Clet, A. Vimont, J.M. Greneche, B. Le Ouay, F. Moreau, E. Magnier, Y. Filinchuk, J. Marrot, J.C. Lavalley, M. Daturi, G. Ferey, Functionalization in Flexible Porous Solids: Effects on the Pore Opening and the Host-Guest Interactions, *J. Am. Chem. Soc.*, 132 (2010) 1127-1136.
- [102] A.J. Fletcher, K.M. Thomas, M.J. Rosseinsky, Flexibility in metal-organic framework materials: Impact on sorption properties, *J. Solid State Chem.*, 178 (2005) 2491-2510.
- [103] J.R. Li, R.J. Kuppler, H.C. Zhou, Selective gas adsorption and separation in metal-organic frameworks, *Chem. Soc. Rev.*, 38 (2009) 1477-1504.
- [104] P.K. Thallapally, J. Tian, M.R. Kishan, C.A. Fernandez, S.J. Dalgarno, P.B. McGrail, J.E. Warren, J.L. Atwood, Flexible (Breathing) Interpenetrated Metal-Organic Frameworks for CO₂ Separation Applications, *J. Am. Chem. Soc.*, 130 (2008) 16842-16843.

- [105] A. Venkatasubramanian, J.H. Lee, V. Stavila, A. Robinson, M.D. Allendorf, P.J. Hesketh, MOF @ MEMS: Design optimization for high sensitivity chemical detection, *Sens. Actuator B-Chem.*, 168 (2012) 256-262.
- [106] K. Otsubo, T. Haraguchi, O. Sakata, A. Fujiwara, H. Kitagawa, Step-by-Step Fabrication of a Highly Oriented Crystalline Three-Dimensional Pillared-Layer-Type Metal-Organic Framework Thin Film Confirmed by Synchrotron X-ray Diffraction, *J. Am. Chem. Soc.*, 134 (2012) 9605-9608.
- [107] V. Stavila, J. Volponi, A.M. Katzenmeyer, M.C. Dixon, M.D. Allendorf, Kinetics and mechanism of metal-organic framework thin film growth: systematic investigation of HKUST-1 deposition on QCM electrodes, *Chemical Science*, 3 (2012) 1531-1540.